ELECTROMAGNETIC ANALYSIS OF A FINITE REINFORCED CONCRETE SLAB

Armin Parsa

A thesis
in
The Department
of
Electrical and Computer Engineering

Presented in Partial Fulfillment of the Requirements
For the Degree of Doctor of Philosophy
Concordia University
Montréal, Québec, Canada

April 2008

Library and
Archives Canada

Published Heritage
Branch

395 Wellington Street
Ottawa ON K1A 0N4
Canada

Bibliothèque et
Archives Canada

Direction du
Patrimoine de l'édition

395, rue Wellington
Ottawa ON K1A 0N4
Canada

Your file Votre référence
ISBN: 978-0-494-37758-1
Our file Notre référence
ISBN: 978-0-494-37758-1

NOTICE:
The author has granted a non-exclusive license allowing Library and Archives Canada to reproduce, publish, archive, preserve, conserve, communicate to the public by telecommunication or on the Internet, loan, distribute and sell theses worldwide, for commercial or non-commercial purposes, in microform, paper, electronic and/or any other formats.

The author retains copyright ownership and moral rights in this thesis. Neither the thesis nor substantial extracts from it may be printed or otherwise reproduced without the author's permission.

AVIS:
L'auteur a accordé une licence non exclusive permettant à la Bibliothèque et Archives Canada de reproduire, publier, archiver, sauvegarder, conserver, transmettre au public par télécommunication ou par l'Internet, prêter, distribuer et vendre des thèses partout dans le monde, à des fins commerciales ou autres, sur support microforme, papier, électronique et/ou autres formats.

L'auteur conserve la propriété du droit d'auteur et des droits moraux qui protège cette thèse. Ni la thèse ni des extraits substantiels de celle-ci ne doivent être imprimés ou autrement reproduits sans son autorisation.

In compliance with the Canadian Privacy Act some supporting forms may have been removed from this thesis.

While these forms may be included in the document page count, their removal does not represent any loss of content from the thesis.

Conformément à la loi canadienne sur la protection de la vie privée, quelques formulaires secondaires ont été enlevés de cette thèse.

Bien que ces formulaires aient inclus dans la pagination, il n'y aura aucun contenu manquant.

Canada

CONCORDIA UNIVERSITY

School of Graduate Studies

This is to certify that the thesis prepared

By: **Mr. Armin Parsa**

Entitled: **Electromagnetic Analysis of a Finite Reinforced Concrete Slab**

and submitted in partial fulfillment of the requirements for the degree of

Doctor of Philosophy (Electrical Engineering)

complies with the regulations of this University and meets the accepted standards with respect to originality and quality.

Signed by the final examining commitee:

____ Chair
____ External Examiner
____ Examiner
____ Examiner
____ Examiner
____ Supervisor

Approved ____
Chair of Department or Graduate Program Director

__________ 20 ____ ________________________________

Dr. Nabil Esmail, Dean
Faculty of Engineering and Computer Science

Abstract

Electromagnetic Analysis of a Finite Reinforced Concrete Slab

Armin Parsa
Concordia University, 2008

In order to calculate the electromagnetic fields reflected, transmitted, and diffracted by a finite reinforced concrete slab in the presence of a source, a Green's function/method of moments approach has been developed. In doing so, a Green's function solution for a finite and electrically thick dielectric slab is obtained. The Green's function for the arbitrary position of the source and field point is based on the interior Green's function, i.e. the Green's function when the source and the field point are both inside the slab. The solution is two-dimensional, with an electric line source excitation.

The first development in this thesis presents an interior electric field Green's function for a thick and finite dielectric slab. The presented solution is based on the separation of variables method which gives an exact solution to a separable slab. The separable slab is closely related to the finite slab. The separable slab solution is expressed in terms of the contribution of the surface wave modes plus the remaining part which is called the "residual wave" contribution. In order to model a finite slab, the surface wave contribution of the separable slab is modified since the separable slab solution fails to model the finite slab when a surface wave mode is close to resonance. The modification is done by correcting the end cap reflection coefficient for each mode and accounting for the mode conversions. The mode conversions and reflections are characterized by the end cap scattering matrix which is obtained by the method of moments. As a result, the interior Green's function solution for a finite slab is the modified surface wave solution plus the residual wave contribution obtained for the separable slab. The Green's functions for the cases when the source and/or field points are outside the slab are obtained using the interior Green's function and the surface equivalence principle.

Having the finite slab Green's function, it is possible to model a finite reinforced concrete slab. Since the metallic rods are assumed to be electrically thick, each metallic rod is replaced by a circular array of thin wires complying with the "same surface area" rule of thumb. To obtain the unknown induced currents on the surface of the thin wires, the method of moments is used in conjunction with the finite slab Green's function. The model is used to investigate the reflection and transmission of electromagnetic waves for some cases of practical interest.

Acknowledgments

Firstly, I would like to thank my supervisor Prof. Robert Paknys for his guidance, advice, and support throughout the completion of this thesis. This work would not have been possible without his invaluable technical suggestions, his encouragements and his continuous financial support. He has been my most important professional role model.

I would also like to express my sincere gratitude to Professor Christopher W. Trueman for his suggestions and advice. I also wish to thank Professors Derek A. McNamara, William E. Lynch and Muthukumaran Packirisamy for their participation in my examination committee and for their invaluable suggestions. My gratitude also goes to Professor Abdel R. Sebak for providing warm and friendly discussions.

I wish to express my heartfelt thanks to my parents, Mandana and Taghi, and my brother Maziyar for their inspiration and support during this thesis.

I would also like to thank my friends Pouneh Shabani and Arian Mirhashemi for inspiring me to focus on my thesis, my friend and my old roommate Alper K. Ozturk for having many interesting conversations on different electromagnetic problems, my fellow graduate student and friend, Aidin Mehdipour for having many interesting discussions on antenna design problems, and my other fellow graduate student, Sadegh Farzaneh, and our laboratory assistant David Gaudine for fixing computer problems.

Contents

List of Figures ix

List of Tables xviii

List of Abbreviations xix

1 Introduction 1

1.1 Problem Statement 2

1.2 Approach 4

1.3 Basic Assumptions 6

1.4 Document Overview 7

2 Background and Literature Review 9

2.1 Finite Dielectric Slab 9

2.2 Reinforced Concrete 15

3 An Exact Interior Green's Function Solution for a Separable and Finite Dielectric Slab 19

3.1 Separation of Variables 20

3.2 Electric Line Source Inside an Infinite Extent Dielectric Slab Backed by a PMC or PEC 24

3.3 Electric Line Source Inside a Separable Structure 32

3.4 Resonance Inside a Separable Dielectric Slab 45
3.5 Results and Discussion 47

4 Interior Green's Function Solution for a Thick and Finite Dielectric Slab 54
4.1 End Cap Scattering Matrix 55
4.2 MoM Formulation 56
4.3 SW Solution for a Semi-Infinite Dielectric Slab 61
4.4 Finite Dielectric Slab Solution Using the GSM Method 64
4.5 Results and Discussion 67

5 Exterior Analysis of a Finite Thick Dielectric Slab 76
5.1 Case 1: Source Inside, Field Point Outside 77
  5.1.1 Electric Line Source 77
5.2 Case 2: Source Outside, Field Point Inside 82
5.3 Case 3: Source Outside, Field Point Outside 84
5.4 Numerical Integration 89
5.5 Results and Discussion 99

6 Analysis of a Finite Reinforced Concrete Slab 109
6.1 Finite Reinforced Concrete Slab 110
  6.1.1 MoM/GF 111
  6.1.2 SIE/MoM 113
6.2 Results and Discussion 120

7 Conclusions 133
7.1 Future Work 135

Bibliography 137

A **144**

A.1 Dielectric Slab Bisected by PMC and PEC Ground Planes 144

A.2 1D Green's Function for Dielectric Slab Backed by PMC Plane 145

A.3 1D Green's Function for Dielectric Slab Backed by PEC Plane 149

A.4 Surface Wave Modes of the 2D Infinite Extent Dielectric Slab 151

A.5 E_z Due to M_x and M_y 153

A.6 H_x and H_y Due to M_x and M_y 155

A.7 Self Term Evaluation for the First and Second Derivative of Free Space Green's Function 156

A.8 Self Impedance Term Evaluation for the Interior Green's Function . . 159

List of Figures

1.1 A reinforced concrete slab. 2

1.2 (a) A two-dimensional infinite dielectric slab embedding metallic bars. (b) A two-dimensional finite dielectric slab embedding metallic bars. 3

3.3 An infinite extent dielectric slab. 25

3.4 (a) Geometry of an infinite dielectric slab of thickness d grounded by a (a) PMC plane at $x = d$ (b) PEC plane at $x = d$. 25

3.5 (a) Singularities of G_x on the complex λ_x plane, top Riemann sheet. The singularities include poles ($\times$) and a branch point ($\bullet$). (b) Branch point ($\circ$) singularity of G_y on the complex λ_y plane. 28

3.6 (a) Singularities on the top sheet of G_x mapped on the complex λ_y plane. G_x has poles ($\times$) and branch point ($\bullet$) singularity. G_y has a branch point ($\circ$) at $\lambda_y = 0$. (b) The complex η plane obtained by $\eta = \sqrt{\lambda_y}$ transformation. 29

3.7 Complex w-plane shows the proper (P_{1-4}) and improper (I_{1-4}) regions which correspond to the top and bottom sheet on the η plane. The LW poles ($\otimes$) and SW poles ($\times$) are shown on this plane. 30

3.8 Complex w-plane shows the path of integration C_2 and C_3. Integration along P_2 and P_3 is equivalent to integration along C_y shown in Fig. 3.7. The LW poles ($\otimes$) and SW poles ($\times$) are shown on this plane. 32

3.9 Geometry of a finite dielectric slab of thickness $2d$ and height $2L$ surrounded by Regions ① and ③. If $\epsilon_3 = 2\epsilon_1 - \epsilon_2$, the structure becomes a separable slab. 33

3.10 (a) Singularities of G_x in the complex λ_x plane, top Riemann sheet. The singularities include poles ($\times$) and a branch point ($\bullet$). (b) Poles ($*$) and branch point ($\circ$) of G_y in the complex λ_y plane, top Riemann sheet. 37

3.11 Poles ($*$) and branch point ($\circ$) of G_y accompanied by the poles ($\times$) and branch point ($\bullet$) of G_x on the complex λ_y plane. The path C_y shows the contour of integration. 38

3.12 Complex η_2 plane showing the poles ($*$) and branch points ($\circ$) of G_y accompanied by the poles ($\times$) and branch points ($\bullet$) of G_x. 38

3.13 The path of integration on the complex w-plane. The singularities of G_y which are poles ($*$) and branch points ($\circ$) are shown, accompanied by the SW poles ($\times$) and the LW poles ($\otimes$) of G_x. 39

3.14 The paths having the mode contributions defined by (a) G_{r++} (b) G_{r--} (c) G_{r+-} (d) G_{r-+}. 42

3.15 The signal flow graph for (a) G_{r++} (b) G_{r--} (c) G_{r+-} (d) G_{r-+}. . . . 43

3.16 The signal flow graph showing the multiple SW reflections inside a separable structure. 44

3.17 A surface wave originating from section A travels back to its origin after reflecting from the top and bottom end cap, respectively. 46

3.18 A line source at $(x_s, y_s) = (0.1, 0)$ m inside a $2L \times 2d = 0.5 \times 0.2$ m separable slab. (a) The electric field at $(x, y) = (0.04, y)$ m. (b) The locations of G_x (+) and G_y (o) poles on the w plane. 48

3.19 A line source at $(x_s, y_s) = (0.02, -0.22)$ m inside a $2L \times 2d = 0.5 \times 0.2$ m separable slab. (a) The electric field at $(x, y) = (0.01, y)$ m. (b) The locations of PMC (+) and PEC (×) poles of G_x and PMC (o) and PEC (□) poles of G_y on the w plane. 49

3.20 The electric field along the width of the slab. The source is at $(x_s, y_s) = (0.02, -0.22)$ m, and the field point is along $y = -0.23$ m. 50

3.21 A line source at $(x_s, y_s) = (0.1, 0)$ m inside a $2L \times 2d = 0.535 \times 0.2$ m separable slab. (a) The electric field at $(x, y) = (0.04, y)$ m. (b) The locations of G_x (+) and G_y (o) poles on the w plane. 51

3.22 (a) The average of the total SW field for PMC modes calculated along the line $(x, y) = (0.04, -L < y < L)$ m inside a SS. (b) The average of the PMC mode fields calculated along the line $(x, y) = (0.04, -L < y < L)$ m inside a SS. 52

4.1 Semi-infinite dielectric slab of thickness $2d$. The infinite plane S at $y = L$ separates the structure into Regions ① and ②. 55

4.2 An infinite extent dielectric slab. 59

4.3 Separable semi-infinite dielectric slab of thickness $2d$. The separability condition requires $\epsilon_3 = 2\epsilon_1 - \epsilon_2$. 62

4.4 A finite dielectric slab of length $2L$ and thickness $2d$. 65

4.5 The signal flow graph picturing the multiple mode conversions and reflections inside a finite dielectric slab. 66

4.6 The electric field along the top end of a semi-infinite dielectric slab at $(x, y) = (x, 0.4)$ m. The slab thickness is $2d = 0.2$ m. The end cap is at $y = L = 0.4$ m, and the source is at $(x_s, y_s) = (0.1, -0.2)$ m. 68

4.7 The electric field inside a semi-infinite dielectric slab. This validates the MoM solution which is used to find the scattering matrix of the end cap. The slab has a thickness of $2d = 0.2$ m. The source is at $(x_s, y_s) = (0.1, -0.2)$ m, and the field point is at $(x, y) = (0.1, y)$ m. The end cap is at $y = L = 0.4$ m. 69

4.8 The comparison of the electric field inside a SIS and S-SIS. The source is at $(x_s, y_s) = (0.05, -0.2)$ m, and the field point is at $(x, y) = (0.05, y)$ m. The slab thickness is (a) $2d = 0.1$ m and (b) $2d = 0.2$ m. 70

4.9 (a) The comparison of the (a) amplitude and (b) the phase of the first three elements of the reflection coefficient matrix $\mathbf{\Gamma}^m$ and the equivalent scattering matrix $\mathbf{\Lambda}^m$. 71

4.10 (a) The electric field inside a $2L \times 2d = 0.5 \times 0.2$ m finite dielectric slab. (a) The line source is at $(x_s, y_s) = (0.1, 0)$ m, and the field point is at $(x, y) = (0.04, y)$ m. (b) The line source is at $(x_s, y_s) = (0.02, -0.22)$ m, and the field point is at $(x, y) = (0.01, y)$ m. 72

4.11 The electric field inside a FS. The slab has a thickness of $2d = 0.2$ m and a height of $2L = 0.535$ m. The source is at $(x_s, y_s) = (0.1, 0)$ m, and the field point is at $(x, y) = (0.04, y)$ m. 74

4.12 The electric field inside a FS. The slab has a thickness of $2d = 0.2$ m and a height of $2L = 0.535$ m. The source is at $(x_s, y_s) = (0.01, 0.26)$ m, and the field point is at $(x, y) = (0.02, y)$ m. 74

4.13 (a) The electric field inside a FS. The source is at $(x_s, y_s) = (0.1, -0.23)$ m, and the field point is at $(x, y) = (x, -0.24)$ m. (a) If the residual wave is omitted, only the SW-FS remains which doesn't match the SIE/MoM-FS. (b) The residual wave is comparable to the SW-FS. . . 75

5.1 (a) An electric line source inside a finite dielectric slab. (b) Applying the surface equivalent theorem to obtain the exterior field, the dielectric slab is replaced by the equivalent surface currents J_{eq} and M_{eq}. 77

5.2 A finite dielectric slab. 82

5.3 (a) An electric line source outside a finite dielectric slab. (b) Surface equivalence principle applied to the interior region. 85

5.4 The dielectric slab surface divided into $4p + 4\ell$ cells. 90

5.5 The magnitude and phase of the equivalent electric current on the surface of the slab when the line source is in the interior region. Source is at $(x_s, y_s) = (0.1, 0)$ m. The slab has a thickness of $2d = 0.2$ m and height of $2L = 0.5$ m. 100

5.6 The magnitude and phase of the equivalent magnetic current on the surface of the slab when the line source is in the interior region. Source is at $(x_s, y_s) = (0.1, 0)$ m. The slab has a thickness of $2d = 0.2$ m and height of $2L = 0.5$ m. 101

5.7 The comparison of the exterior electric field generated by a line source inside the finite and infinite slab. Source is at $(x_s, y_s) = (0.1, 0.)$ m, and the field point is at $(x_o, y_o) = (-1, y)$ m. 102

5.8 The exterior electric field generated by a line source inside the finite and infinite slab. Source is at $(x_s, y_s) = (0.01, 0.24)$ m, and the field point is at $(x_o, y_o) = (-3, y)$ m. 102

5.9 The effect of increasing the slab height in the exterior field. Finite slab solution is compared with the infinite case. Source is at $(x_s, y_s) = (0.01, 0.24)$ m, and the field point is at $(x_o, y_o) = (-3, y)$ m. (a) $\sigma = 0.195$ mS/m (b) $\sigma = 1.95$ mS/m 103

5.10 Surface equivalent currents generated by a line source on the surface of a finite dielectric slab with thickness of $2d = 0.2$ m and height of $2L = 0.5$ m. The line source is at $(x_s, y_s) = (0, -0.2226)$ m. 104

5.11 The exterior electric field generated by a line source on a surface of a finite dielectric slab. Source is at $(x_s, y_s) = (0, -0.2226)$ m, and the field point is at $(x_o, y_o) = (-3, y)$ m. 105

5.12 Surface equivalent currents generated by a line source at $(x_s, y_s) = (-1, 0)$ m. 106

5.13 The total and scattered electric field generated by a line source outside a finite dielectric slab. Source is at $(x_s, y_s) = (-1, 0)$ m, and the field point is at $(x_o, y_o) = (-3, y)$ m. 107

5.14 The total and scattered electric field generated by a line source outside a finite dielectric slab. Source is at $(x_s, y_s) = (-2, 0)$ m, and the field point is at $(x_o, y_o) = (\cos\theta, \sin\theta)$ m. 107

6.1 A model for a finite reinforced concrete slab. There are N_c PEC rods (•) embedded in a finite dielectric slab with height $2L$ and thickness $2d$. An electric line source of strength I_s is placed at $\boldsymbol{\rho}_s$ to the left of the slab. 110

6.2 (a) Geometry of N_c rods inside a finite dielectric slab. Each rod has a diameter of $2a$ and placed at $x = d$. (b) Wire grid modeling of a rod with N_w wires. 111

6.3 (a) The equivalent exterior problem. (b) The equivalent interior problem. 114

6.4 The finite slab is divided into $2(M + N)$ cells. 117

6.5 The field scattered by a finite reinforced concrete slab. The source is at $(x_s, y_s) = (-0.2, 0)$ m, and the field point is at $(x_o, y_o) = (0.4\cos\theta, 0.4\sin\theta)$ m. $N_c = 5$ rods are inside a $2L \times 2d = 0.5 \times 0.2$ m finite dielectric slab. . 121

6.6 The field scattered by a finite reinforced concrete slab, calculated by the MoM/GF technique. The source is at $(x_s, y_s) = (-0.2, 0)$ m, and the field point is at $(x_o, y_o) = (0.4\cos\theta, 0.4\sin\theta)$ m. 121

6.7 Comparing the scattered field by a finite and infinite reinforced concrete slab. The MoM/GF technique has been used. The source is at $(x_s, y_s) = (-0.2, 0)$ m, and the field point is at $(x_o, y_o) = (0.4\cos\theta, 0.4\sin\theta)$ m. The finite slab size is $2L \times 2d = 0.5 \times 0.2$ m. $N_c = 5$ rods were placed inside the finite and infinite slab. 122

6.8 (a) The comparison of the scattered field by the wires inside a finite and infinite dielectric slab. (b) The comparison of the scattered field by the finite and infinite dielectric slab. 123

6.9 The scattered field for a finite reinforced concrete slab. The source is at $(x_s, y_s) = (-2, 0)$ m, and the field point is at $(x_o, y_o) = (\cos\theta, \sin\theta)$ m. $N_c = 19$ rods are placed inside a $2L \times 2d = 1 \times 0.2$ m finite dielectric slab. The rod spacing is $g = 5$ cm. 124

6.10 (a) The scattered field for the reinforced concrete slab. The scattered field consists of the contribution due to the wires and the slab without wires. The scattered field at $(x_o, y_o) = (\cos\theta, \sin\theta)$ m generated by a line source at $(x_s, y_s) = (-2, 0)$ m behind (b) a finite and infinite reinforced concrete slab, (c) the wires inside the finite and infinite dielectric slab, and (d) the finite and infinite dielectric slab when the wires are removed. The finite reinforced concrete model has a dimension of $2L \times 2d = 1 \times 0.2$ m in (a), (b), (c), and (d). The number of rods $N_c = 19$ is used. The rod spacing is $g = 5$ cm. 125

6.11 The scattered field for a finite reinforced concrete slab. The source is at $(x_s, y_s) = (-2, 0)$ m. $N_c = 33$ rods are placed inside a $2L \times 2d = 5 \times 0.2$ m finite dielectric slab. The rod spacing is $g = 15.24$ cm. The field point is at (a) $(x_o, y_o) = (-3, y)$ m, (b) $(x_o, y_o) = (3, y)$ m. 127

6.12 (a,b) The scattered field for the reinforced concrete slab. The scattered field consists of the contribution due to the wires shown in (c-d), and the contribution due to the slab without wires shown in (e-f). The scattered field (a,c,e) at $(x_o, y_o) = (-3, y)$ m and (b,d,f) at $(x_o, y_o) = (3, y)$ m. The finite slab dimension is $2L \times 2d = 5 \times 0.2$ m. $N_c = 33$ rods are placed inside the dielectric slab. The rod spacing is $g = 15.24$ cm. The source is at $(x_s, y_s) = (-2, 0)$ m. 128

6.13 Effect of the rod spacing on the average of the transmitted electric field along the line $(x_o, y_o) = (3, -2.5 < y < 2.5)$ m. $N_c = 33$ rods are placed inside an infinite dielectric slab. 129

6.14 Comparing the transmitted electric field through identical finite and infinite reinforced slab. The source is at $(x_s, y_s) = (-2, 0)$ m, and the field point is at $(x_o, y_o) = (3, y)$ m. $N_c = 33$ rods are placed with a spacing of $g = 0.1057$ m inside the finite and infinite slab. The finite slab length is $2L = 5$ m. 130

6.15 The transmitted electric field at $(x_o, y_o) = (3, y)$ m. The source is at $(x_s, y_s) = (-2, 0)$ m. $N_c = 65$ rods are placed inside a $2L \times 2d = 10 \times 0.2$ m finite dielectric slab. The rod spacing is (a) $g = 0.1524$ m, (b) $g = 0.1057$ m. 130

6.16 The transmitted field for normal incidence. The source is at $(x_s, y_s) = (-2, 0)$ m, and the field point is at $(x_o, y_o) = (x, 0)$ m. $N_c = 65$ rods are placed inside the finite and infinite slab. The finite slab dimension is $2L \times 2d = 10 \times 0.2$ m. 131

A.1 (a) An electric line source inside a dielectric slab backed by a PMC ground plane. (b) A line source and its image with respect to $x = d$ inside a dielectric slab. 145

A.2 (a) An electric line source inside a dielectric slab backed by a PEC ground plane. (b) A line source and its image with respect to $x = d$ inside a dielectric slab. 146

A.3 Dielectric slab backed by PMC. 146

A.4 Dielectric slab backed by PEC. 150

A.5 Reciprocity theorem is applied to obtain the electric field E_{z2} generated by (a) a y-directed magnetic line source M_{y2}, and (b) a x-directed magnetic line source M_{x2}. 154

A.6 (a)Geometry of a rectangular box enclosing a line source at $\boldsymbol{\rho}_n$ with strength I_s. (b) A magnetic line dipole of strength M_s in front of a cell. 156

A.7 Complex w-plane shows the path of integration $\overline{S}$. The LW poles ($\otimes$) and SW poles ($\times$) are shown on this plane 162

List of Tables

3.1 Locations of the PMC poles of G_x on the w plane. 52

List of Abbreviations

1D	One-Dimensional
2D	Two-Dimensional
3D	Three-Dimensional
A-IE	Aperture Integral Equation
E-PMCHWT	Electric Field Integral Equation-PMCHWT
EDC	Effective Dielectric Constant
EFIE	Electric Field Integral Equation
F-IE	Fringe Integral Equation
FD	Finite Difference
FDTD	Finite Difference Time Domain
FEM	Finite Element Method
FS	Finite Dielectric Slab
GF	Green's Function
GF/MoM	Green's Function/Method of Moments
GSM	Generalized Scattering Matrix
GTD	Geometrical Theory of Diffraction
LW	Leaky Wave
MoM	Method of Moments
MTL	Modal Transmission-Line

PEC	Perfect Electric Conductor
PMC	Perfect Magnetic Conductor
PMCHWT	Poggio-Miller-Chang-Harrington-Wu-Tsai
PML	Perfect Matched Layer
PO	Physical Optics
RBC	Radiation Boundary Condition
S-SIS	Separable Semi-Infinite Dielectric Slab
SDP	Steepest Descent Path
SIE/MoM	Surface Integral Equation/Method of Moments
SIS	Semi-Infinite Dielectric Slab
SS	Separable Dielectric Slab
SW	Surface Wave
SWP	Surface Wave Poles
TE	Transverse Electric
TM	Transverse Magnetic
UHF	Ultra High Frequency
VIE/MoM	Volume Integral Equation/Method of Moments

Chapter 1

Introduction

In the study of indoor radio propagation at UHF and above, a problem of interest is the propagation modeling of the environment in the vicinity of reinforced concrete structures. In this type of modeling, the source and field points are usually in the near field of the structure which is electrically large.

The concrete structures are usually reinforced by embedding metallic bars, and they are known as reinforced concrete. The metallic bars inside the concrete provide more strength to the structure. The reinforced concrete slabs are conventionally designed in the indoor environments to carry the load of the buildings. They are also popular because of their fire-resistive behavior. The reinforced concrete is mainly used in the ceilings, walls, floors and the columns in tall buildings and high-rises.

When the incident electromagnetic field propagates through the reinforced concrete slab, the metallic bars can block a portion of the transmitted field like a shield. Although this shielding is helpful in case of interference, it might cause a problem for a radio link to function. The metallic rods can also increase the reflected electric field depending on their physical geometry. This is not usually desired when multi-path fading is a problem because of highly reflected signal.

Since the presence of embedded metallic bars can highly affect the reflection and transmission properties of the walls and ceilings, an accurate modeling should account for these reinforcement bars. Although this usually increases the complexity of the model, it provides the correct propagation characteristics of the reinforced concrete for the study of indoor wave propagation.

1.1 Problem Statement

Fig. 1.1 shows an array of metallic bars inside a concrete slab representing a simple reinforced concrete slab. The concrete slab is modeled by a one layer dielectric medium enclosing the metallic bars. The metallic bars are parallel to the z axis. Since this structure is usually electrically large and thick above UHF, the source and the field points are often in the near field of such a model. As a result, the plane wave reflection and transmission properties of such a structure cannot predict the scattering properties of the reinforced concrete correctly. A better approach is to assume a

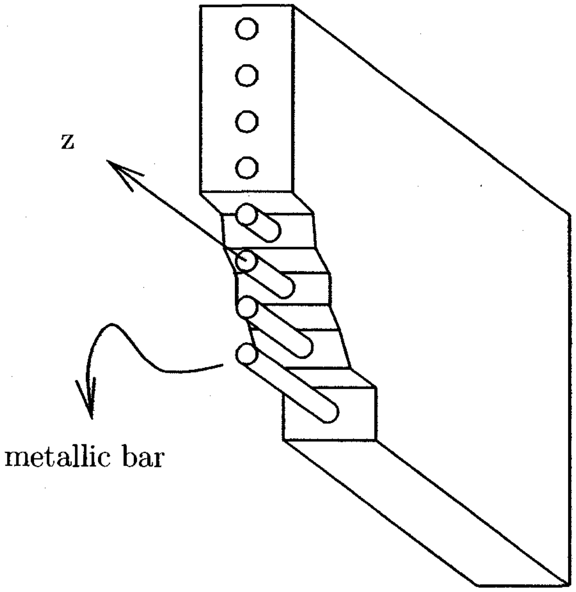

Figure 1.1: A reinforced concrete slab.

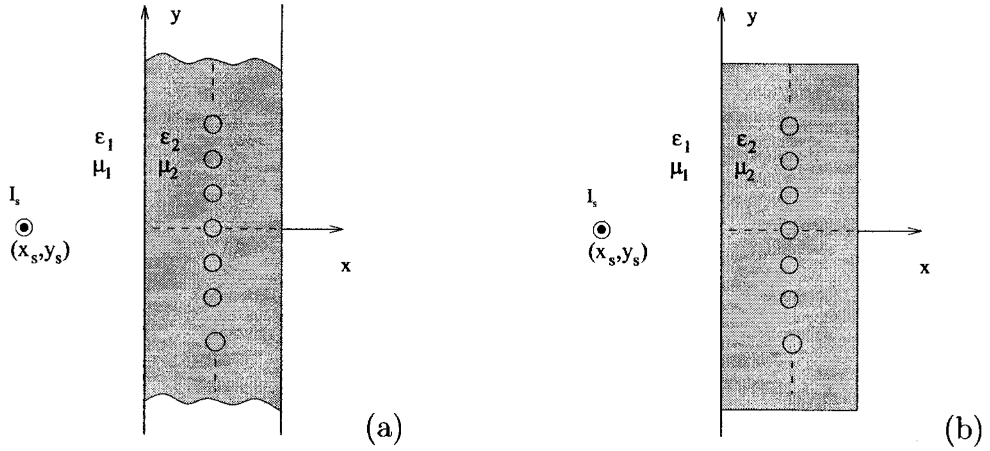

Figure 1.2: (a) A two-dimensional infinite dielectric slab embedding metallic bars. (b) A two-dimensional finite dielectric slab embedding metallic bars.

cylindrical wave originating from a line source in the near field region of the slab. By doing so, we assume that the slab and metallic bars are infinitely long in the z direction. A problem of interest is to model this structure when the slab is also infinitely long in the y direction as shown in Fig. 1.2.a. This is referred to as infinite dielectric slab. The concrete, which is modeled by a homogenous lossy dielectric material, is characterized by the permittivity ϵ_2 and permeability μ_2. Since the exterior region is usually air, we have $\epsilon_1 = \epsilon_0$ where ϵ_0 is the free space permittivity. The materials are also assumed to be non-magnetic, so $\mu_1 = \mu_2 = \mu_0$, where the free space permeability is denoted by μ_0. An electric line source of strength I_s which is located outside the dielectric slab at (x_s, y_s) generates a TM_z field (transverse magnetic field to the z direction).

The model shown in Fig. 1.2.a can be improved by letting the slab have a finite length in the y direction. This model is presented in Fig. 1.2.b which shows the slab cross section in the x-y plane.

1.2 Approach

The accurate full wave computational techniques such as method of moments or finite elements usually fail to model an electrically large structure such as reinforced concrete on a standard desktop personal computer. The finite elements and method of moments are highly dependent on the electrical size of the structure because these approaches usually use volume or surface meshing for solving problems. The mesh size which is directly related to the size of the structure defines the number of unknowns in a system of equations. As a result, the memory size used for solving the system of equations is directly related to the size of the structure.

In modeling the reinforced concrete, the main challenge is to adopt an accurate method with the minimum number of unknowns. This requires applying a hybrid approach which usually combines a full-wave electromagnetic technique and an asymptotic method for analyzing large structures.

If we model the concrete slab as a one-layer homogeneous dielectric medium, it is possible to find the electric field generated by a current element in front of the slab by means of an exact expression called a "Green's function." A hybrid method called the Green's function/method of moments (GF/MoM) can then be used to solve for the induced currents on any scatterer inside/outside of the dielectric slab. The reader is referred to [1] for an overview of the GF/MoM technique. The hybrid GF/MoM combines method of moments (MoM) and Green's function (GF). The MoM is used for computing the induced currents on the scatterer bodies which are the metallic bars in our problem. In doing so, the scatterer bodies are first replaced by their unknown equivalent surface currents. This can be done by applying the surface equivalence principle. As a result, the medium becomes homogeneous and has an exact solution by means of a GF. The moment method then uses the Green's function to solve for the unknown equivalent currents which had replaced the metallic bars.

It is noted that the dielectric slab in the GF/MoM is not part of the scatterer body solved by MoM since the Green's function formulation accounts for the presence of the slab. As a result, the GF/MoM is more efficient than the full wave MoM in which the dielectric body is part of the scatterer that we wish to model.

A key step in GF/MoM formulation is having the Green's function for the dielectric slab. The Green's function for an infinite dielectric slab is already available in the literature [2]. It would be necessary to develop a GF model for a thick finite slab (FS), as shown in Fig. 1.2.b.

As a first step towards this goal, this thesis develops a Green's function for the finite and thick dielectric slab. The first development assumes that the source and field points are inside the slab, i.e. the interior problem. To obtain the interior GF, we first find the exact GF for the separable dielectric slab (SS) problem, which is closely related to the FS. The solution for the SS problem is expressed in terms of a discrete spectrum of surface wave (SW) poles plus the remaining part which we call the "residual wave." Since the SS solution fails to model the FS when the slab size is close to resonance, we modify the SW part of the solution by correcting the end cap reflection coefficient for each guided mode and accounting for the end cap mode conversion. The mode conversions and reflections are characterized by the end cap scattering matrix which is obtained by the MoM. The interior GF solution for a FS is then the MoM-modified SW solution plus the residual wave contribution obtained for the SS problem.

It is noted that this interior Green's function can be used to obtain the Green's function solution for three other possible cases, i.e. the cases when the source and/or the field points are outside the FS. The solution for the cases when the source and/or field points are outside the FS is obtained using the interior GF and the surface equivalence principle.

Applying the surface equivalence principle, we can obtain the exterior field generated by an interior source. This can be done by computing the surface equivalent currents using the interior Green's function. The equivalent surface currents together with the free-space Green's function can be used to obtain the field at any point outside the slab. Applying the reciprocity theorem, we can interchange the source and the field point. As a result, we are able to calculate the interior field due to an exterior line source. This is used later for computing the exterior Green's function where we first obtain the electric and magnetic fields on the slab surface generated by an exterior line source. Having the electric and magnetic fields on the slab surface will provide the surface equivalent currents. These currents will be the sources of the scattered field in the exterior region.

After obtaining the GF for the FS, it is possible to apply the GF/MoM to a finite reinforced concrete slab. To validate the results obtained by the GF/MoM, we also model the finite reinforced concrete slab using the surface integral equation/method of moments (SIE/MoM) technique. In doing so, the SIE/MoM forms the electric field integral equation formulation before solving for the unknown currents on the slab surface and metallic bar surfaces.

1.3 Basic Assumptions

The modeling of the finite reinforced concrete in this thesis involves some necessary assumptions which are clarified here. The assumptions explained in this section are necessary for simplifying the structure which we wish to model.

The concrete material is assumed to be homogeneous. As a result, the concrete is modeled by a one layer medium filled with homogeneous and isotropic material.

It is also assumed that the metallic bars are perfect conductors. As a result, the conductor loss due to the metallic bars is not accounted for in our model. A minor modification would be needed for considering such a configuration.

All the models in this thesis are assumed to be two-dimensional (2D). As a result, the electric and magnetic fields have no variations along the length of the metal bars. The model here also assumes that the metallic bars and concrete surfaces have no roughness.

Although the metallic bars can have any cross section in the model, we just show the results for the cases where each rod has a circular cross section. The metallic bars are assumed to be electrically thick. It is also noted that the metallic bars can be placed anywhere inside the slab. However, the results shown here are provided for the cases where the metallic bars are at the center line of the slab, and the adjacent bars are equally spaced.

The 2D model is able to treat parallel bars but not crossed bars that occur in actual reinforced concrete. This approximation is somewhat justified by the fact that electromagnetic scattering by a 3D wire grid is dominated by the wires that are parallel to the incident electric field. For the more general case of 3D oblique incidence, a model with parallel bars would not be sufficient.

The sinusoidally time-varying fields are considered in this thesis where the time variations is represented by $e^{j\omega t}$ and suppressed.

1.4 Document Overview

The materials in this document is presented as follows. Chapter 2 explains the problem background and summarizes the works already completed by others. Chapter 3 presents the interior Green's function solution for a separable dielectric slab. In this chapter, the resonance property of the separable dielectric slab is also studied. The generated results for the separable slab are shown at the end of this chapter. Chapter 4 first carries out the calculation of the scattering matrix at the end cap of a semi-infinite dielectric slab. Next, this chapter describes the generalized scattering matrix (GSM) method which is used to obtain the solution for a thick finite slab.

Chapter 5 carries out the calculation of the Green's function when the field point and/or the source are outside the dielectric slab using the interior Green's function. Chapter 6 presents the analysis of the finite reinforced concrete slab using GF/MoM and SIE/MoM techniques. Chapter 7 gives a conclusion and discusses the potential future research topics.

Chapter 2

Background and Literature Review

The literature survey which is performed briefly in this chapter will review the topics related to the area of research presented in this thesis. First, the review will address the approaches applied to a finite dielectric slab. Next, the methods applied for modeling a reinforced concrete slab are discussed.

2.1 Finite Dielectric Slab

As it was mentioned in Section 1.2, the key step in applying the GF/MoM to a finite reinforced concrete is having the Green's function for a finite dielectric slab. However, an exact closed-form analytical solution for a finite dielectric slab is not available in the literature yet. As for an approximate solution, there have been several publications addressing this problem in the literature which will be reviewed here.

A well-known study by Marcatili [3] used the separation of variables method to obtain an approximate solution for the guided modes in rectangular-core dielectric waveguides. He used this method to accurately calculate the propagation constants away from the cut-off. However, the field distribution inside the dielectric slab was not studied.

An approximate approach known as effective dielectric constant (EDC) method was used by Knox *et al.* [4] to model the rectangular-core dielectric waveguide. In the EDC method which is very similar to the Marcatili approach, the refractive index of the dielectric core n_2 is replaced by an effective refractive index n_{eff} defined as

$$\mathrm{n}_{eff}^2 = \mathrm{n}_2^2 - \frac{\eta_2^2}{k_2^2} \tag{2.1.1}$$

where η_2 is the propagation constant in the y direction (perpendicular to the dielectric core extent), and k_2 is the dielectric slab wave number. This approximate method improved the Marcatili's technique while computing the propagation constant of the modes near cut-off.

Although Marcatili's separation of variables formulation cannot solve the finite dielectric slab (FS) problem, it does solve another closely related structure which we call the separable dielectric slab (SS). The interior of this equivalent structure is the same as the original FS problem; however, applying the separation of variables technique to the dielectric region forces boundary conditions in the four exterior corner regions that do not match the FS that we wish to model.

An approximate solution for a FS can be obtained by applying physical optics (PO) and using the equivalent volume polarization currents, whereby the currents in the finite and infinite slabs are assumed to be identical. Bokhari *et al.* [5] applied the PO approximation to calculate the radiation pattern of a patch antenna on a finite size substrate. Maci *et al.* [6] also used the PO approximation with volume equivalent currents, and developed the asymptotic expression to account for the diffraction by a semi-infinite grounded dielectric slab. (The expression which relates the diffracted field to the incident field at the end cap is known as diffraction coefficient.) The PO approach is more efficient for thin slabs and the far-field region. However, it does not include the surface wave (SW) reflections at the end caps.

A more accurate approach is to use an integral equation technique. This has been applied by Maci *et al.* [7] and Volski and Vandenbosch [8] in order to obtain the diffraction by a semi-infinite grounded dielectric slab. These approaches formulate the integral equations by enforcing the continuity of the electric field on an infinite aperture plane at the end cap. This is referred to as aperture integral equation (A-IE) method. Although this technique requires solving a system of equations, the number of unknowns is much less than the number of unknowns when using surface or volume integral equation for the entire structure. Both these works were applied to the case of a thin semi-infinite grounded dielectric slab.

The integral equation approach has also been applied to a 2D semi-infinite grounded dielectric slab by Jorgensen *et al.* [9]. To obtain the diffracted field by the end cap of the semi-infinite slab, they extracted the equivalent surface current on the infinite slab from the equivalent currents on the semi-infinite slab when the two slabs were illuminated by the same source. After forming the integral equations which they called fringe integral equation (F-IE), they applied MoM by using the pulse and entire domain basis functions. This let them solve for the equivalent surface currents induced on the surface because of the end cap. The results shown in their work were obtained for the thin dielectric slab case which guided one surface wave mode.

Shishegar and Faraji-Dana [10] developed an approximate Green's function solution for the FS by applying the complex image technique and using plane wave Fresnel reflection coefficients at the end caps. This is a good assumption if the incident field is mostly reflected at the air-dielectric boundary. It will be shown in this thesis that this is a good assumption if the surface waves in the slab do not experience a resonance. It was found that their result was not satisfactory for a high refractive index, so they suggested a mode matching technique to correct the reflection coefficients at the end caps. Their results were limited to the case of a thin dielectric slab supporting a single guided mode.

The mode matching technique has been applied by Derudder *et al.* [11] to a 2D semi-infinite dielectric slab. In this numerical approach, the slab is placed inside a parallel plate waveguide. Inside the waveguide, the parallel plates are covered with perfect matched layers (PML's). As a result, the slab problem which is an open structure problem is converted into a waveguide problem. An open structure has both a continuous and discrete modal spectrum, but a closed structure only has a discrete modal spectrum known as guided modes. In addition to the guided modes inside the air-filled parallel plate waveguide, extra types of guided modes known as Berenger modes are inside the waveguide because of the PML layer. The mode matching technique enforces the boundary condition which is the continuity of the tangential field components on the aperture plane containing the end cap. This technique is accurate when the knowledge of the possible excited guided modes at the matching aperture is provided.

In order to investigate the propagation characteristics of the wave inside a rectangular dielectric rod, Goell [12] used a numerical approach based on the point matching technique on the rod surface. In this technique, the fields inside and outside the dielectric rod are expressed in terms of a series of circular harmonics. By applying the point matching technique on the rod surface, the inside fields are matched to the outside fields at finite number of points on the surface. Furthermore, a finite number of harmonics is used for the interior and exterior field expansion. Cullen *et al.* [13] later investigated the fields mismatch on the boundary of a rectangular rod, by using the Goell technique. For reducing the mismatch on the boundary, they showed that it is better to have a matching point at the edge of the dielectric rod when the match points are equiangularly spaced. Applying the Goell approach to a large dielectric slab is not efficient since a large number of terms in the expansion series are needed for accurate modeling.

An accurate numerical approach based on a volume integral equation/method of moment (VIE/MoM) technique was applied to a 2D arbitrary cross-section shape dielectric cylinder by Richmond [14]. He extended this later to a thin dielectric slab [15] using the entire domain basis and weighting functions. In the VIE/MOM, the dielectric region is divided into small cells. The dielectric region can be replaced with the unknown equivalent volume polarization-currents. The unknown currents are obtained by applying the boundary condition on the dielectric region and solving a system of equations. Since the number of unknown currents is directly related to the size of the dielectric slab, this approach is computationally efficient for thin dielectric slabs. When the dielectric slab becomes electrically thick and large, a standard desktop computer fails to solve the problem using VIE/MoM.

A better and more efficient MoM approach is the SIE/MoM which was applied to a 2D arbitrary cross-sectioned dielectric cylinder by Wu *et al.* [16]. This technique is also known as Poggio-Miller-Chang-Harrington-Wu-Tsai (PMCHWT) method [17] [18] [19] [20] when the electric and/or magnetic field integral equations are used. This approach is more efficient since the number of unknown equivalent surface currents only depends on the surface area of the homogeneous dielectric body. This also has been extended to a problem of a conducting body inside a dielectric scatterer by Kishk [21] *et al.* who called it E-PMCHWT (electric field integral equation-PMCHWT). In this formulation, the electric field integral equation is formed on the surface of the conductor.

Although the SIE/MoM is more efficient for modeling a homogeneous dielectric body than VIE/MoM, the SIE/MoM formulation is usually more complex than VIE/MoM formulation. Furthermore, the VIE/MoM can be applied easier when the dielectric is inhomogeneous.

An accurate numerical approach based on finite element technique was applied by Rahman *et al.* [22] to model a dielectric slab problem. The finite element method is differential-equation-based, and it solves the problems in the frequency domain. Applying the 2D finite element, the region of interest is divided into finite number of triangular subregions. Unlike the integral equation technique where the region of unknown currents is limited to the surface or interior region of the scatterer, the region of interest of unknown fields in finite element is extended to a region outside the scatterer. The boundary of this extended region is usually terminated by an artificial boundary wall called radiation boundary condition (RBC) as explained in [23] and [24]. The RBC walls should usually be far enough from the scatterer so that they do not affect the fields inside the scatterer. Since this makes the number of finite elements large, this technique is not efficient for modeling a large structure on a standard desktop computer. However, an advantage of the finite element approach is its matrix sparsity, unlike the integral equation techniques which should solve a dense matrix.

A 2D finite-difference (FD) method was applied to a rectangular dielectric guiding structure by Schweig *et al.* [25]. Using this technique, the region of interest should first be confined. In doing so, the dielectric slab is placed inside a box with electrically large conducting walls so that the conducting walls do not affect the guided modes inside the dielectric slab. For simplicity, the region of interest is usually divided into square cells. Comparing the FD with finite element approach, the FD technique is easier to implement and its formulation involves less complexity. Although the FD approach requires half as much computer storage as finite element, it is not efficient for modeling an arbitrarily shaped and large structure.

A high frequency technique based on geometrical theory of diffraction (GTD) was developed by Burnside *et al.* [26] for modeling a thin lossless dielectric slab.

Applying the GTD, the scattered field is written in terms of diffracted, reflected and transmitted fields. The diffracted field is obtained in order to compensate for the field discontinuity associated with the incident and reflection shadow boundaries. This GTD technique is computationally efficient, but it is limited to a case of thin slab with a thickness less than a quarter wavelength.

In this thesis, a hybrid approach based on the Green's function technique and MoM was developed [27] [28] for modeling a finite and thick dielectric slab. This technique, which will be presented in detail, is computationally efficient since it can be applied to an electrically large and thick dielectric slab.

2.2 Reinforced Concrete

In modeling reinforced concrete, the concrete is often represented by a homogeneous dielectric slab of infinite transverse extent, and the reinforcement is formed by an array of metallic bars or wires embedded in the dielectric slab. It is sometimes computationally efficient to assume a periodicity property for modeling the reinforcement. This implies an infinite number of metallic bars placed periodically inside the dielectric slab.

Using the periodicity property and applying the modal transmission-line (MTL) technique, Savov *et al.* [29] modeled the plane wave transmission coefficient of a 2D reinforced concrete slab. In this technique, the reinforced concrete is modeled by a three layer medium. To fit the wires in the center layer, this approach assumes square cross-section wires for simplicity. As a result, the center layer becomes a periodic structure surrounded by two homogeneous layers. The tangential fields at the boundary of each layer is expanded in term of Floquet space-harmonics as a result of the periodicity property. This series of harmonics forms an infinite number of modes. The infinite series should be truncated so that the eigenvalue equation can be written in a matrix form accounting for a finite number of modes. Using this technique, it is usually hard to estimate the needed number of modes for obtaining an accurate result. Furthermore, this approach only solves the problem when a plane wave incident field is assumed.

Applying the finite element technique and expanding the fields in terms of Floquet's modes, Richalot *et al.* [30] studied the transmission coefficient of reinforced concrete. Using this model, they only investigated the slab embedding thin wires by assuming the wire diameters of 2-4 mm at 900 MHz and 1.8 GHz. Although they used thin wires, they showed that the effect of the wires cannot be neglected at 1.8 GHz. Their technique could only calculate the transmission coefficient for plane wave incidence.

Assuming the periodic characteristics of the structure, Chia [31] investigated the reflection characteristics of the reinforced concrete using the Floquet modal theorem. In this study, plane wave incidence was assumed.

Dalke *et al.* [32] used a finite-difference time-domain (FDTD) method to determine the reflection and transmission properties of various reinforced concrete walls at commonly used radio frequencies over a range of 100-6000 MHz. The reflection and transmission coefficients were studied when the wires inside the concrete had a lattice configuration, i.e. a 2D grid of wires. The lattice configuration modeled the wires parallel and perpendicular to the incident field. They showed that for a thick reinforced wall, the transmission coefficient can become much larger than the predicted transmission for the rebar structure in free space. Their study was based on assuming a normal incidence plane wave.

The FDTD technique was also used by Bin *et al.* [33] for modeling reinforced concrete. Their model could compute the shielding effectiveness of reinforced concrete in high power electromagnetic environments. They studied single and double-layered reinforced concrete for wideband pulse waves. Using the periodicity property of the reinforced concrete, they applied Floquet periodic boundary conditions. In indoor propagation, the shielding effectiveness is defined as

$$SE = 20 \log \frac{E_{op}}{E_{cp}}$$

where E_{op} is the electric field at a certain point when the wall is not present, and E_{cp} is the electric field at the same point with the presence of the shielding.

Using a 2D FDTD approach, Elkamchouchi *et al.* [34] also studied the shielding effectiveness of reinforced concrete with a sinusoidal point source. They investigated convex, concave, and plane reinforced concrete walls. Their results showed the effect of wall thickness, wire spacing and wire radius on the shielding effectiveness.

Using ray tracing models and the empirical transmission data, Pena *et al.* [35] estimated the equivalent electric parameters ϵ and σ of the brick and doubly reinforced concrete walls at 900-MHz. This required a knowledge of transmitted field measurement data through walls.

Penetration loss measurements for different reinforced concrete wall thicknesses were made by Zhang *et al.* [36]. They measured penetration loss over the frequency range of 900 MHz to 18 GHz.

Arnold *et al.* [37] measured copolarized attenuation at 815 MHz within two different buildings and between floors constructed with reinforced concrete. When the transmitter and receiver were on the adjacent floors, they measured cross-floor isolation of approximately 26 dB at 150 ft distance for the mean of the signal. However, they observed a more than 20 dB variation in the instantaneous signal level. They used the "raster-scan" technique for median signal level measurements.

Bihua *et al.* [38] investigated the shielding effectiveness of reinforced concrete for pulse shape plane wave incidence experimentally. In their work, they concluded that the shielding effectiveness improves by increasing the wire radius and decreasing the grid cell size although this does not agree with the "same surface area" rule of thumb. According to the "same surface area" rule, the best shielding is when the total surface area of the wires is equal to the cross-section area of the slab parallel to the wire grid.

A 2D GF/MoM approach has been developed by Paknys [2] to model the reflection and transmission properties of reinforced concrete. The case of thick wires was later examined by Parsa and Paknys [39]. In this technique, the Green's function of the dielectric slab which is in the form of Sommerfeld integrals is evaluated numerically and asymptotically. By using the dielectric slab Green's function, the number of unknowns solved in the GF/MoM technique has been greatly reduced compared to the full wave MoM approach. Furthermore, the number of unknowns in the GF/MoM method is independent of the slab thickness, unlike the full wave techniques like MoM, FEM and others. Applying the GF/MoM approach, the number of unknowns only depends on the number of metallic bars. As a result, the GF/MoM is computationally more efficient than full wave methods which model the whole structure including the dielectric slab. Using the full wave techniques, the computational cost for modeling the dielectric slab can be high since the slab is usually several wavelengths thick at UHF and above.

Chapter 3

An Exact Interior Green's Function Solution for a Separable and Finite Dielectric Slab

To model a finite dielectric slab, we need to solve the wave equation subject to the boundary conditions for the tangential electric and magnetic field on the surface of the dielectric slab. The Green's function is a solution to the boundary value problem for a point source excitation of unit strength. Up to now, there is no exact closed-form analytical solution available for a finite dielectric slab. The reason is that the finite dielectric slab is not a separable structure. If we use the separation of variable method and impose the boundary condition on the surface of the dielectric, the solution imposes undesirable boundary conditions at the corner regions outside the slab that do not match the problem that we want to solve. The boundary conditions at the corner regions represent certain materials in the corner regions. This structure is referred to as separable dielectric slab which is presented in this chapter. The work has been reported in [27].

3.1 Separation of Variables

In this section, we follow the the separation of variables method [40] [41] to solve the inhomogeneous Helmholtz equation. In electromagnetic problems, time harmonic electric field ($\overline{E}$) must satisfy

$$(\nabla^2 + k^2)\overline{E} = j\omega\mu\overline{J} - \frac{\nabla\nabla \cdot \overline{J}}{j\omega\epsilon} + \nabla \times \overline{M} \tag{3.1.1}$$

where ϵ is permittivity, μ is permeability, and $\overline{J}$ and $\overline{M}$ are electric and magnetic current density, respectively. Time variation is represented by $e^{j\omega t}$ and suppressed. We assume a 2D problem and TM_z polarization. This means that the electric field has only a z component ($E_x = E_y = 0$) with no z-variation ($\partial E_z/\partial z = 0$). This assumption reduces (3.1.1) to

$$(\frac{\partial^2}{\partial x} + \frac{\partial^2}{\partial y} + k^2)E_z = j\omega\mu J_z \tag{3.1.2}$$

which is a scalar inhomogeneous wave equation. Using the vector potential A and knowing that $E = -j\omega\mu A$ leads to

$$(\frac{\partial^2}{\partial x} + \frac{\partial^2}{\partial y} + k^2)A_z = -J_z. \tag{3.1.3}$$

To solve this inhomogeneous partial differential equation, we develop a Green's function (G) which is the solution due to a unit line source at (x_s, y_s). The Green's function must satisfy the unit impulse source-excited partial differential equation

$$(\nabla^2 + k^2)G(x, y; x_s, y_s) = -\delta(x - x_s)\delta(y - y_s) \tag{3.1.4}$$

and the same boundary condition as A. Having the solution due to the unit impulse, represented by G, we can obtain the electric field generated by any current distribution as

$$E_z = -j\omega\mu J_z * G \tag{3.1.5}$$

where the asterisk denotes the convolution. To solve the inhomogeneous partial differential equation (3.1.4), the proposed solution, also known as an "ansatz" is

$$G(x, y; x_s, y_s) = \mathcal{K}[G_x(x, x_s)G_y(y, y_s)] \tag{3.1.6}$$

where $\mathcal{K}$ is a linear operator, to be determined. We should define the linear operator $\mathcal{K}$. Substituting (3.1.6) in (3.1.4), we can write

$$\mathcal{K}[G_y\frac{d^2G_x}{dx^2} + G_x\frac{d^2G_y}{dy^2} + k^2G_xG_y] = -\delta(x - x_s)\delta(y - y_s). \tag{3.1.7}$$

We can assume that $k^2 = k_0^2\epsilon(x, y)$ where $\epsilon(x, y)$ represents the dielectric constant in cartesian coordinates. k_0 is a constant defined by $k_0 = \omega\sqrt{\epsilon_0\mu_0}$ where ϵ_0 and μ_0 are free space permittivity and permeability, respectively. We assume that

$$\epsilon(x, y) = \epsilon_x(x) + \epsilon_y(y) \tag{3.1.8}$$

and postulate that (3.1.4) is separable into two 1D Helmholtz equations as

$$\frac{d^2G_x}{dx^2} + (\lambda_x + k_0^2\epsilon_x)G_x = -\delta(x - x_s) \tag{3.1.9}$$

$$\frac{d^2G_y}{dy^2} + (\lambda_y + k_0^2\epsilon_y)G_x = -\delta(y - y_s). \tag{3.1.10}$$

Using (3.1.9) and (3.1.10) in (3.1.7) to replace the derivatives, we can write

$$\mathcal{K}[G_x G_y(-\lambda_x-\lambda_y-k_0^2(\epsilon_x+\epsilon_y)+k^2)-G_y\delta(x-x_s)-G_x\delta(y-y_s)] = -\delta(x-x_s)\delta(y-y_s). \tag{3.1.11}$$

If we impose

$$\lambda_x + \lambda_y = 0 \tag{3.1.12}$$

$$k_0^2(\epsilon_x + \epsilon_y) = k^2 \tag{3.1.13}$$

then (3.1.11) simplifies to

$$\mathcal{K}[G_y\delta(x-x_s) + G_x\delta(y-y_s)] = \delta(x-x_s)\delta(y-y_s). \tag{3.1.14}$$

From the theorem presented in [40] for one-dimensional Green's functions, we know that

$$\frac{1}{2\pi j}\oint_{C_y} G_y(y, y_s, \lambda_y)d\lambda_y = -\delta(y-y_s) \tag{3.1.15}$$

where the closed contour C_y encloses all the singularities of G_y in the complex λ_y plane, in a counterclockwise direction. Because the closed contour C_y doesn't encircle the singularities of G_x, we can write that

$$\frac{1}{2\pi j}\oint_{C_y} G_x(x, x_s, \lambda_y)d\lambda_y = 0 \tag{3.1.16}$$

and propose that the linear operator $\mathcal{K}$ has a form of

$$\mathcal{K} = K\oint_{C_y}[.]d\lambda_y \tag{3.1.17}$$

where the constant K should be obtained. Using the linear operator $\mathcal{K}$ in (3.1.14) leads to

$$K \oint_{C_y} G_y d\lambda_y \delta(x - x_s) + K \oint_{C_y} G_x d\lambda_y \delta(y - y_s) = \delta(x - x_s)\delta(y - y_s). \qquad (3.1.18)$$

By applying (3.1.16), the second term on the left side of (3.1.18) is zero. Utilizing (3.1.15), we can rewrite (3.1.18) as

$$K(-2j\pi\delta(y - y_s))\delta(x - x_s) = \delta(x - x_s)\delta(y - y_s)$$

which determines the constant K in the linear operator as

$$K = -\frac{1}{2\pi j}.$$

Consequently, the solution for the two-dimensional Green's function problem given in (3.1.6) becomes

$$G(x, y; x_s, y_s) = -\frac{1}{2\pi j} \oint_{C_y} G_x(x, x_s, -\lambda_y) G_y(y, y_s, \lambda_y) d\lambda_y \qquad (3.1.19)$$

where G_x and G_y are one dimensional Green's functions and should satisfy the required boundary conditions. Note that λ_x can be expressed in terms of λ_y using (3.1.12).

Similarly, we can choose a linear operator in the form of

$$\mathcal{K} = -\frac{1}{2\pi j} \oint_{C_x} [.] d\lambda_x$$

which satisfies (3.1.14). Applying this operator to (3.1.6) and replacing λ_y by $\lambda_y =$

$-\lambda_x$ leads to an alternative solution as

$$G(x, y; x_s, y_s) = -\frac{1}{2\pi j} \oint_{C_x} G_x(x, x_s, \lambda_x) G_y(y, y_s, -\lambda_x) d\lambda_x \tag{3.1.20}$$

where C_x only encircles the singularities of G_x in the complex λ_x plane and does not enclose the singularities of G_y.

The singularities of the one dimensional Green's function can be in the form of poles and/or branch-cuts. The closed contour around the poles is usually presented in terms of discrete spectra according to the residue theorem. Moreover, the contour which encloses the branch cuts forms the continuous spectra. The path of integration can be deformed in any manner as long as it does not cross any poles or branch points. It should be noted that the integrand in (3.1.19) or (3.1.20) should have a decaying tail on the contour of the integration. This is important for performing the integration, whether numerically or asymptotically. In Section 3.3, we will apply the separation of variables to find an approximate Green's function for a finite extent dielectric slab. In the next section, the solution to the infinite extent dielectric slab problem will be presented.

3.2 Electric Line Source Inside an Infinite Extent Dielectric Slab Backed by a PMC or PEC

Fig. 3.3 shows a dielectric slab of thickness $2d$, having an infinite extent in the y direction. The dielectric slab has a permittivity of ϵ_2, surrounded by Region 1 which has a permittivity of ϵ_1. The permeability in both regions is assumed to be that of free space, μ_0. A current line source I_s is located inside the dielectric slab at (x_s, y_s), and generates the cylindrical wave. The infinite-extent slab was investigated by Paknys [2].

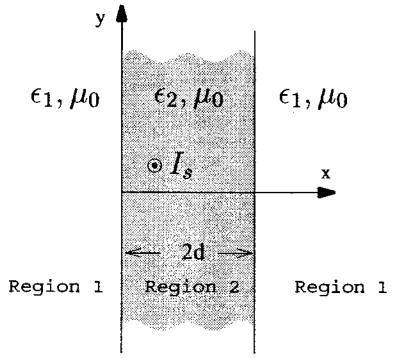

Figure 3.3: An infinite extent dielectric slab.

The present section contains analytical details that were not included in that paper. The dielectric slab solution can be obtained by solving the two problems shown in Fig. 3.4 as it is discussed in Appendix A.1. For any of the two problems shown in

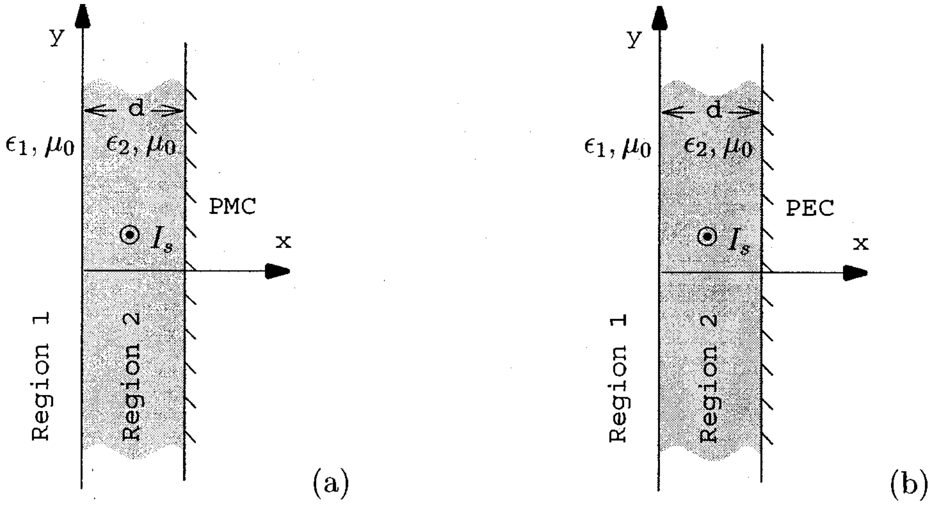

Figure 3.4: (a) Geometry of an infinite dielectric slab of thickness d grounded by a (a) PMC plane at $x = d$ (b) PEC plane at $x = d$.

Fig. 3.4, the Helmholtz equation should be satisfied by the Green's function

$$(\nabla^2 + k_{1,2}^2)G(x, y; x_s, y_s) = -\delta(x - x_s)\delta(y - y_s) \tag{3.2.1}$$

where $k_1 = k_0\sqrt{\epsilon_1}$ and $k_2 = k_0\sqrt{\epsilon_2}$. To apply the separation of variables, (3.1.13) can be written as

$$k_0^2\epsilon(x,y) = k_0^2(\epsilon_x(x) + \epsilon_y(y)) = \begin{cases} k_2^2 & 0 \leq x \leq d \\ k_1^2 & \text{elsewhere} \end{cases} \tag{3.2.2}$$

where $\epsilon(x,y)$ has been defined in (3.1.8). It can be noted that k_1 and k_2 do not have any variation with respect to y, so $\epsilon_y(y) = \epsilon_{y1}$ where ϵ_{y1} is an unknown constant. Moreover, we can write

$$\epsilon_x(x) = \begin{cases} \epsilon_{x2} & 0 \leq x \leq d \\ \epsilon_{x1} & \text{elsewhere} \end{cases} \tag{3.2.3}$$

where ϵ_{x1} and ϵ_{x2} are both constants to be defined. Using (3.2.2) and (3.2.3), we can obtain

$$\epsilon_{x1} + \epsilon_{y1} = \epsilon_1 \qquad \text{elsewhere} \tag{3.2.4}$$

$$\epsilon_{x2} + \epsilon_{y1} = \epsilon_2 \qquad 0 \leq x \leq d \tag{3.2.5}$$

which form a system of linear equations with an infinite number of solutions. We can choose $\epsilon_{y1} = 0$ and obtain $\epsilon_{x1} = \epsilon_1$ and $\epsilon_{x2} = \epsilon_2$. Using these dielectric constants in (3.1.9) and (3.1.10), we should solve

$$\frac{d^2G_x}{dx^2} + (\lambda_x + k_1^2)G_x = -\delta(x - x_s) \qquad x < 0 \tag{3.2.6}$$

$$\frac{d^2G_x}{dx^2} + (\lambda_x + k_2^2)G_x = -\delta(x - x_s) \qquad 0 \leq x \leq d \tag{3.2.7}$$

$$\frac{d^2G_y}{dy^2} + \lambda_y G_y = -\delta(y - y_s) \quad -\infty < y < \infty. \tag{3.2.8}$$

The boundary condition at $x = 0$ requires continuity of tangential electric and magnetic fields which implies that G_x and $\frac{1}{\mu_0}dG_x/dx$ should be continuous. For solving the problem of a dielectric backed PEC, imposing the boundary condition at $x = d$ requires zero tangential electric field or $G_x = 0$. Similarly, the tangential magnetic field should vanish on the PMC sheet or $dG_x/dx = 0$. The Appendices A.2 and A.3 present the derivation of Green's functions for the dielectric slab problem backed by PEC and PMC, denoted by G_{22}^e and G_{22}^m. The notation G_{22} which represents the interior Green's function indicates that both source and observation points are inside the dielectric slab in Region 2. The 1D solution of (3.2.6) and (3.2.7) according to the Appendices A.2 and A.3 becomes

$$G_{22x}^m = \frac{j\kappa_1 \sin \kappa_2 x_< + \kappa_2 \cos \kappa_2 x_<}{j\kappa_1 \cos \kappa_2 d - \kappa_2 \sin \kappa_2 d} \cdot \frac{\cos \kappa_2 (d - x_>)}{\kappa_2} \tag{3.2.9}$$

$$G_{22x}^e = \frac{j\kappa_1 \sin \kappa_2 x_< + \kappa_2 \cos \kappa_2 x_<}{j\kappa_1 \sin \kappa_2 d + \kappa_2 \cos \kappa_2 d} \cdot \frac{\sin \kappa_2 (d - x_>)}{\kappa_2} \tag{3.2.10}$$

where $x_<$ denotes smaller of x_s or x, and $x_>$ is the larger. It is noted that $0 \leq (x_s, x) \leq d$, and we have

$$\kappa_1 = \sqrt{\lambda_x + k_1^2} \tag{3.2.11}$$

$$\kappa_2 = \sqrt{\lambda_x + k_2^2}. \tag{3.2.12}$$

The 1D solution for (3.2.8) which satisfies the radiation condition is free space Green's function [40], known to be

$$G_y = \frac{e^{-j\sqrt{\lambda_y}|y-y_s|}}{j2\sqrt{\lambda_y}}. \tag{3.2.13}$$

The two dimensional Green's functions can be constructed by using (3.1.19) and (3.1.12) which becomes

$$G_{22}^{m,e} = -\frac{1}{2\pi j} \oint_{C_y} G_{22x}^{m,e}(-\lambda_y) G_y(\lambda_y) d\lambda_y \tag{3.2.14}$$

where

$$\kappa_1 = \sqrt{k_1^2 - \lambda_y} \tag{3.2.15}$$

$$\kappa_2 = \sqrt{k_2^2 - \lambda_y}. \tag{3.2.16}$$

The contour C_y should enclose the singularities of G_y and exclude the G_x singularities. The singularities of G_y and G_x are shown in Fig. 3.5. Since G_y only has a "branch point" singularity at $\lambda_y = 0$, C_y should encircle the branch cut of G_y. The branch cut is a curve that joins the branch point and makes $\sqrt{\lambda_y}$ single valued. The presence of the branch cut sets up a rule to avoid encircling a branch point. Although we can choose the branch cut arbitrarily, it is required to have $\text{Im}(\sqrt{\lambda_y}) < 0$ (imaginary part of λ_y less than zero) to ensure that the radiation condition is satisfied. This requirement limits the argument of λ_y to the range zero to -2π in a clockwise sense. As a result of this requirement, the branch cut should be selected on the positive real axis on the complex λ_y plane as it is shown in Fig. 3.5.b.

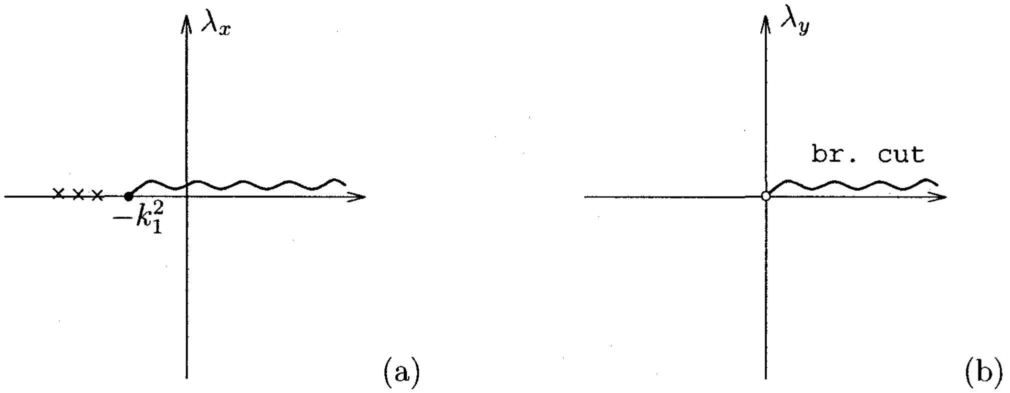

Figure 3.5: (a) Singularities of G_x on the complex λ_x plane, top Riemann sheet. The singularities include poles (×) and a branch point (•). (b) Branch point (○) singularity of G_y on the complex λ_y plane.

Fig. 3.5.a shows the poles and branch cut of G_x on the complex λ_x plane. The G_x singularities are explained in Appendix A.4. Note that the radiation condition requires that $\text{Im}(\sqrt{k_1^2 + \lambda_x}) < 0$. This limits the argument of $\sqrt{k_1^2 + \lambda_x}$ to the range

zero to -2π in a clockwise sense. This sheet is called the proper sheet or top Riemann sheet. The range -2π to -4π for $\sqrt{k_1^2+\lambda_x}$ is the improper or bottom sheet which corresponds to $\mathrm{Im}(\sqrt{k_1^2+\lambda_x}) > 0$.

Using (3.1.12), we can plot the singularities of G_x on the complex λ_y plane. The contour C_y is shown in Fig. 3.6. It is now convenient to make the change of variable $\eta = \sqrt{\lambda_y}$. This change of variable maps the top sheet of λ_y plane into the lower half of the complex η plane and makes $\sqrt{\lambda_y} = 0$ a regular point. Fig. 3.6.b shows complex η plane and the path of integration C_y. Note that this plane is referred to proper sheet because $\mathrm{Im}(\sqrt{k_1^2-\eta^2}) < 0$. Moreover, the singularities of G_x on the bottom sheet are not shown in Fig. 3.6.b. In order to map the top and bottom sheets on one plane, we use a change of variable $\eta = k_1 \sin \mathrm{w}$. This mapping transforms the two branch points at $\eta = \pm k_1$ into regular points on the w plane. Fig. 3.7 shows the complex w plane and the mapped regions. The top sheet on the η plane is mapped into the upper half of the strip $0 < \mathrm{w}_r < \pi$ and the lower half of the strip $-\pi < \mathrm{w}_r < 0$ on the w plane. The strip $-\pi < \mathrm{w}_r < \pi$ repeats in every adjacent strip of width 2π since $\sin(\mathrm{w}+2\pi) = \sin \mathrm{w}$. The path of integration C_y is also shown on the w plane. Since there are no branch points in the w plane, the integration in this plane is

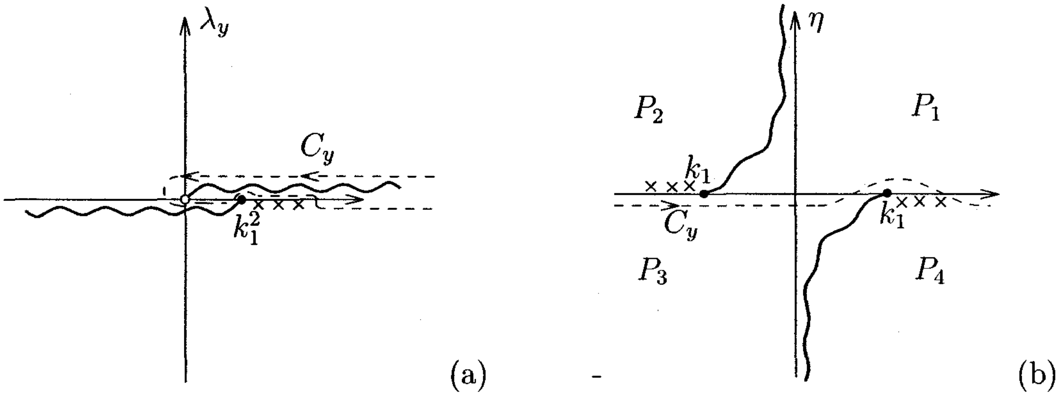

Figure 3.6: (a) Singularities on the top sheet of G_x mapped on the complex λ_y plane. G_x has poles (×) and branch point (•) singularity. G_y has a branch point (∘) at $\lambda_y = 0$. (b) The complex η plane obtained by $\eta = \sqrt{\lambda_y}$ transformation.

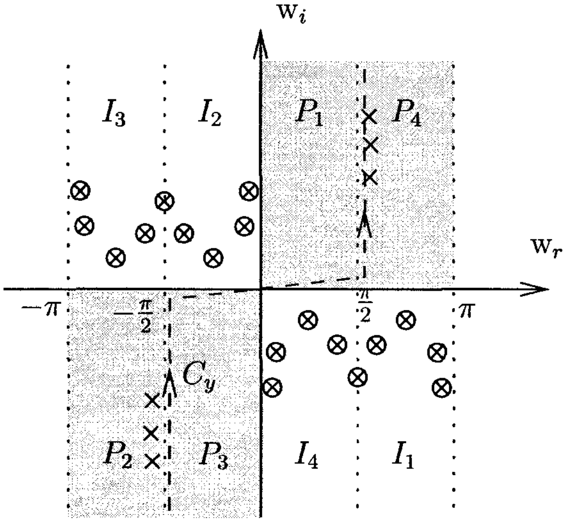

Figure 3.7: Complex w-plane shows the proper (P_{1-4}) and improper (I_{1-4}) regions which correspond to the top and bottom sheet on the η plane. The LW poles ($\otimes$) and SW poles ($\times$) are shown on this plane.

more convenient. The path of integration should have a decaying tail at the ends of contour C_y. This requires the terminations of the path to be on the proper regions as $\mathrm{w} \to \pm\infty$. Meeting this requirement, the path of integration can be deformed in any manner. However, any pole crossing during the path deformation must be accounted for according to the residue theorem.

After applying the change of variable $\eta = \sqrt{\lambda_y}$ and $\eta = k_1 \sin \mathrm{w}$, and considering the differentiation $d\eta = d\lambda_y/(2\sqrt{\lambda_y})$ and $d\eta = k_1 \cos \mathrm{w}\, d\mathrm{w}$, (3.2.14) becomes

$$G_{22}^{m,e} = \frac{1}{2\pi} \int_{C_y} \kappa_1 G_{22x}^{m,e} e^{-jk_1 \sin \mathrm{w}(y-y_s)} d\mathrm{w} \tag{3.2.17}$$

where

$$\kappa_1 = k_1 \cos \mathrm{w} \tag{3.2.18}$$

$$\kappa_2 = \sqrt{k_2^2 - k_1^2 \sin^2 \mathrm{w}}. \tag{3.2.19}$$

According to Appendix A.1, the solution to the dielectric slab problem shown in Fig. 3.3 is given by

$$G_{22} = \frac{1}{2\pi} \int_{C_y} \kappa_1 \frac{G^m_{22x} + G^e_{22x}}{2} e^{-jk_1 \sin \mathrm{w}(y-y_s)} d\mathrm{w} \tag{3.2.20}$$

for $0 \leq (x_s, x) \leq 2d$ (image theory restricts this result to $0 \leq x \leq d$, but it can be shown that G_{22} is also valid for $0 \leq x \leq 2d$). The integration on the w plane can be performed numerically. To facilitate the numerical integration, we avoid crossing the leaky wave poles. We choose the path of integration C_2 as shown in Fig. 3.8. The path of integration C_2 passes through the saddle point of G_{22} at $\mathrm{w} = \phi + j0$. Polar coordinates

$$x - x_s = R \sin \phi \tag{3.2.21}$$

$$y - y_s = R \cos \phi \tag{3.2.22}$$

are used, where $R = \sqrt{(x - x_s)^2 + (y - y_s)^2}$ is the distance between the source and the field point. When contour C_2 crosses the SW poles, the SW contribution should be accounted for in the solution. When the SW poles are crossed, the SW contribution which is the integration along the path C_3 can be obtained by the residue theorem. The expressions for the surface wave pole contributions are given in Appendix A.4. Using (A.4-11) and (3.2.20), the solution when C_2 crosses all the SW poles becomes

$$G_{22} = \frac{1}{2\pi} \int_{C_2} \kappa_1 \frac{G^m_{22x} + G^e_{22x}}{2} e^{-j\kappa_1(y-y_s)} d\mathrm{w} + G^{SW}_{\infty} \tag{3.2.23}$$

where G^{SW}_{∞} includes the SW contributions. For $\mathrm{w}_i > 0$, the contour C_2 is adjusted along the steepest descent path (SDP). Since the integrand has the fastest decaying tail along the SDP, it is more convenient to choose SDP for numerical integration when $\mathrm{w}_i > 0$. For more details on this path of integration, the reader is referred

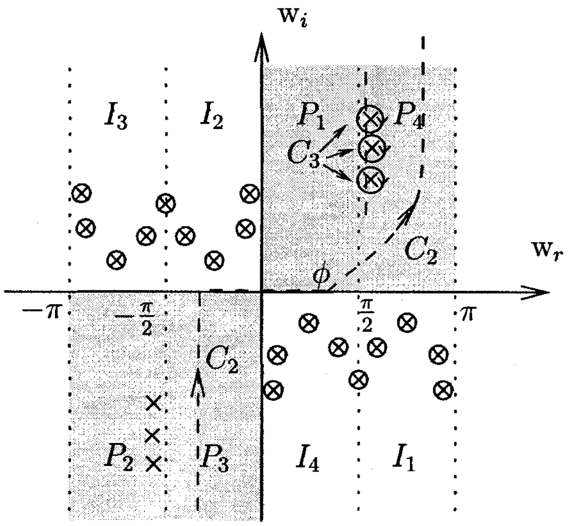

Figure 3.8: Complex w-plane shows the path of integration C_2 and C_3. Integration along P_2 and P_3 is equivalent to integration along C_y shown in Fig. 3.7. The LW poles ($\otimes$) and SW poles ($\times$) are shown on this plane.

to [2].

3.3 Electric Line Source Inside a Separable Structure

Fig. 3.9 shows a truncated dielectric slab of thickness $2d$ and height $2L$, with permittivity ϵ_2 surrounded by Regions ① and ③. The permittivity in Regions ① and ③ are denoted by ϵ_1 and ϵ_3, respectively. All the materials are assumed to be non magnetic. A current line source I_s is placed at (x_s, y_s), and the field point is at (x, y).

The structure shown in Fig. 3.9 is called separable if the structure can be solved by the separation of variables method. We need to define the separability condition, which is the criterion under which the structure becomes separable.

The construction of the Green's function is similar to the procedure explained for the infinite dielectric slab in Section 3.2. This is similar to the development obtained

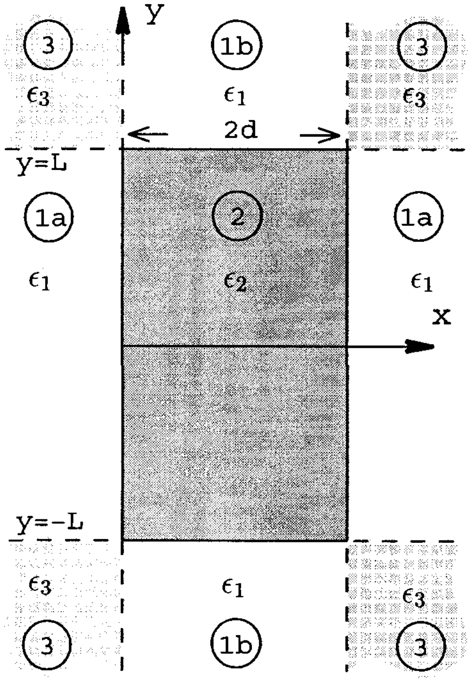

Figure 3.9: Geometry of a finite dielectric slab of thickness $2d$ and height $2L$ surrounded by Regions ① and ③. If $\epsilon_3 = 2\epsilon_1 - \epsilon_2$, the structure becomes a separable slab.

in [10]. The Green's function for the problem shown in Fig. 3.9 should satisfy the inhomogeneous Helmholtz equation

$$\nabla^2 G(x, x_s; y, y_s) + k_m^2 G(x, x_s; y, y_s) = -\delta(x - x_s)\delta(y - y_s) \qquad (3.3.1)$$

where $k_m = w\sqrt{\mu_0 \epsilon_m}$ and $m = 1, 2, 3$ depending on the field point position. To apply the separation of variables, (3.1.13) can be written as

$$k_0^2(\epsilon_x(x) + \epsilon_y(y)) = \begin{cases} k_0^2\epsilon_1 & \text{in Regions (1a) and (1b)} \\ k_0^2\epsilon_2 & \text{in Region ②} \\ k_0^2\epsilon_3 & \text{in Region ③.} \end{cases} \qquad (3.3.2)$$

We can write $\epsilon_x(x)$ and $\epsilon_y(y)$ in terms of unknown constants as

$$\epsilon_x(x) = \begin{cases} \epsilon_{x2} & 0 \le x \le 2d \\ \epsilon_{x1} & \text{elsewhere} \end{cases} \tag{3.3.3}$$

$$\epsilon_y(y) = \begin{cases} \epsilon_{y2} & -L \le y \le -L \\ \epsilon_{y1} & \text{elsewhere} \end{cases} \tag{3.3.4}$$

where the four unknowns ϵ_{x1}, ϵ_{x2}, ϵ_{y1} and ϵ_{y2} form a system of equations. Using (3.3.3) and (3.3.4) in (3.3.2), we can write

$$\epsilon_{x2} + \epsilon_{y2} = \epsilon_2 \qquad \text{in Region ②} \tag{3.3.5}$$

$$\epsilon_{x1} + \epsilon_{y2} = \epsilon_1 \qquad \text{in Region (1a)} \tag{3.3.6}$$

$$\epsilon_{x1} + \epsilon_{y1} = \epsilon_3 \qquad \text{in Region ③} \tag{3.3.7}$$

$$\epsilon_{x2} + \epsilon_{y1} = \epsilon_1 \qquad \text{in Region (1b)} \tag{3.3.8}$$

which is an overdetermined system of equations. This system of equations has no solution unless we impose

$$\epsilon_3 = 2\epsilon_1 - \epsilon_2 \tag{3.3.9}$$

so that the system of equations becomes underdetermined with an infinite number of solutions. The criterion given in (3.3.9) is the separability condition which grants a solution to (3.3.1) using the separation of variables method. Since the system of equations has an infinite number of solutions after imposing the separability condition, we can choose $\epsilon_{y2} = 0$ in order to find the other unknowns as

$$\epsilon_{x1} = \epsilon_1 \tag{3.3.10}$$

$$\epsilon_{x2} = \epsilon_2 \tag{3.3.11}$$

$$\epsilon_{y1} = \epsilon_1 - \epsilon_2. \tag{3.3.12}$$

Since the dielectric constants are obtained, we can write the 1D Helmhotz equations using (3.1.9) and (3.1.10) as

$$\frac{d^2G_x}{dx^2} + (\lambda_x + k_1^2)G_x = -\delta(x - x_s) \qquad x < 0,\, x \geq 2d \tag{3.3.13}$$

$$\frac{d^2G_x}{dx^2} + (\lambda_x + k_2^2)G_x = -\delta(x - x_s) \qquad 0 \leq x \leq 2d \tag{3.3.14}$$

$$\frac{d^2G_y}{dy^2} + (\lambda_y + k_1^2 - k_2^2)G_y = -\delta(y - y_s) \qquad y < -L,\, y \geq L \tag{3.3.15}$$

$$\frac{d^2G_y}{dy^2} + \lambda_y G_y = -\delta(y - y_s) \qquad -L \leq y \leq L. \tag{3.3.16}$$

The solution to (3.3.13) and (3.3.14) has been already obtained in terms of PEC and PMC bisected dielectric slab problems as

$$G_x = (G^e_{22x} + G^m_{22x})/2 \tag{3.3.17}$$

where G^m_{22x} and G^e_{22x} are given in (3.2.9) and (3.2.10), respectively. The solution to (3.3.15) and (3.3.16) can be written similar to (3.3.17) in terms of PEC and PMC bisected dielectric slab problems as

$$G_y = (G^e_{22y} + G^m_{22y})/2. \tag{3.3.18}$$

where G^e_{22y} and G^m_{22y} can be obtained by considering the geometry-based similarity of G_{22x} and G_{22y}. In order to adopt (3.2.9) and (3.2.10) to the 1D Green's function in the y direction, we should replace κ_1 and κ_2 with η_1 and η_2, respectively. Moreover, we should replace d, $x_>$ and $x_<$ with L, $(L - y_<)$ and $(L - y_>)$, respectively. As a result, G^e_{22y} and G^m_{22y} become

$$G^m_{22y} = \frac{j\eta_1 \sin \eta_2(L - y_>) + \eta_2 \cos \eta_2(L - y_>)}{j\eta_1 \cos \eta_2 L - \eta_2 \sin \eta_2 L} \cdot \frac{\cos \eta_2 y_<}{\eta_2} \tag{3.3.19}$$

$$G^e_{22y} = \frac{j\eta_1 \sin \eta_2(L - y_>) + \eta_2 \cos \eta_2(L - y_>)}{j\eta_1 \sin \eta_2 L + \eta_2 \cos \eta_2 L} \cdot \frac{\sin \eta_2 y_<}{\eta_2} \tag{3.3.20}$$

where η_1 and η_2 are the wavenumbers in the y direction. Using (3.2.11) and (3.2.12), and replacing κ_1, κ_2, $(\lambda_x + k_1^2)$ and $(\lambda_x + k_2^2)$ with η_1, η_2, $(\lambda_y + k_1^2 - k_2^2)$ and λ_y, the y-directed wavenumbers become

$$\eta_1 = \sqrt{\lambda_y + k_1^2 - k_2^2} \tag{3.3.21}$$

$$\eta_2 = \sqrt{\lambda_y}. \tag{3.3.22}$$

Using (3.1.19) and (3.1.12), we can write the two dimensional Green's function as

$$G_{22} = -\frac{1}{2\pi j} \oint_{C_y} G_x(-\lambda_y) G_y(\lambda_y) d\lambda_y \tag{3.3.23}$$

where G_x and G_y are given by (3.3.17) and (3.3.18). The path of integration should enclose all the singularities of G_y and exclude the singularities of G_x. The singularities of G_x on the top sheet of λ_x plane are shown in Fig. 3.10.a. It can be shown that $\kappa_2 = 0$ is a regular point in the λ_x plane. Furthermore, $\kappa_1 = 0$ is a branch point of G_x. Using (3.2.11), the branch point location can be obtained which is at $\lambda_x = -k_1^2$. In order to ensure that the radiation condition is met in the x direction, we should have $\mathrm{Im}(\kappa_1) < 0$ which defines the top sheet of λ_x plane. Similarly, $\eta_2 = 0$ is a regular point of the G_y while $\eta_1 = 0$ is a branch point in the λ_y plane. Using (3.3.21), the branch point of G_y is at $\lambda_y = k_2^2 - k_1^2$ as shown in Fig. 3.10.b. The radiation condition

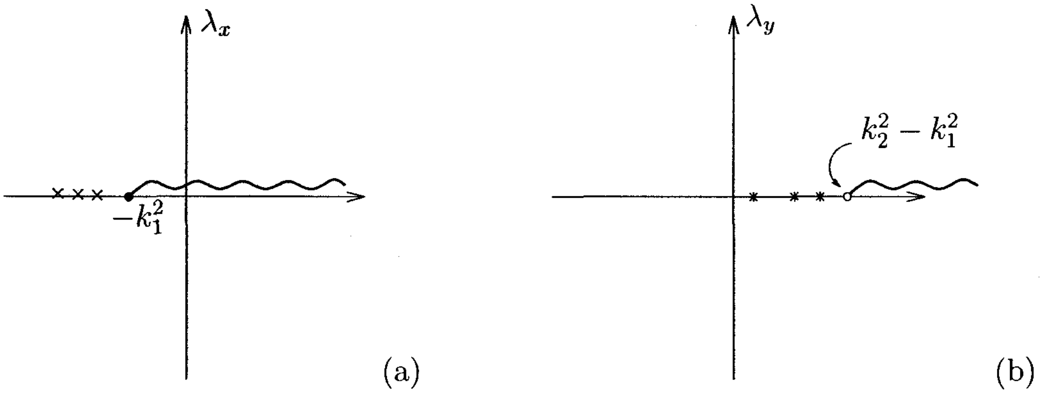

Figure 3.10: (a) Singularities of G_x in the complex λ_x plane, top Riemann sheet. The singularities include poles (×) and a branch point (•). (b) Poles ($*$) and branch point ($\circ$) of G_y in the complex λ_y plane, top Riemann sheet.

in the y direction requires $\mathrm{Im}(\eta_1) < 0$ which denotes the top sheet of λ_y plane. The singularities of G_x and G_y are similar since they are similar functions. It is noted that in order to obtain G_y, the variables κ_1, κ_2 and d of G_x were replaced by η_1, η_2 and L. We can assume $L = d$. If we compare κ_2 and η_2 which are given in (3.2.12) and (3.3.22), we notice that the position of singularities of G_x in the λ_x plane is similar to the position of singularities of G_y in the λ_y plane, but shifted k_2^2 to the right. By enlarging the slab height L, the number of G_y pole singularities increases on the top sheet of the λ_y plane. Usually $L \gg d$ indicates that G_y has a larger number of pole singularities than G_x on the top λ_y sheet. By using (3.1.12), we can map the singularities of G_x into the λ_y plane which is shown in Fig. 3.11. The path C_y encircles all the singularities of G_y in the top Riemann sheet in a counterclockwise sense. It is expedient to use the transformation $\eta_2 = \sqrt{\lambda_y}$ which maps the λ_y plane into the η_2 plane. Fig. 3.12 shows the top sheet of η_2 plane where $\mathrm{Im}(\eta_1) < 0$ and $\mathrm{Im}(\kappa_1) < 0$. Note that this transformation does not remove the branch points. The branch point at $\lambda_y = k_1^2$ is mapped to $\eta_2 = \pm k_1$ in the complex η_2 plane. To remove

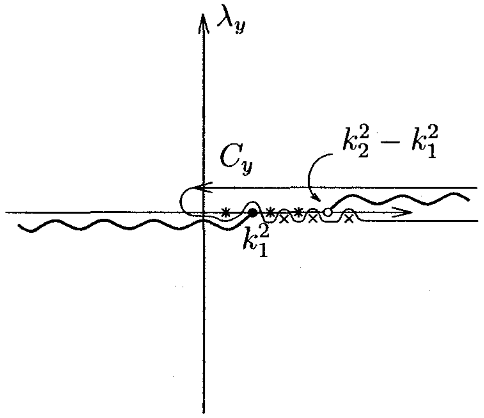

Figure 3.11: Poles ($*$) and branch point ($\circ$) of G_y accompanied by the poles ($\times$) and branch point ($\bullet$) of G_x on the complex λ_y plane. The path C_y shows the contour of integration.

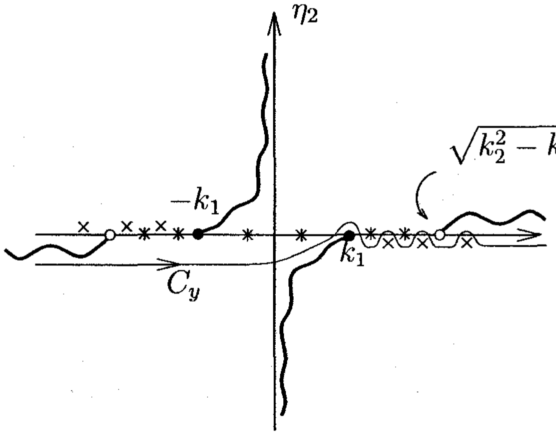

Figure 3.12: Complex η_2 plane showing the poles ($*$) and branch points ($\circ$) of G_y accompanied by the poles ($\times$) and branch points ($\bullet$) of G_x.

the branch points at $\eta_2 = \pm k_1$, we use the change of variable

$$\eta_2 = k_1 \sin \mathrm{w} \tag{3.3.24}$$

where $\mathrm{w} = \mathrm{w}_r + j\mathrm{w}_i$. This change of variable maps the η_2 plane into a two-sheeted w plane as shown in Fig. 3.13. The poles of G_x on the top and bottom sheets are

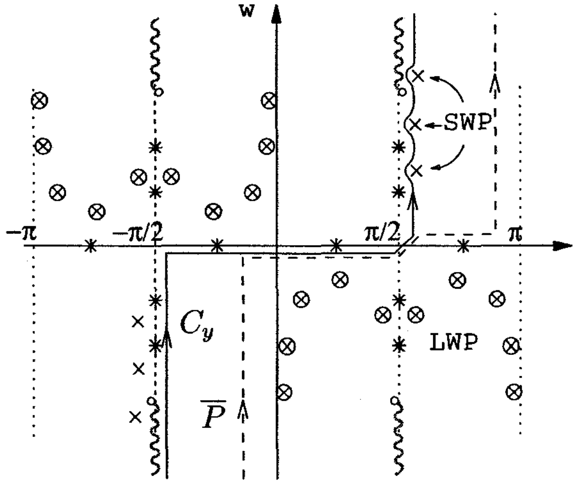

Figure 3.13: The path of integration on the complex w-plane. The singularities of G_y which are poles ($*$) and branch points ($\circ$) are shown, accompanied by the SW poles ($\times$) and the LW poles ($\otimes$) of G_x.

shown on the top sheet of the w plane. The G_x poles on the top sheet which are called surface wave (SW) poles are mapped along the line at $\mathrm{w}_r = \pm\pi/2$ for lossless dielectric material. When the dielectric is lossy, the SW poles along $\mathrm{w}_r = \pi/2$ move to the positive w_r direction in the strip $\pi/2 < \mathrm{w}_r < \pi$, $\mathrm{w}_i > 0$. The G_x poles on the bottom sheet which are called leaky wave (LW) poles are mapped into the strip $0 < \mathrm{w}_r < \pi$, $\mathrm{w}_i < 0$ and the strip $-\pi < \mathrm{w}_r < 0$, $\mathrm{w}_i > 0$. The contour of integration C_y is also shown in the w plane. The SW poles of G_x and G_y should be on the right and left side of the path C_y along $\mathrm{w}_r = \pi/2$, respectively. The LW poles of G_y are accessed by passing through the branch cuts to the bottom sheet of the w plane. The numerical integration on contour C_y for low-loss dielectric materials is complicated by the fact that the G_y poles are intertwined with the SW poles of G_x along $\mathrm{w}_r = \pi/2$.

It is convenient to deform the path C_y into the path $\overline{P}$ in order to avoid the numerical integration close to the poles. The contribution due to the SW poles should be included according to the residue theorem since the contour $\overline{P}$ crosses the

SW poles. The solution given in (3.3.23) can be written as

$$G_{22} = -\frac{1}{4\pi j}\int_{\overline{P}} \kappa_1\eta_2(G^m_{22x} + G^e_{22x})(G^m_{22y} + G^e_{22y})d\mathrm{w} + G^{SW}_{22} \tag{3.3.25}$$

where G^{SW}_{22} represents the SW contribution due to the SW poles which are crossed by the path $\overline{P}$. The 1D Green's functions G^m_{22x} and G^e_{22x} were already obtained in (3.2.9) and (3.2.10). Using (3.3.22) and (3.3.24), the wavenumbers in the x direction given in (3.2.15) and (3.2.16) become

$$\kappa_1 = k_1 \cos \mathrm{w} \tag{3.3.26}$$

$$\kappa_2 = \sqrt{k_2^2 - k_1^2 \sin^2 \mathrm{w}}. \tag{3.3.27}$$

The 1D Green's functions G^m_{22y} and G^e_{22y} are given in (3.3.19) and (3.3.20), respectively. Using (3.3.24), the wavenumbers in the y direction presented by (3.3.21) and (3.3.22) can be written as

$$\eta_1 = \sqrt{k_1^2 - k_2^2 + k_1^2 \sin^2 \mathrm{w}} \tag{3.3.28}$$

$$\eta_2 = k_1 \sin \mathrm{w}. \tag{3.3.29}$$

To obtain the contribution due to the poles, we can directly apply the residue theorem and find the residues at the SW poles. However, it is of interest to write the solution in terms of infinite slab modes which are reflected an infinite number of times by the end caps at $y = \pm L$. We can assume that an infinite slab mode is generated inside the separable structure. According to the PEC and PMC dielectric bisection, the mode can be classified as PEC or PMC mode. The expression for a mode field inside an infinite slab is given in (A.4-6), and it is repeated here for convenience. It can be rewritten as

$$G_{\infty}^{e_\nu,m_\tau} = G_x^{e_\nu,m_\tau}(x, x_s, \mathrm{w}_{\nu,\tau}) \cdot D(y - y_s) \tag{3.3.30}$$

where w_ν and w_τ represent the location of the PEC and PMC poles, respectively. The expression for $G_x^{e_\nu}$ and $G_x^{m_\tau}$ are given in (A.4-8) and (A.4-9). Inside the separable structure, the infinite slab SW mode is reflected by the end caps. Note that a SW mode of the infinite slab can be constructed as the superposition of two zig-zagging plane waves. As a result, the reflection coefficient at the boundaries $y = \pm L$ becomes

$$\Gamma = \frac{\eta_2 - \eta_1}{\eta_2 + \eta_1} \tag{3.3.31}$$

where η_1 and η_2 are the y-directed wavenumbers outside and inside the dielectric slab, respectively. It is noted that (3.3.31) is in the form of the usual transmission-line reflection coefficient. It is important to remember that when used in the 2D problem, η_1 and η_2 contain an angular dependence in terms of w. The Green's function for a SW mode generated by the source and reflected by the end cap at $y = L$ can be written by

$$\begin{aligned} G_{ref}^{e_\nu,m_\tau} &= G_x^{e_\nu,m_\tau}(x, x_s, \mathrm{w}_{\nu,\tau}) \cdot D(L - y_s) \cdot \Gamma \cdot D(L - y) \\ &= G_x^{e_\nu,m_\tau}(x, x_s, \mathrm{w}_{\nu,\tau}) \cdot \Gamma \cdot D(2L - y_s - y) \end{aligned} \tag{3.3.32}$$

where the function $D(L-y_s)$ accounts for the y direction traveling distance between the source and the top end cap. It can be written by using (A.4-7) as

$$D(L - y_s) = e^{-jk_1 \sin \mathrm{w}_{\nu,\tau} |L - y_s|}. \tag{3.3.33}$$

The traveling distance from the end cap to the field point is accounted for by the term $D(L-y)$. If we multiply (3.3.32) by $\Gamma^2 D(4L)$, we can obtain the second partial

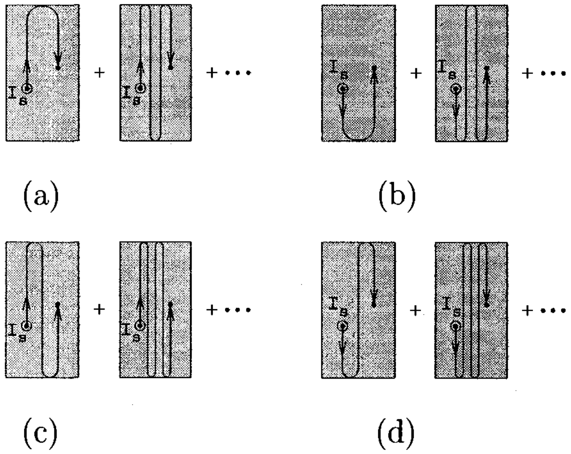

Figure 3.14: The paths having the mode contributions defined by (a) G_{r++} (b) G_{r--} (c) G_{r+-} (d) G_{r-+}.

reflection contribution. This can be explained if we let the mode continue traveling to the bottom end cap at $y = -L$, reflect back to the top end cap at $y = L$ and finally reflect back to the source. Note that this process can be repeated as it is pictured in Fig. 3.14.a, and the total contribution can be expressed as

$$G_{r++}^{e_\nu,m_\tau} = G_x^{e_\nu,m_\tau}(x, x_s, \mathrm{w}_{\nu,\tau}) \cdot \Gamma \cdot D(2L - y - y_s) \sum_{n=0}^{\infty} (\Gamma^2 D(4L))^n \tag{3.3.34}$$

where the index notation $r{+}{+}$ is adopted, whereby the first sign denotes $y = +L$ at which the first reflection happens, and the second sign being $y = +L$ at which the last reflection happens before the mode reaches the observer. The signal flow graph shown in Fig. 3.15.a depicts the multiple reflection process for the expression given in (3.3.34). The infinite series in (3.3.34) can be written in closed form since $|\Gamma^2 D(2L)| \leq 1$. By doing so, the expression in (3.3.34) becomes

$$G_{r++}^{e_\nu,m_\tau} = G_x^{e_\nu,m_\tau}(x, x_s, \mathrm{w}_{\nu,\tau}) \frac{\Gamma D(2L - y_s - y)}{1 - \Gamma^2 D(4L)}. \tag{3.3.35}$$

Fig. 3.15 shows all the possible paths that a mode can travel from the source to the

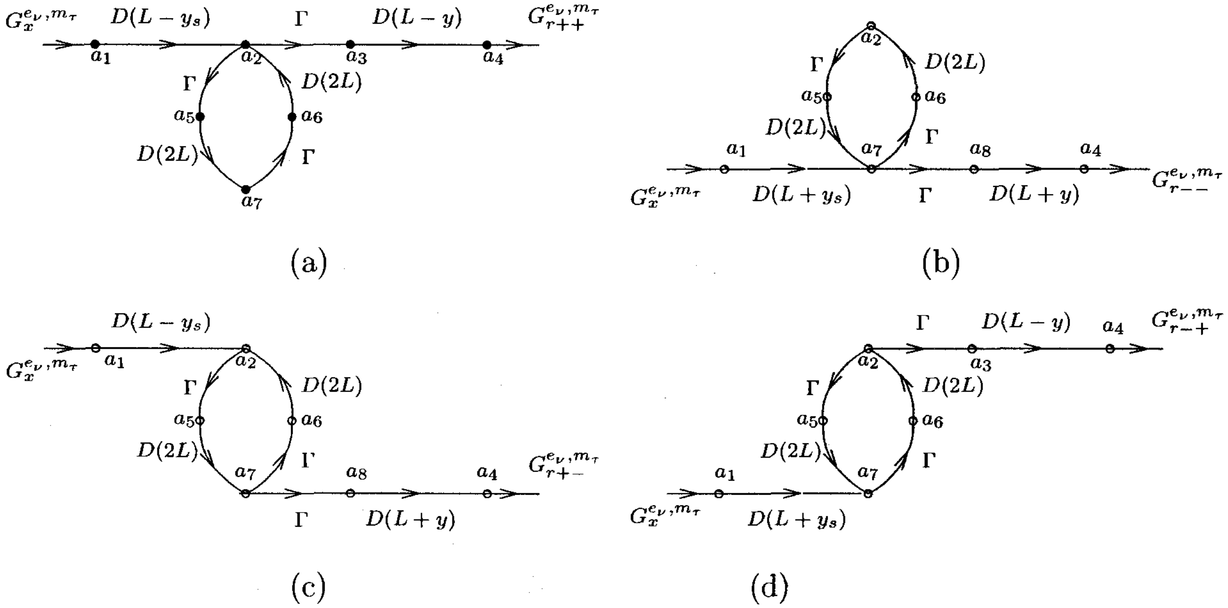

Figure 3.15: The signal flow graph for (a) G_{r++} (b) G_{r--} (c) G_{r+-} (d) G_{r-+}.

observer by having at least once reflected by an end cap. The contributions pictured in Fig. 3.14.b to Fig. 3.14.d correspond to the signal flow graphs shown in Fig. 3.15.b to Fig. 3.15.d, respectively. Using the signal flow graphs, the other contributions can be written as

$$G_{r--}^{e_\nu,m_\tau} = G_x^{e_\nu,m_\tau}(x, x_s, \mathrm{w}_{\nu,\tau}) \frac{\Gamma D(2L+y+y_s)}{1-\Gamma^2 D(4L)} \tag{3.3.36}$$

$$G_{r+-}^{e_\nu,m_\tau} = G_x^{e_\nu,m_\tau}(x, x_s, \mathrm{w}_{\nu,\tau}) \frac{\Gamma^2 D(4L+y-y_s)}{1-\Gamma^2 D(4L)} \tag{3.3.37}$$

$$G_{r-+}^{e_\nu,m_\tau} = G_x^{e_\nu,m_\tau}(x, x_s, \mathrm{w}_{\nu,\tau}) \frac{\Gamma^2 D(4L-y+y_s)}{1-\Gamma^2 D(4L)}. \tag{3.3.38}$$

It is useful to combine all the possible paths in a single signal flow graph as shown in Fig. 3.16. Note that the signal flow graph also includes the direct path from the source to the observer without any reflection by the end caps which is expressed in (3.3.30). Using the signal flow graph shown in Fig. 3.16, the total field due to a single

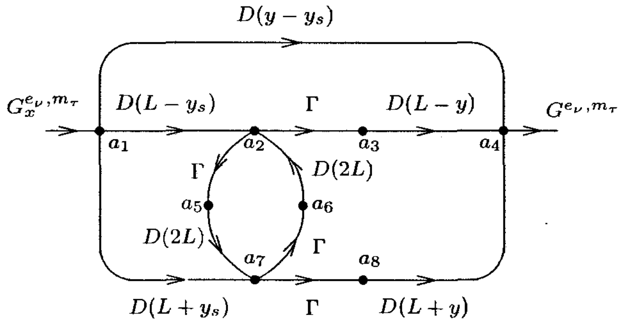

Figure 3.16: The signal flow graph showing the multiple SW reflections inside a separable structure.

mode inside a separable structure can be obtained as

$$G^{e_\nu,m_\tau} = G_\infty^{e_\nu,m_\tau} + G_{r++}^{e_\nu,m_\tau} + G_{r--}^{e_\nu,m_\tau} + G_{r+-}^{e_\nu,m_\tau} + G_{r-+}^{e_\nu,m_\tau}. \qquad (3.3.39)$$

The total SW contribution for a separable structure can be written in terms of PEC and PMC mode fields as

$$G_{22}^{SW} = \sum_\nu G^{e_\nu}/2 + \sum_\tau G^{m_\tau}/2. \qquad (3.3.40)$$

where G^{e_ν} and G^{m_τ} are the total fields due to a single mode inside a PEC and PMC bisected problems, respectively.

It is possible to obtain the SW contribution by applying the residue theorem to (3.3.25). By doing so, the result will be in form of trigonometric functions. By transforming the trigonometric functions to exponential functions, the field due to a single mode will be the same as (3.3.39). The advantage of writing the SW solution in form of (3.3.39) is that the solution is in terms of the end cap reflection coefficient. The reflection coefficient obtained for separable structure in (3.3.31) is the plane wave reflection coefficient. With this format, it is straightforward to modify the solution to treat the non-separable slab by simply changing the reflection coefficients. Then, the reflection coefficient must be found by some other means such as solving an integral equation. Removing the corner regions ($\epsilon_3 = \epsilon_1$) changes the end cap reflection coefficient for the modes. When several modes are present, each mode can generate other modes because of mode conversion at the end cap. The mode conversion can be characterized by developing an end cap scattering matrix. In the next chapter, we will use the MoM to obtain the end cap scattering matrix.

3.4 Resonance Inside a Separable Dielectric Slab

In this section, the resonance behavior of a SW mode inside a separable slab is studied. Fig. 3.17 shows an infinite slab SW mode traveling inside a separable slab. The expression for an infinite slab SW mode traveling in the y direction is given in (A.4-6). The figure shows a simple track of the SW with one reflection at each interface. The SW mode originates from the slab section A and travels in the positive y direction. After reflection at the top end cap, it travels in the negative y direction toward the bottom end cap where it reflects back again to reach section A. In order to have resonance, the fields should return in phase at section A. This requires that the SW mode that reaches section A after reflection from the top and bottom end cap have the same phase and amplitude as the originating SW mode. This condition can be written as

$$E_0(x) = E_0(x)\Gamma^2 e^{-j\eta_2 4L} \tag{3.4.1}$$

where $E_0(x)$ is the electric field of the the originated SW mode at section A, and η_2 is the y directed wavenumber given in (3.3.29). The reflection coefficient Γ at the top and bottom end cap is also given in (3.3.31). After some rearrangements in 3.4.1, the

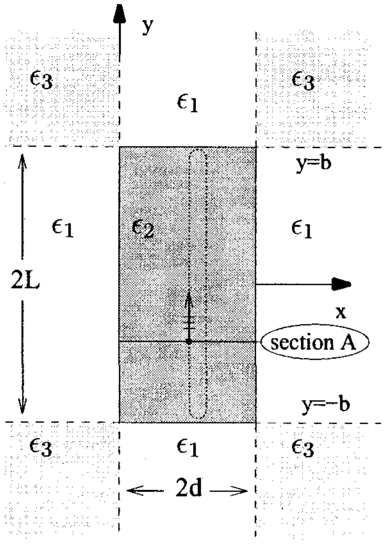

Figure 3.17: A surface wave originating from section A travels back to its origin after reflecting from the top and bottom end cap, respectively.

resonance condition becomes

$$1 - \Gamma^2 e^{-j\eta_2 4L} = 0. \qquad (3.4.2)$$

This equation also appears in the denominator of G_y. If a SW mode satisfies (3.4.2), the resonance occurs. This means that the SW pole of G_x coincides with a SW pole of G_y.

According to (3.4.2), the magnitude of the reflection coefficient should be unity in order to have resonance ($|\Gamma| = 1$). This implies that the mode is trapped inside the slab since it is fully reflected at the end caps. Furthermore, η_2 should be real which means that the slab should be lossless.

It is noted that the resonance periodically occurs as a function of L. This means that if we have a resonance height available for a mode, it is possible to find other resonance heights for the same mode. If we call the period of repeating resonance height T_{res}, we can write

$$1 - \Gamma^2 e^{-j\eta_2 2(2L+nT_{res})} = 0 \qquad n = ..., -1, 0, 1, ...; n > \frac{-2L}{T_{res}} \tag{3.4.3}$$

which gives the period of resonance height as

$$T_{res} = \pi/\eta_2. \tag{3.4.4}$$

It is noted that when the source is along $y = 0$, the period T_{res} should satisfy

$$1 - \Gamma e^{-j\eta_2(2L+nT_{res})} = 0 \qquad n = ..., -1, 0, 1, ...; n > \frac{-2L}{T_{res}}. \tag{3.4.5}$$

This is similar to placing the source inside the PMC bisected dielectric slab, when the PMC plane is at $y = 0$. The resonance period for this case becomes

$$T_{res} = 2\pi/\eta_2. \tag{3.4.6}$$

3.5 Results and Discussion

In order to validate the Green's function solution for a separable dielectric slab (GF-SS), we compare our result with the solution obtained by a commercial finite element electromagnetic solver, HFSS [42]. The solution presented in this chapter is intended for a large and thick structure, i.e. a concrete wall. Since HFSS cannot handle large structures, we have validated our result by choosing a moderately thick but not very large slab. Referring to Fig. 3.9, the dielectric slab has a height $2L = 50$ cm and thickness $2d = 20$ cm and the frequency is $f = 1.8$ GHz. The slab's relative permittivity is $\epsilon_r = 6$ and the conductivity is $\sigma_2 = 0.195$ mS/m, corresponding to concrete. The exterior medium is free space. The source strength I_0 is normalized so that it generates 1 V/m at a distance of 1 m in free space, and 0 dB corresponds to 1 V/m.

The separability condition requires $\epsilon_3 = -4\epsilon_0$ for the SS. It is noted that we do not consider σ_2 in calculating ϵ_3 since σ_2 is small. To form a 2D waveguide structure using HFSS, we placed our structure between two parallel ground planes 1 cm apart at $z = \pm 0.5$ cm. The plate spacing was sufficiently small so that only one layer of tetrahedra was generated in the z direction. We formed a 0.8 × 1.1 × 0.01 m air box embedding the structure. The four faces of the air box parallel to the z axis were defined as radiation boundaries.

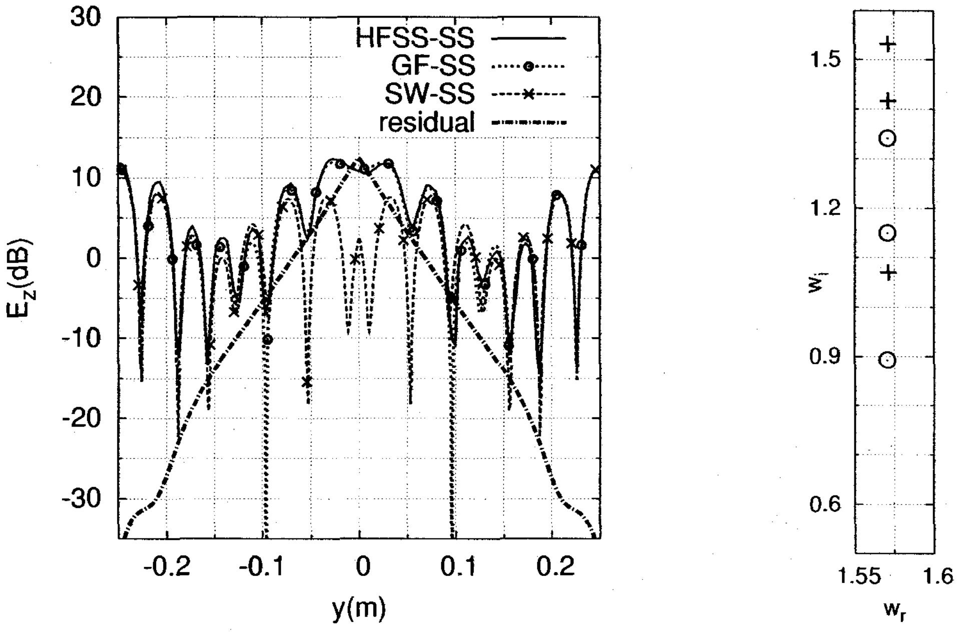

Figure 3.18: A line source at $(x_s, y_s) = (0.1, 0)$ m inside a $2L \times 2d = 0.5 \times 0.2$ m separable slab. (a) The electric field at $(x, y) = (0.04, y)$ m. (b) The locations of G_x (+) and G_y (o) poles on the w plane.

Fig. 3.18.a shows the electric field along $x = 0.04$ m, generated by a line source at $(x_s, y_s) = (0.1, 0)$ m. The result obtained by HFSS and GF-SS are compared. The final mesh in HFSS had 30337 tetrahedra. The result obtained by HFSS for

a separable dielectric slab (HFSS-SS) agrees very well with the result provided by GF-SS. This validates the GF-SS. The residual and SW part of GF-SS (SW-SS) are also shown here. The GF-SS is the total solution which consists of the residual wave plus the SW-SS. It is observed that the residual part is strong when the field point is close to the source. When the field point is away from the source, the residual part becomes weak compared to the SW part of the solution.

Fig. 3.18.b shows a part of the w plane along $w_r = \pi/2$, where the location of the G_x and G_y poles are marked. Since the source is at the center of the slab, only the PMC poles of G_x and G_y contribute. It is noted that the SW modes of G_x do not show resonance for this example since the poles of G_x and G_y are away from each other.

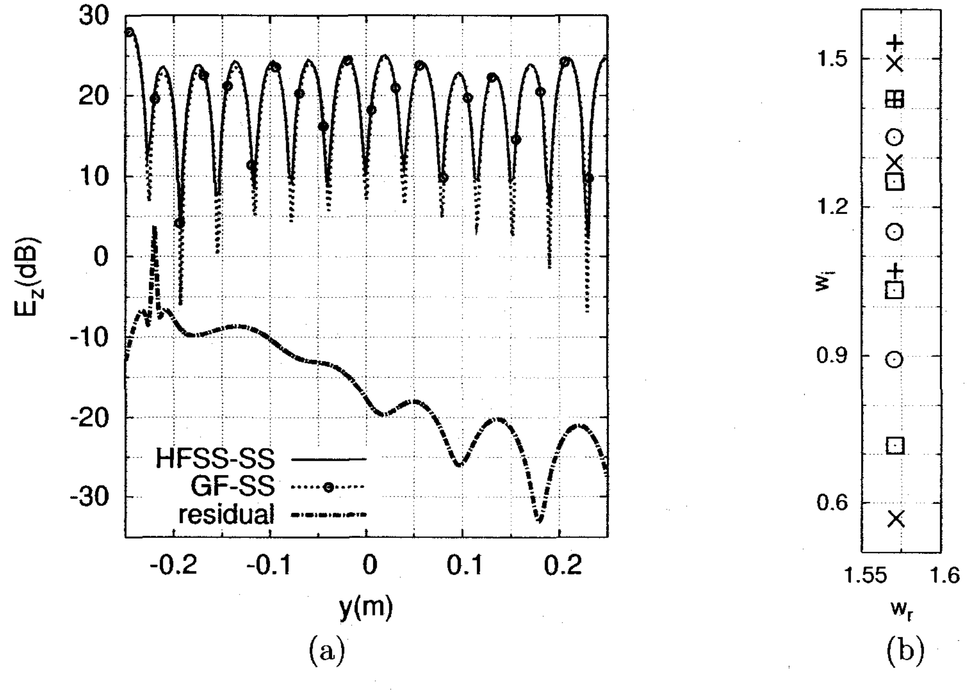

(a)

(b)

Figure 3.19: A line source at $(x_s, y_s) = (0.02, -0.22)$ m inside a $2L \times 2d = 0.5 \times 0.2$ m separable slab. (a) The electric field at $(x, y) = (0.01, y)$ m. (b) The locations of PMC (+) and PEC (×) poles of G_x and PMC (o) and PEC (□) poles of G_y on the w plane.

Fig. 3.19.a shows the electric field along $x = 0.01$ m, when the source is close

to the end cap, at $(x_s, y_s) = (0.02, -0.22)$ m. The result obtained by HFSS-SS and GF-SS agree very well. For this case, it is shown that the residual part of the solution does not make a significant contribution to the total field. The locations of the G_x and G_y poles are also shown in Fig. 3.19.b. It is noted that the PEC poles of G_x and G_y contribute in this case. It can be observed that one of the SW modes is very close to resonance since its corresponding G_x pole at $w = 1.5710 + j1.4166$ is very close to a G_y pole at $w = 1.5708 + j1.4189$.

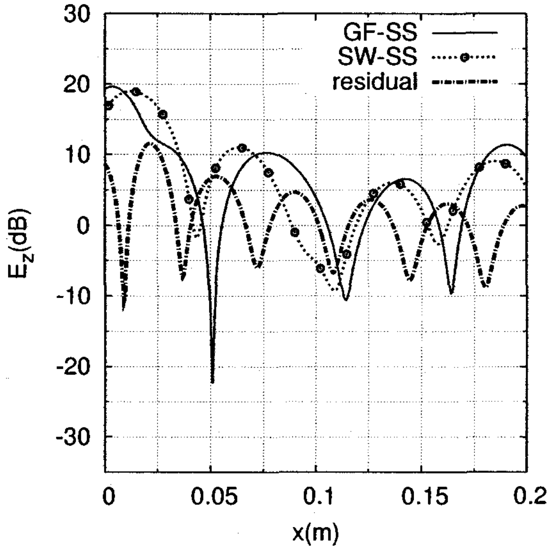

Figure 3.20: The electric field along the width of the slab. The source is at $(x_s, y_s) = (0.02, -0.22)$ m, and the field point is along $y = -0.23$ m.

The electric field at $(x, y) = (x, -0.23)$ m along the width of slab is also shown in Fig. 3.20. For this case, the residual part of the solution is comparable to the SW field, and it makes a significant contribution to the total field.

The examples of Fig. 3.18-3.20 serve to illustrate that the relative strengths of the SW and residual contributions depends on the locations of the source and field points in the slab. It is possible to find a slab height $2L$ that causes a SW pole of G_x to become very close to a G_y pole. Fig. 3.21 shows the electric field inside the

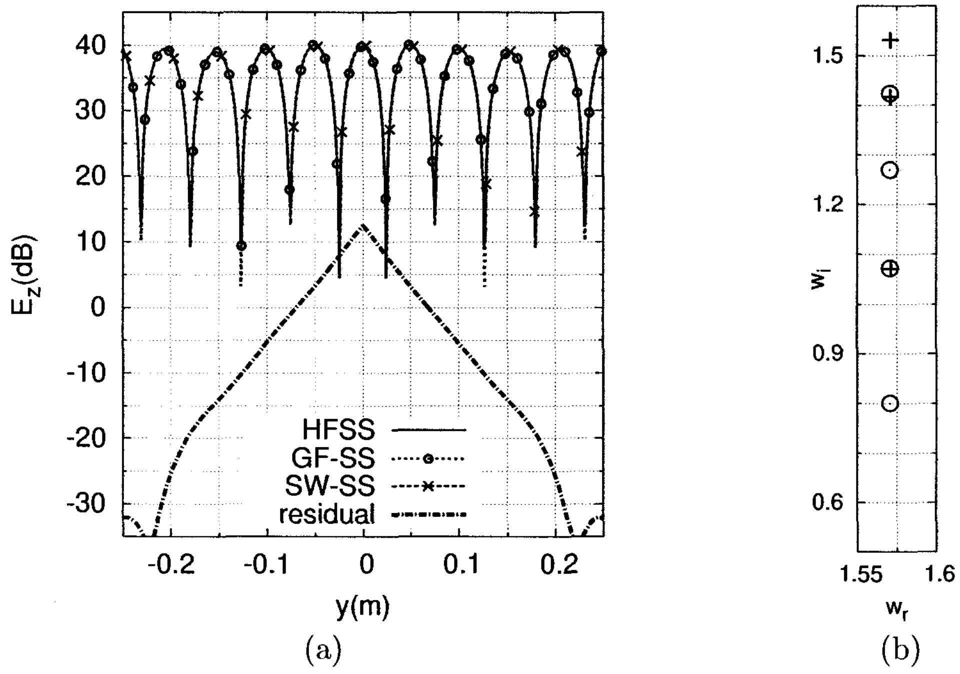

(a) (b)

Figure 3.21: A line source at $(x_s, y_s) = (0.1, 0)$ m inside a $2L \times 2d = 0.535 \times 0.2$ m separable slab. (a) The electric field at $(x, y) = (0.04, y)$ m. (b) The locations of G_x (+) and G_y (o) poles on the w plane.

dielectric slab with height $2L = 0.535$ m. The source is at $(x_s, y_s) = (0.1, 0)$, and field point is at $(x, y) = (0.04, y)$ m. It also shows the location of the poles in the w plane where a PMC pole of G_x at $w = 1.571207 + j1.070810$ is very close to a PMC pole of G_y at $w = 1.570811 + j1.071560$. As a result of the G_x-G_y pole overlap, the corresponding SW mode shows a close to resonance behavior. For this slab height, another PMC pole of G_x at $w = 1.571019 + j1.416632$ is also close to a PMC pole of G_y at $w = 1.570839 + j1.424187$. This explains why the SW field is so strong compared to the residual wave part.

The exact locations of the G_x poles on the w plane are given in Table 3.1. For each mode incident on the end caps, an incidence angle is calculated as

$$\theta_i = \arccos \frac{\eta_2}{k_2} \qquad 0 \leq \theta_i \leq \pi/2. \tag{3.5.1}$$

Table 3.1: Locations of the PMC poles of G_x on the w plane.

τ	w_τ	θ_i(degree)
1	$1.570978 + j1.531669$	8.7
2	$1.571019 + j1.416632$	27.0
3	$1.571207 + j1.070810$	48.3

Note that each SW mode can be written as a superposition of plane waves. The incident angle θ_i is measured from the positive y axis to the direction of plane wave travel regardless of sign. For calculating the incident angle shown in Table 3.1, the material loss is neglected so that θ_i becomes a real number. Since the critical angle for the material chosen here is $\theta_c \simeq 24.1°$, the mode corresponding to $\tau = 1$ is transmitted at the end caps while the other modes are totally reflected.

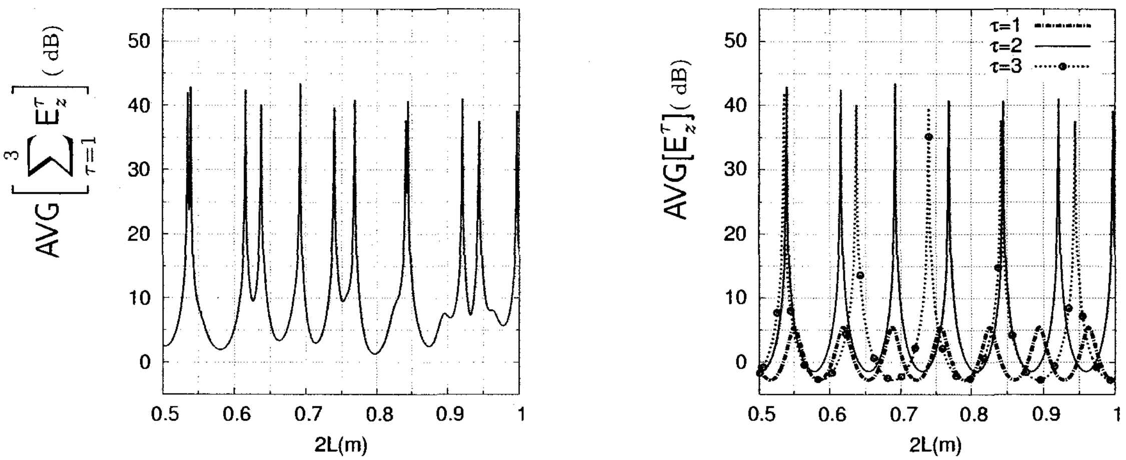

(a) (b)

Figure 3.22: (a) The average of the total SW field for PMC modes calculated along the line $(x, y) = (0.04, -L < y < L)$ m inside a SS. (b) The average of the PMC mode fields calculated along the line $(x, y) = (0.04, -L < y < L)$ m inside a SS.

It is useful to study the field variation of each SW mode with respect to the slab height. Fig. 3.22.a shows the average of the total SW field calculated along the line $(x, y) = (0.04, -L < y < L)$ m when the source was at $(x_s, y_s) = (0.1, 0)$ m. At the heights where the electric field is maximum, one of the SW modes is close to resonance. The electric field contribution of the τ'th PMC mode is denoted by E_z^τ.

Fig. 3.22.b shows the average of each SW mode field along $(x, y) = (0.04, -L < y < L)$ m. It is observed that the mode corresponding to $\tau = 1$ does not show any resonance behavior since this SW mode is not totally reflected at the end caps. Furthermore, it was observed that the pole corresponding to $\tau = 1$ never becomes close to any G_y pole. By increasing the slab height, the G_y poles on the top sheet of the w plane, which originate from the branch point at $w = 1.5710 + \jmath 1.4436$, move downward. As a result, the G_y poles cannot overlap the G_x pole at $\mathrm{w}_{\tau=1}$. Using (3.4.6), the resonance period $T_{res} = 0.0763$ m is calculated for the second PMC mode ($\tau = 2$) which also agrees with the period of the maxima shown in Fig. 3.22.b. Similarly, the calculated period of resonance $T_{res} = 0.10216$ m for the third PMC mode ($\tau = 3$) matches the period of resonance shown in Fig. 3.22.

In summary, it has been shown that when a G_x and G_y pole overlap, it corresponds to the resonance of a SW mode inside the slab. It was shown that the SS Green's function and HFSS solution are in good agreement, whether or not we are near a resonant frequency.

Chapter 4

Interior Green's Function Solution for a Thick and Finite Dielectric Slab

In this chapter, we study the mode conversion inside a thick semi-infinite dielectric slab. The mode conversion occurs because of the diffraction phenomenon at the edges of the semi-infinite slab. The mode conversion can be characterized by the use of a scattering matrix. The MoM can be applied in order to obtain the scattering matrix. The integral equation is formed by enforcing the continuity of the tangential electric field on an infinite plane at the end cap of a semi-infinite dielectric slab. The infinite plane contains the truncation interface and is perpendicular to the slab extent. Having the scattering matrix, we will modify the separable slab solution in this chapter to obtain the interior Green's function solution for a thick and finite dielectric slab. This work has been reported in [27].

4.1 End Cap Scattering Matrix

Fig. 4.1 shows a semi-infinite dielectric slab of thickness $2d$. The slab is truncated at $y = L$, and it occupies the region between $x = 0$ and $x = 2d$. We assume that the dielectric slab is thick enough to let several guided modes propagate inside the slab. The guided modes are generated by a line source at (x_s, y_s). The modes traveling toward the positive y direction are diffracted at the truncated interface, and mode conversion is expected. In order to express the interactions between the guided modes, we can use a scattering matrix. The scattering matrix $\boldsymbol{S}_{11}$, which is a square matrix, characterizes the interactions between the incident and reflected modes at the truncation interface. An element of the scattering matrix $S_{11}(i,j)$ is the amplitude of the i'th reflected mode due to the j'th incident mode of unit amplitude. The notation in [43] is followed, whereby the subscript 11 indicates that this is a reflection term.

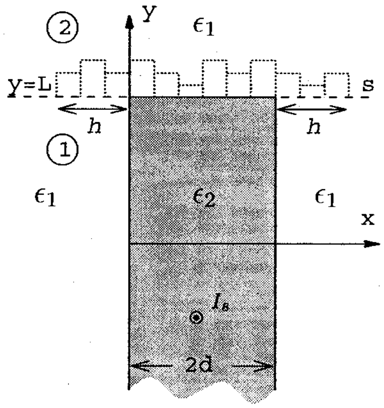

Figure 4.1: Semi-infinite dielectric slab of thickness $2d$. The infinite plane S at $y = L$ separates the structure into Regions ① and ②.

We classify the guided modes into PEC and PMC modes which are the modes inside a PEC and PMC bisected dielectric slab, respectively. Since the PEC and PMC modes originate from two independent structures, the PEC modes cannot be converted to the PMC modes and vice versa. As a result, we can express the scattering matrix by

$$S_{11} = \begin{bmatrix} S_{11}^m & 0 \\ 0 & S_{11}^e \end{bmatrix} \tag{4.1.1}$$

where S_{11}^m and S_{11}^e are the scattering matrices for the PMC and PEC modes, respectively. In order to obtain the elements of the scattering matrices, the MoM is applied. The details are presented in the next section.

4.2 MoM Formulation

The semi-infinite slab of thickness $2d$ is shown in Fig. 4.1 with permittivity ϵ_2 surrounded by a material having a permittivity of ϵ_1. The permeability in both materials is assumed to be μ_0, the free space permeability. A line source of strength I_s at (x_s, y_s) inside the slab generates the guided modes. The modes traveling toward the positive y direction are reflected back by the end cap at $y = L$. To solve this problem, we form the integral equation formulations on an infinite plane S at $y = L$. This is similar to the spectral domain approach applied by Maci *et al.* [7] and Volski and Vandenbosch [8] to obtain the diffraction coefficient of a semi-infinite dielectric slab. However, the formulations here are formed in the spatial domain unlike [7] and [8] in which the spectral domain formulation was used. Since we are interested in the mode reflection and conversions at the end cap, the MoM region on the infinite plane S can be limited to the range $-h < x < 2d + h$. This is possible since the MoM currents on the plane S outside this range turn out to be weak. This is because the electric field outside the slab generated by a guided mode decays exponentially when the field point moves away from the slab surface. By reciprocity, if a source outside the slab moves away from the surface, the generated SW mode field will be weak.

Applying the surface equivalence principle on the plane S, the problem is separated into two independent regions, Region ① and Region ②. Regions ① and ② occupy

$y < L$ and $y > L$, respectively. By placing a PMC plate at $y = L^+$ and using image theory, Region ① becomes an infinite dielectric slab. The equivalent electric current $J_{eq}^{(1)}$ on the plane S in Region ① is doubled while the equivalent magnetic current is shorted by removing the PMC plate and applying the image theorem. The total electric field in Region ① generated by a line source can be written as

$$E_1 = E_1^{inc} + E_1^{img} + E_1^s \tag{4.2.1}$$

where E_1^{inc} and E_1^{img} are the electric fields initiated by the line source and its image in front of an infinite dielectric slab, respectively; E_1^s is the scattered electric field generated by the duplicated equivalent electric current $2J_{eq}^{(1)}$ in the presence of the infinite dielectric slab. Similarly, placing a PMC sheet at $y = L^-$ and using image theory doubles the equivalent electric current $J_{eq}^{(2)}$ and shorts the equivalent magnetic current in Region ②. After applying image theory to the PMC sheet, Region ② becomes free space in which the doubled equivalent electric current is radiating. Since we assumed that the line source is in Region ①, the total electric field in Region ② becomes

$$E_2 = E_2^s \tag{4.2.2}$$

where E_2^s is the scattered electric field in Region ② generated by the doubled equivalent electric current $2J_{eq}^{(2)}$ radiating in the free space. To write the integral equations, we impose the continuity of the electric and magnetic fields on the plane S. Imposing the continuity of the magnetic field on the plane S requires

$$J_{eq}^{(1)}(x) = -J_{eq}^{(2)}(x) = J_{eq}(x) \tag{4.2.3}$$

where the unknown current density $J_{eq}(x)$ can be obtained by solving the integral equation

$$E_1^{inc}(x) + E_1^{img}(x) + E_1^s(x) = E_2^s(x) \qquad \text{on plane S} \tag{4.2.4}$$

which provides the continuity of the electric field on the plane S. Since $E_1^{inc}(x)$ and $E_1^{img}(x)$ are equal due to the symmetry of the source and its image about the plane S, we can express (4.2.4) by using (4.2.3) as

$$\begin{aligned} 2E_1^{inc}(x) - 2jw\mu_o \int_S J_{eq}(x')G_\infty(\boldsymbol{\rho}, \boldsymbol{\rho}')dx' \\ = w\mu_o/2 \int_S J_{eq}(x')H_0^{(2)}(k_1|x - x'|)dx' \end{aligned} \tag{4.2.5}$$

where G_∞ is the Green's function of the infinite extent dielectric slab shown in Fig. 4.2 and $\boldsymbol{\rho} = \hat{\boldsymbol{x}}x + \hat{\boldsymbol{y}}L$. The expression for G_∞ when the source and field point are inside the slab is given in (3.2.23). The variable of integration on the plane S is defined by $\boldsymbol{\rho}' = \hat{\boldsymbol{x}}x' + \hat{\boldsymbol{y}}L$. To apply the MoM, we represent the unknown equivalent current along $y = L$ by

$$J_{eq}(x) = \begin{cases} \sum_{n=1}^{N} I_n P_n(x) & -h < x \leq 2d + h \\ 0 & \text{elsewhere} \end{cases} \tag{4.2.6}$$

where the I_n denotes the unknown coefficient associated with the n'th cell. The parameter h defines the extent of the MoM region which is $-h \leq x \leq 2d + h$. It is noted that the MoM region is divided into N cells. The pulse basis function P_n is expressed as

$$P_n = \begin{cases} 1 & x_n - \frac{\delta}{2} < x \leq x_n + \frac{\delta}{2} \\ 0 & \text{otherwise.} \end{cases} \tag{4.2.7}$$

where δ is the cell size and x_n represents the center of the n'th cell located at $\boldsymbol{\rho}_n = \hat{\boldsymbol{x}}x_n + \hat{\boldsymbol{y}}L$. The cell size should comply with $\delta \leq 0.1\lambda_{1,2}$ where λ_2 and λ_1 represent the wavelength inside and outside the dielectric slab, respectively. This criterion gives two different cell sizes inside and outside the slab, so the small value $\delta = 0.1\lambda_2$ is used. In forming the system of equations, the delta testing function is used. The $N \times N$ system of equations can be written as

$$E^{inc}_{sw_j}(\boldsymbol{\rho}_m) = \sum_{n=1}^{N} Z_{mn} I_n \qquad m = 1, 2, \ldots N \tag{4.2.8}$$

where $\boldsymbol{\rho}_m$ represents the center of the m'th cell on the MoM region located at $\boldsymbol{\rho}_m = \hat{\boldsymbol{x}}x_m + \hat{\boldsymbol{y}}L$. The incident field denoted by $E^{inc}_{sw_j}$ is the field due to the j'th incident SW mode. The elements of the impedance matrix Z_{mn} can be written by using (4.2.5)-(4.2.8) as

$$\begin{aligned} Z_{mn} =& j\omega\mu_0 \int_{x_n-\delta/2}^{x_n+\delta/2} G_\infty(\boldsymbol{\rho}_m, \boldsymbol{\rho}')dx' \\ &+\omega\mu_0/4 \int_{x_n-\delta/2}^{x_n+\delta/2} H_0^{(2)}(k_1|x_m - x'|)dx'. \end{aligned} \tag{4.2.9}$$

It is noted that the geometrical symmetry of the slab with respect to the $x = d$ can be used to speed up calculating the elements of the impedance matrix. For calculating the self impedance term, we should extract the free space Green's function G_f from

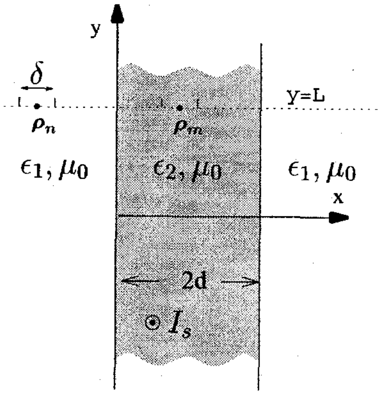

Figure 4.2: An infinite extent dielectric slab.

G_∞. For the case when the source and the field point are inside the slab, we can write

$$G_\infty = G_f + G_m^{(2)} \tag{4.2.10}$$

where G_f and $G_m^{(2)}$ are given in (A.8-3) and (A.8-7), respectively. The self term evaluation of the free space Green's function which contains the singular term is given in (A.8-4). When the source and the field point are outside the slab, the Green's function can be evaluated similarly.

The line source at $\boldsymbol{\rho}_s = \hat{\boldsymbol{x}} x_s + \hat{\boldsymbol{y}} y_s$ will excite PMC and PEC SW modes. For the moment, let us consider the j'th incident PEC mode at the aperture as

$$E_{\mathrm{sw}_j}^{inc}(x_n) = \zeta_j^{inc} \boldsymbol{e}_j^{inc}(x_n) = -j\omega\mu_0 I_s G_\infty^{e_j}(\boldsymbol{\rho}_n, \boldsymbol{\rho}_s) \tag{4.2.11}$$

where ζ_j^{inc} is the amplitude of the j'th incident PEC mode at $y = L$, and $G_\infty^{e_j}$ is given in (A.4-6). The SW mode function which is denoted by $\boldsymbol{e}_j^{inc}$ is normalized so that it has a unit amplitude at its maximum. The solution to the $N \times N$ system of equations in (4.2.8) can then be obtained. After obtaining the I_n coefficients, the i'th scattered PEC mode due to the j'th incident PEC mode at $y = L$ can be expressed as

$$E_{\mathrm{sw}_{ij}}^{s}(x) = \zeta_{ij}^{s} \boldsymbol{e}_i^{s}(x) = -j\omega\mu_0 \sum_{n=1}^{N} I_n \int_{x_n-\delta/2}^{x_n+\delta/2} G_\infty^{e_i}(\boldsymbol{\rho}, \boldsymbol{\rho}')dx' \tag{4.2.12}$$

where ζ_{ij}^{s} denotes the amplitude of the i'th scattered PEC mode at $y = L$ due to the j'th incident PEC mode. Since the image of the j'th incident PEC mode in the PMC plane contributes only to the j'th reflected PEC mode, the amplitude of the

i'th reflected PEC mode at $y = L$ can be expressed by

$$\zeta_{ij}^{ref} = \begin{cases} \zeta_{jj}^{s} + \zeta_{j}^{img} & i = j \\ \zeta_{ij}^{s} & i \neq j \end{cases} \tag{4.2.13}$$

which is due to the j'th incident PEC mode. It is noted that ζ_j^{img}, which is the amplitude of the image of the j'th incident PEC mode, is equal to ζ_j^{inc} on the plane S. The elements of the scattering matrix $\boldsymbol{S}_{11}^e$ can be obtained by

$$S_{11}^e(i,j) = \frac{\zeta_{ij}^{ref}}{\zeta_j^{inc}} \tag{4.2.14}$$

where $S_{11}^e(i,j)$ is already defined as the amplitude of the i'th reflected PEC mode due to the j'th incident mode of unit amplitude.

Similarly, the elements of the scattering matrix $\boldsymbol{S}_{11}^m$ can be obtained if we replace G_∞^e by G_∞^m in (4.2.11) and (4.2.12) where $G_\infty^{m_i}$ is given in (A.4-6). The elements of $\boldsymbol{S}_{11}^m$ then become

$$S_{11}^m(i,j) = \frac{\zeta_{ij}^{ref}}{\zeta_j^{inc}}. \tag{4.2.15}$$

Having $\boldsymbol{S}_{11}^e$ and $\boldsymbol{S}_{11}^m$, we can form the end cap scattering matrix by using (4.1.1). It is noted that the scattering matrix characterizes the SW mode reflection and mode conversion at the end cap. However, it does not include the near field contribution due to the pulse basis currents at the end cap.

4.3 SW Solution for a Semi-Infinite Dielectric Slab

The SW solution inside a semi-infinite dielectric slab is obtained by modifying the SW solution of the separable semi-infinite dielectric slab (S-SIS). Fig. 4.3 shows the

S-SIS where the end cap interface is at $y = L$. The SW solution can be written as

$$G^{SW}_{S-SIS} = \sum_{\nu} G^{e_\nu}/2 + \sum_{\tau} G^{m_\tau}/2. \tag{4.3.1}$$

where G^{e_ν} and G^{m_ν} denote the total field due to a single PEC and PMC mode,

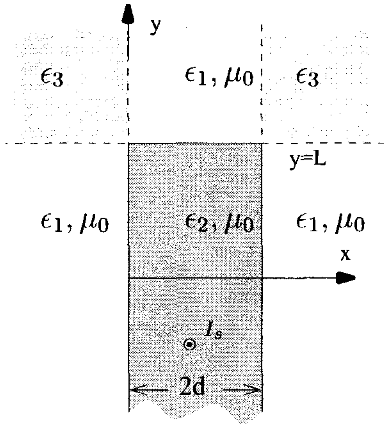

Figure 4.3: Separable semi-infinite dielectric slab of thickness $2d$. The separability condition requires $\epsilon_3 = 2\epsilon_1 - \epsilon_2$.

respectively. Furthermore, each mode which is composed of the infinite slab mode plus the reflected mode at the end cap can be written as

$$G^{e_\nu, m_\tau} = G^{e_\nu, m_\tau}_{\infty} + G^{e_\nu, m_\tau}_{ref} \tag{4.3.2}$$

where $G^{e_\nu, m_\tau}_{\infty}$ and G^{e_ν, m_τ}_{ref} are given in (3.3.30) and (3.3.32), respectively. It is useful to write (4.3.2) in matrix form as

$$\boldsymbol{G}^{e,m}_{S-SIS} = \boldsymbol{D}^{e,m}(y - y_s)\boldsymbol{G}^{e,m}_{x} + \boldsymbol{D}^{e,m}(L - y)\boldsymbol{\Gamma}^{e,m}\boldsymbol{D}^{e,m}(L - y_s)\boldsymbol{G}^{e,m}_{x} \tag{4.3.3}$$

where the diagonal reflection coefficient matrices $\boldsymbol{\Gamma}^{e,m}$ have elements given by

$$\Gamma_{ij}^{e,m} = \begin{cases} \frac{\eta_2-\eta_1}{\eta_2+\eta_1} & i = j \\ 0 & i \neq j. \end{cases} \tag{4.3.4}$$

The elements of the column vector $\boldsymbol{G}_x^{e,m}$ are denoted as $G_x^{e_i,m_i}$ which are given in (A.4-8) and (A.4-9). Furthermore, the elements of the column matrix $\boldsymbol{G}_\infty^{e,m}$ are $G_\infty^{e_\nu,m_\tau}$ given in (3.3.30). The diagonal matrix $\boldsymbol{D}^{e,m}$ has elements given by

$$D_{ij}^{e,m}(y) = \begin{cases} e^{-jk_1 \sin \mathrm{w}_i |y|} & i = j \\ 0 & i \neq j. \end{cases} \tag{4.3.5}$$

where $D_{ii}^{e,m}(L - y_s)$ accounts for the y direction traveling of a mode from the source to the end cap. Similarly, $D_{ii}^{e,m}(L-y)$ accounts for the y direction traveling of a mode from the end cap to the field point.

We now wish to solve the semi-infinite dielectric slab (SIS) problem shown in Fig. 4.1. To modify the S-SIS solution for a semi-infinite slab, the mode conversion is a possibility that we must consider. We can correct the SW solution provided that the scattering matrix at the end cap $\boldsymbol{S}_{11}$ is available. This can be done by replacing $\boldsymbol{\Gamma}^{e,m}$ by $\boldsymbol{S}_{11}^{e,m}$ in (4.3.3). As a result, we can have

$$\boldsymbol{\zeta}_{SIS}^{e,m} = \boldsymbol{D}^{e,m}(y - y_s)\boldsymbol{\zeta}_x^{e,m} + \boldsymbol{D}^{e,m}(L - y)\boldsymbol{S}_{11}^{e,m}\boldsymbol{D}^{e,m}(L - y_s)\boldsymbol{\zeta}_x^{e,m}. \tag{4.3.6}$$

The elements of the column vector $\boldsymbol{\zeta}_x^{e,m}$ are the amplitudes of the PEC or PMC modes $\zeta_{\nu,\tau}^x$ defined as

$$G_x^{e_\nu,m_\tau} = \zeta_{\nu,\tau}^x e_{\nu,\tau}(x) \tag{4.3.7}$$

where $\boldsymbol{e}_\nu$ and $\boldsymbol{e}_\tau$ are the normalized PEC and PMC mode functions, respectively.

The obtained column vector $\zeta_{SIS}^{e,m}$ represents the amplitudes of the mode functions, $\zeta_{SIS}^{\nu,\tau}$, given as

$$G^{e_\nu,m_\tau} = \zeta_{SIS}^{\nu,\tau}\mathbf{e}_{\nu,\tau}(x). \tag{4.3.8}$$

The SW solution for the SIS becomes

$$G_{SIS}^{SW} = \sum_{\nu} G^{e_\nu}/2 + \sum_{\tau} G^{m_\tau}/2. \tag{4.3.9}$$

It is possible to replace the scattering matrices $\boldsymbol{S}_{11}^{e,m}$ in (4.3.6) with the equivalent diagonal scattering matrices $\boldsymbol{\Lambda}^{e,m}$ which have only the diagonal elements $\Lambda_{ii}^{e,m}$ given as

$$\Lambda_{ii}^{e,m} = \sum_{j} S_{11}^{e,m}(i,j)\frac{D_{jj}^{e,m}(L-y_s)\zeta_j^x}{D_{ii}^{e,m}(L-y_s)\zeta_i^x}. \tag{4.3.10}$$

It is noted that $\boldsymbol{\Lambda}^{e,m}$ and $\boldsymbol{\Gamma}^{e,m}$ are diagonal matrices representing mode reflections at the end cap of a SIS and S-SIS, respectively. By forming the equivalent scattering matrices $\boldsymbol{\Lambda}^{e,m}$, it is possible to compare $\boldsymbol{\Lambda}^{e,m}$ with the reflection coefficient matrices $\boldsymbol{\Gamma}^{e,m}$. The results and discussion will be given in Section 4.5.

4.4 Finite Dielectric Slab Solution Using the GSM Method

Fig. 4.4 shows a finite dielectric slab of height $2L$ and thickness $2d$ with the permittivity ϵ_2 and permeability μ_0, surrounded by a material characterized with ϵ_1 and μ_0. The dielectric slab occupies the region between $x = 0$ and $x = 2d$ along the x direction, and $y = -L$ and $y = L$ in the y direction. The problem is similar to the separable structure shown in Fig. 3.9 but having $\epsilon_3 = \epsilon_1$. For this problem the mode conversion is a possibility that we must consider. We can modify the SW part of

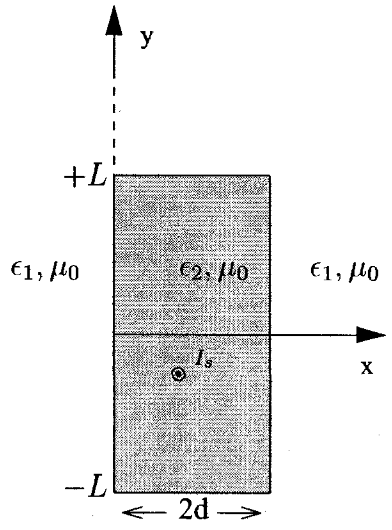

Figure 4.4: A finite dielectric slab of length $2L$ and thickness $2d$.

the solution provided that the end cap scattering matrix $\boldsymbol{S}_{11}$ is available. We can generalize the results of Section 3.3 by replacing Γ with $\boldsymbol{S}_{11}$ which is a matrix. This is referred to as the generalized scattering matrix (GSM) method. The GSM method accounts for all the mode reflections and conversions inside the finite slab. It is convenient to employ the signal flow graph shown in Fig. 3.16 by converting the branch parameters into matrices. (In doing so, the reflection coefficient Γ is replaced by the end cap scattering matrix $\boldsymbol{S}_{11}$.) The new signal flow graph is shown in Fig. 4.5. It represents all the mode interactions inside the dielectric slab whereby the problem is treated separately for the PEC and PMC modes. As a result, the input column vector $\boldsymbol{\zeta}_x^{e,m}$ has the elements $\zeta_{\nu,\tau}^x$ which are the amplitudes of the PEC or PMC modes given in (4.3.7). It is noted that $G_x^{e_\nu,m_\tau}$ given by (A.4-8) and (A.4-9) can be written in form of (4.3.7). The diagonal matrix $\boldsymbol{D}^{e,m}(y-y_s)$ accounts for the y direction traveling of a mode from the source to the field point where the elements of the diagonal matrix $\boldsymbol{D}^{e,m}(y)$ are already defined in (4.3.5). Using the signal flow graph, we can write the

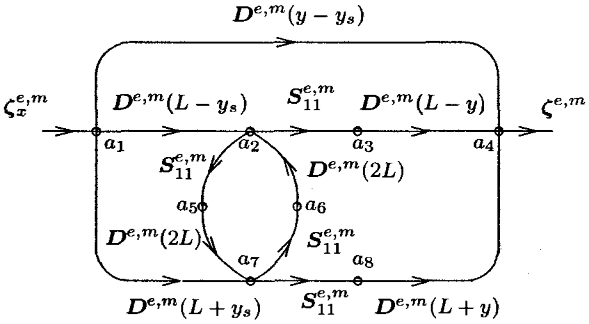

Figure 4.5: The signal flow graph picturing the multiple mode conversions and reflections inside a finite dielectric slab.

solution similar to (3.3.39) as

$$\zeta^{e,m} = \zeta_{\infty}^{e,m} + \zeta_{r++}^{e,m} + \zeta_{r--}^{e,m} + \zeta_{r+-}^{e,m} + \zeta_{r-+}^{e,m} \tag{4.4.1}$$

where the column vector $\zeta_{\infty}^{e,m}$ represents the direct path contribution of the modes, and it can be written similar to (3.3.30) as

$$\zeta_{\infty}^{e,m} = \boldsymbol{D}^{e,m}(y-y_s)\zeta_x^{e,m}. \tag{4.4.2}$$

Using the signal flow graph, we can write the other contributions similar to (3.3.35)-(3.3.38) as

$$\zeta_{r++}^{e,m} = \boldsymbol{D}^{e,m}(L-y)\boldsymbol{S}_{11}^{e,m}\boldsymbol{C}^{e,m}\boldsymbol{D}^{e,m}(L-y_s)\zeta_x^{e,m} \tag{4.4.3}$$

$$\zeta_{r--}^{e,m} = \boldsymbol{D}^{e,m}(L+y)\boldsymbol{S}_{11}^{e,m}\boldsymbol{C}^{e,m}\boldsymbol{D}^{e,m}(L+y_s)\zeta_x^{e,m} \tag{4.4.4}$$

$$\zeta_{r+-}^{e,m} = \boldsymbol{D}^{e,m}(L+y)\boldsymbol{S}_{11}^{e,m}\boldsymbol{C}^{e,m}\boldsymbol{D}^{e,m}(2L)\boldsymbol{S}_{11}^{e,m}\boldsymbol{D}^{e,m}(L-y_s)\zeta_x^{e,m} \tag{4.4.5}$$

$$\zeta_{r-+}^{e,m} = \boldsymbol{D}^{e,m}(L-y)\boldsymbol{S}_{11}^{e,m}\boldsymbol{C}^{e,m}\boldsymbol{D}^{e,m}(2L)\boldsymbol{S}_{11}^{e,m}\boldsymbol{D}^{e,m}(L+y_s)\zeta_x^{e,m} \tag{4.4.6}$$

$$\boldsymbol{C}^{e,m} = \left\{\boldsymbol{I} - [\boldsymbol{D}^{e,m}(2L)\boldsymbol{S}_{11}^{e,m}]^2\right\}^{-1} \tag{4.4.7}$$

where $\boldsymbol{S}_{11}^{e}$ and $\boldsymbol{S}_{11}^{m}$ represent the PEC and PMC scattering matrices and $\boldsymbol{I}$ is the identity matrix. The obtained column vector $\boldsymbol{\zeta}^{e,m}$ represents the amplitudes of the mode functions, $\zeta_{\nu,\tau}$, given by

$$G^{e_\nu, m_\tau} = \zeta_{\nu,\tau} e_{\nu,\tau}(x) \tag{4.4.8}$$

and the SW solution is expressed by

$$G_{finite}^{SW} = \sum_{\nu} G^{e_\nu}/2 + \sum_{\tau} G^{m_\tau}/2. \tag{4.4.9}$$

By replacing the G_{22}^{SW} with G_{finite}^{SW} in (3.3.25), the Green's function solution for the finite dielectric slab can be written as

$$G_{22} = -\frac{1}{4\pi j}\int_{P} \kappa_1 \eta_2 (G_{22x}^{m} + G_{22x}^{e})(G_{22y}^{m} + G_{22y}^{e}) d\mathrm{w} + G_{finite}^{SW} \tag{4.4.10}$$

where the integral represents the residual wave part obtained for the separable structure.

4.5 Results and Discussion

For validation, the results obtained by a MoM code for a SIS are compared with the results generated by HFSS. Referring to Fig. 4.1, we choose the slab thickness $2d = 20$ cm and the frequency $f = 1.8$ GHz. The end cap of the semi-infinite dielectric slab is placed at $y = L = 0.4$ m. The relative permittivity and conductivity of the slab are $\epsilon_r = 6$ and $\sigma_2 = 0.195$ mS/m, respectively. The exterior medium is free space. The source strength I_s is normalized so that it generates 1 V/m at a distance of 1 m in free space, and 0 dB corresponds to 1 V/m.

Fig. 4.6 shows the electric field along the top end of a semi-infinite dielectric slab

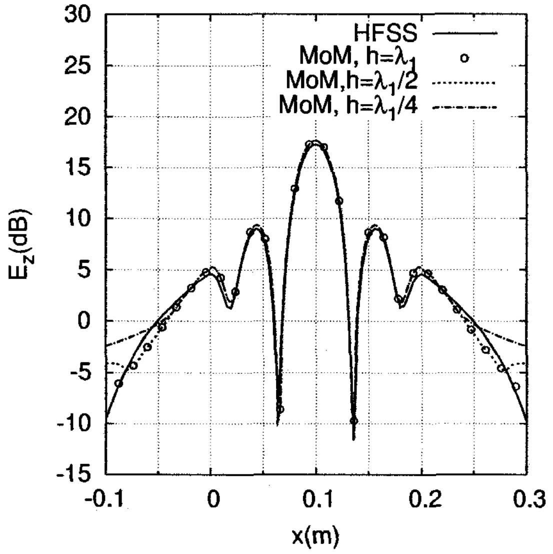

Figure 4.6: The electric field along the top end of a semi-infinite dielectric slab at $(x, y) = (x, 0.4)$ m. The slab thickness is $2d = 0.2$ m. The end cap is at $y = L = 0.4$ m, and the source is at $(x_s, y_s) = (0.1, -0.2)$ m.

at $y = L = 0.4$ m. The source is at $(x, y) = (0.1, -0.2)$ m. To form a 2D waveguide structure using HFSS, we placed our structure between two PEC parallel plates 1 cm apart at $z = \pm 0.5$ cm. We formed a $0.6 \times 0.8 \times 0.01$ m air box embedding the structure. The four faces of the air box parallel to the z axis were defined as radiation boundaries. The final mesh in HFSS had 47846 tetrahedra. According to (4.2.6), we approximate the equivalent current on a MoM region along $y = L$, where the MoM region spans the range $-h \leq x \leq 2d + h$. To observe the effect of varying h, we compared the calculated electric field for three different values of h. It was found that the electric field is most affected by the value of h when the field point is away from the slab surfaces at $x = 0$, $x = 0.2$ m. Convergence was observed when $h = \lambda_1$ (where λ_1 is the wavelength outside the dielectric slab). When we chose $h = \lambda_1$, it was found that the total electric field can be accurately calculated inside the dielectric slab. This is shown in Fig. 4.7 for the field point at $(x, y) = (0.1, y)$ m.

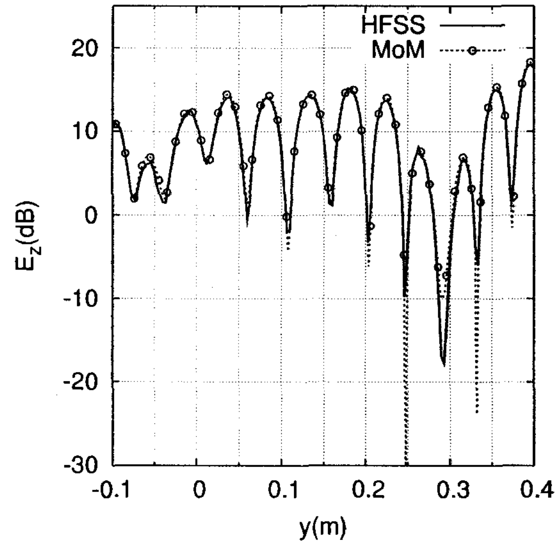

Figure 4.7: The electric field inside a semi-infinite dielectric slab. This validates the MoM solution which is used to find the scattering matrix of the end cap. The slab has a thickness of $2d = 0.2$ m. The source is at $(x_s, y_s) = (0.1, -0.2)$ m, and the field point is at $(x, y) = (0.1, y)$ m. The end cap is at $y = L = 0.4$ m.

Fig. 4.8 shows the electric field at $(x, y) = (0.05, y)$ m when the source was at $(x_s, y_s) = (0.05, -0.2)$ m. The result obtained for separable semi-infinite slab (S-SIS) is compared with the SIS results. The result is shown for the slab thickness $2d = 0.1$ m and $2d = 0.2$ m. It is observed that the S-SIS and SIS results agree better when $2d = 0.2$ m. We also verified other cases in the range $0.01 \leq 2d \leq 0.6$ m. The results showed that the results obtained by S-SIS was very different from SIS results when $2d \leq 0.07$ m. By increasing the slab thickness when $0.07 \leq 2d \leq 0.2$ m, the agreement between the results obtained for S-SIS and SIS was improved. This shows that using the Fresnel reflection coefficient for thicker SIS slabs gives more accurate results.

It was also observed that by moving the source to the center line of the slab at $(x_s, y_s) = (0.1, -0.2)$ m, the agreement shown in Fig. 4.8.b becomes better. For the case when the source is at the centerline of the slab, only the PMC modes contribute.

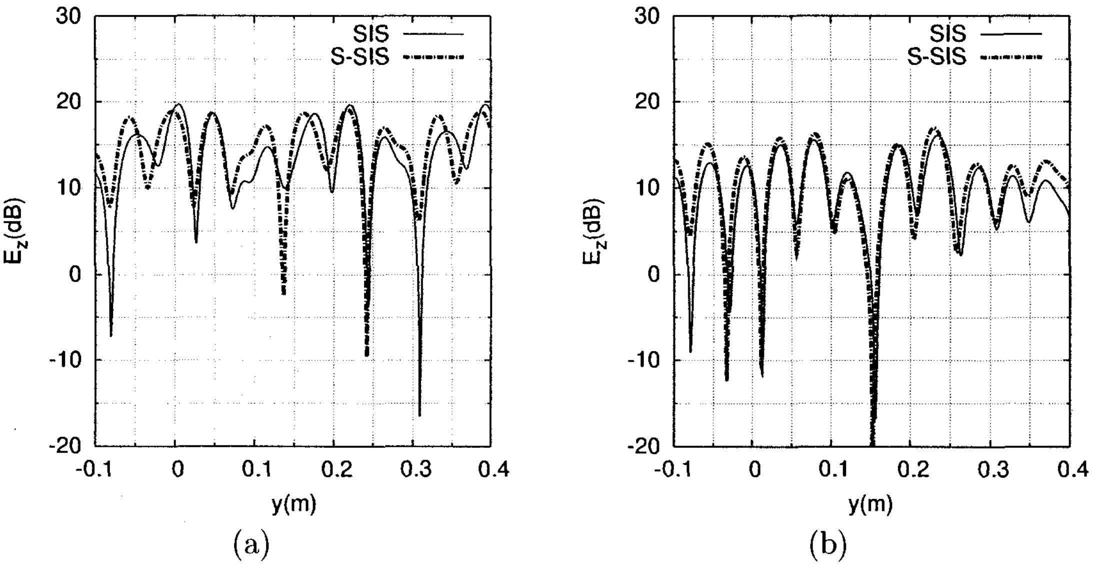

Figure 4.8: The comparison of the electric field inside a SIS and S-SIS. The source is at $(x_s, y_s) = (0.05, -0.2)$ m, and the field point is at $(x, y) = (0.05, y)$ m. The slab thickness is (a) $2d = 0.1$ m and (b) $2d = 0.2$ m.

This shows that using the Fresnel reflection coefficient for the PMC modes in a thick slab gives better results than using the Fresnel reflection coefficient for the PEC modes. Furthermore, the corner regions of a S-SIS affect the PEC modes more than the PMC modes. It is noted that a PMC mode electric field is strong along the center line of the slab, and it is weaker near the slab surface. On the other hand, a PEC mode electric field is zero at the center line of the slab, and it is strong at the slab surface. As a result, the corner regions at the end cap affect the PEC modes more than the PMC modes.

Fig. 4.9 shows the amplitude and phase variation of the first three diagonal elements of $\mathbf{\Gamma}^m$ and $\mathbf{\Lambda}^m$ versus the slab thickness. The diagonal elements of the equivalent scattering matrix $\mathbf{\Lambda}^m$ are obtained using (4.3.10). Furthermore, the elements of the reflection coefficient $\mathbf{\Gamma}^m$ are given in (4.3.4). The reflection coefficient matrix gives the reflected modes inside a S-SIS, while the equivalent scattering matrix is used for calculating the reflected modes inside a SIS. It was observed that by increasing

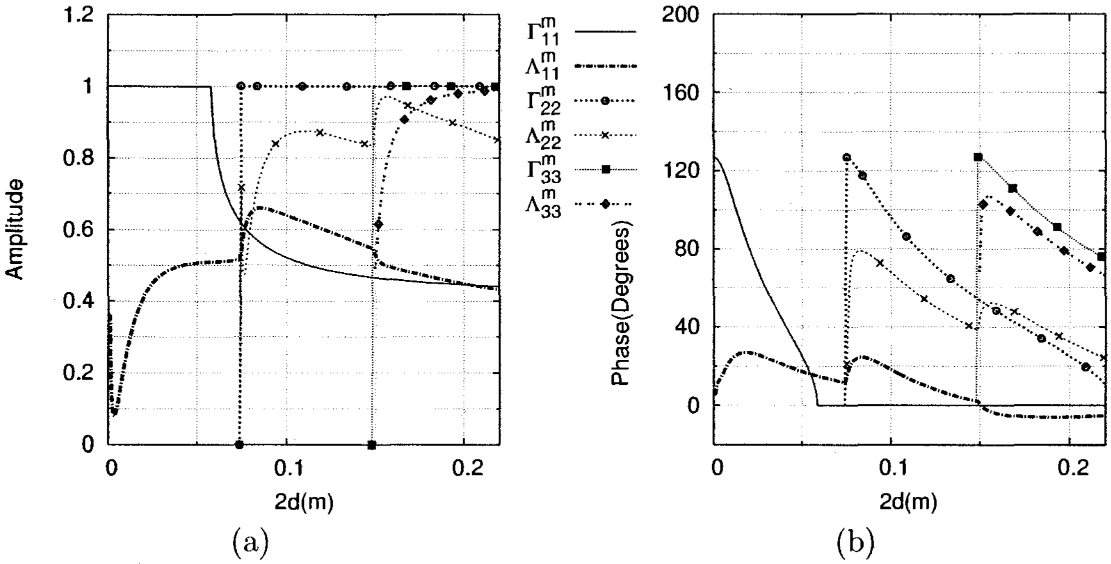

Figure 4.9: (a) The comparison of the (a) amplitude and (b) the phase of the first three elements of the reflection coefficient matrix $\mathbf{\Gamma}^m$ and the equivalent scattering matrix $\mathbf{\Lambda}^m$.

the slab thickness $2d$, the angle of incidence of each mode at the end cap (the positive angle that the plane wave terms of a SW mode make with the y axis) becomes smaller. As it is shown in Fig. 4.9.a, the angle of incidence for the first mode becomes smaller than the critical angle when $2d \geq 0.058$ m. When the slab thickness is $2d \leq 0.058$ m, the first mode is completely reflected at the end cap since $|\Gamma^m_{11}| = 1$. By increasing the slab thickness, it is observed that the reflection coefficient Γ^m_{11} shows closer behavior to Λ^m_{11}. Furthermore, it is shown that Γ^m_{ii} behaves more similarly to Λ^m_{ii} for the third PMC mode ($ii = 3$) than the first or second PMC mode.

Fig. 4.10 shows the electric field inside a $2L \times 2d = 0.5 \times 0.2$ m finite dielectric slab. The results obtained using the surface integral equation/method of moments for a finite slab (SIE/MoM-FS) are compared with the results computed by GF for the finite slab (GF-FS) and GF-SS. The reader is referred to Subsection 6.1.2 for more details on the SIE/MoM technique. For this slab size, the SIE/MoM-FS solved a 460×460 impedance matrix since the surface of the slab was divided into 230 cells.

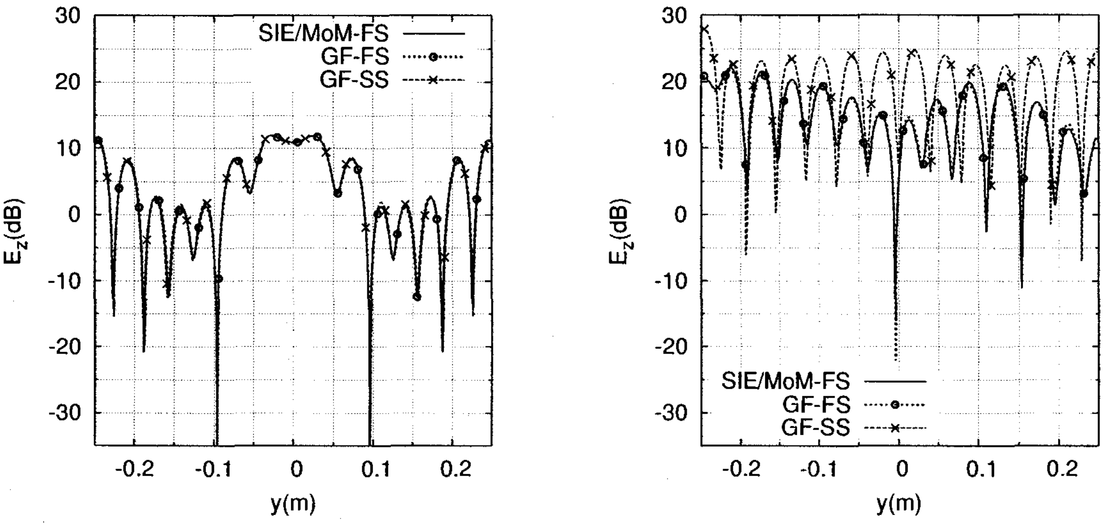

(a)

(b)

Figure 4.10: (a) The electric field inside a $2L \times 2d = 0.5 \times 0.2$ m finite dielectric slab. (a) The line source is at $(x_s, y_s) = (0.1, 0)$ m, and the field point is at $(x, y) = (0.04, y)$ m. (b) The line source is at $(x_s, y_s) = (0.02, -0.22)$ m, and the field point is at $(x, y) = (0.01, y)$ m.

This is more efficient than HFSS which uses volume tetrahedral mesh to solve this problem. In using HFSS, the final volume mesh had 30337 tetrahedra. Furthermore, to obtain the scattering matrix at the end cap of a SIS with the thickness $2d = 0.2$ m, a 64×64 impedance matrix was solved. The scattering matrix was then used in GF-FS to solve the FS problem. The advantage of using GF-FS is that increasing the slab height of the FS does not have any additional computational costs. As a result, it is suitable for modeling large slabs.

Fig. 4.10.a shows the case when the source is at $(x_s, y_s) = (0.1, 0)$ m and the field point is at $(x, y) = (0.04, y)$ m. The pole locations of the SS were already shown in Fig. 3.18.b. It was observed that the poles of G_x are not close to the poles of G_y for this case. The result obtained by GF-FS agrees well with the results computed by GF-SS. This shows that the SW modes are not sensitive to the material in the corner regions.

Fig. 4.10.b shows the case when the source is at $(x_s, y_s) = (0.02, -0.22)$ m and the field point is at $(x, y) = (0.01, y)$ m. The pole locations of the SS were already shown in Fig. 3.19.b where one of the SW modes inside the SS was showing "close to resonance" behavior. The results show that the GF-SS cannot model the finite slab when one of the G_x poles is very close to a G_y pole.

Fig. 4.11 compares the electric field inside a FS and SS when the slab size is $2L \times 2d = 0.535 \times 0.2$ m. The source is at $(x_s, y_s) = (0.1, 0)$ m, and the field point is at $(x, y) = (0.04, y)$ m. The pole locations of the SS are shown in Fig. 3.21.b where two poles of G_x are very close to two poles of G_y. As a result, a very strong electric field is observed inside the SS which is very different from the electric field inside a FS. In this case, it is a poor approximation to use the SS Green's function to compute the electric field in an actual FS which we wish to model. It is also shown that the GF-FS results agree well with the results obtained by SIE/MoM-FS. This validates the presented GF-FS.

Fig. 4.12 shows the electric field inside a FS when the source is close to the end cap at $(x_s, y_s) = (0.01, 0.26)$ m, and the field point is at $(x, y) = (0.02, y)$ m. The slab size is unchanged. Although the source is very close to the slab end cap, the GF-FS still agrees very well with SIE/MoM-FS. In calculating the GF-FS result, the end cap scattering matrix was used. The scattering matrix was calculated by finding the pulse bases currents at the end cap. However, the pulse bases has a near field contribution that is not included in the total field near the end cap.

Fig. 4.13 shows the electric field inside a FS along the width of the slab when the source is at $(x_s, y_s) = (0.1, -0.23)$ m and the field point is at $(x, y) = (x, -0.24)$ m. The GF-FS is the total solution, which consists of the residual wave plus the SW of the FS (SW-FS). The plot also shows the SW-FS alone, i.e. the total with the residual wave omitted. It can be seen that the residual wave is strong, and it makes

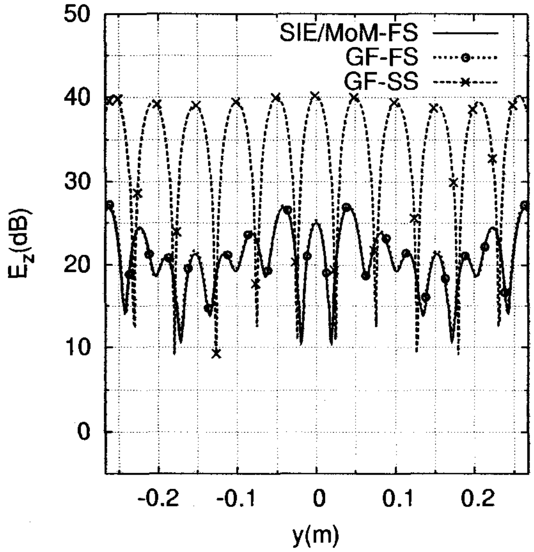

Figure 4.11: The electric field inside a FS. The slab has a thickness of $2d = 0.2$ m and a height of $2L = 0.535$ m. The source is at $(x_s, y_s) = (0.1, 0)$ m, and the field point is at $(x, y) = (0.04, y)$ m.

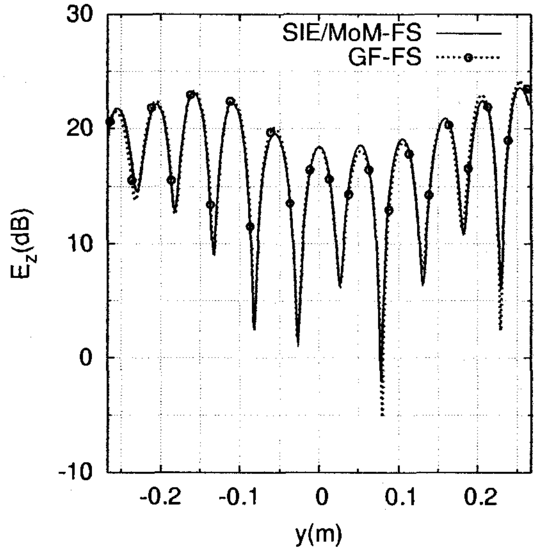

Figure 4.12: The electric field inside a FS. The slab has a thickness of $2d = 0.2$ m and a height of $2L = 0.535$ m. The source is at $(x_s, y_s) = (0.01, 0.26)$ m, and the field point is at $(x, y) = (0.02, y)$ m.

a significant contribution to the total field. Furthermore, the residual wave provides the necessary correction to the SW field so that the total matches the SIE/MoM-FS

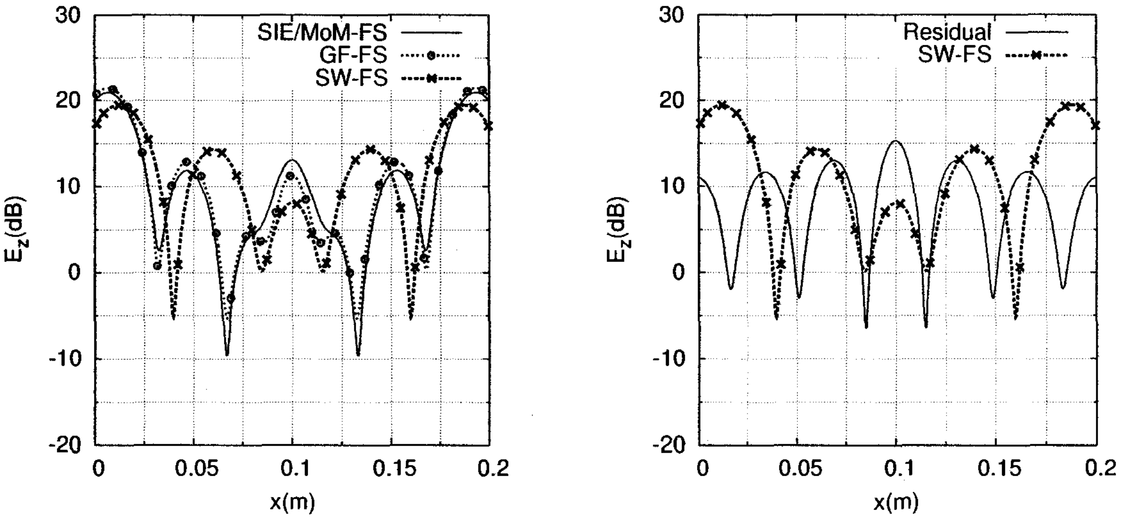

(a) (b)

Figure 4.13: (a) The electric field inside a FS. The source is at $(x_s, y_s) = (0.1, -0.23)$ m, and the field point is at $(x, y) = (x, -0.24)$ m. (a) If the residual wave is omitted, only the SW-FS remains which doesn't match the SIE/MoM-FS. (b) The residual wave is comparable to the SW-FS.

solution. It is also seen that the MoM correction is necessary for the SW's but not for the residual wave. This happens because the SW part of the SS solution is very sensitive to the material in the corner region. Furthermore, the material in the corner regions affects the resonance behavior of the SW-FS. However, the residual part of the solution cannot experience a resonant behavior since it decays fast in the y direction.

Chapter 5

Exterior Analysis of a Finite Thick Dielectric Slab

In the previous chapter, the interior Green's function for a finite dielectric slab was obtained. The interior Green's function can be used to calculate the electric field when the source and the field point are both inside the dielectric slab. In this chapter, we present a simple procedure that can be used in order to obtain the electric field using the interior Green's function when the source and/or the field point is exterior to the dielectric slab. Applying the surface equivalence principle, we can obtain the exterior field generated by an interior source. This can be done by computing the surface equivalent currents using the interior Green's function. The equivalent surface currents together with the free-space Green's function can be used to obtain the field at any point outside the slab. Applying the reciprocity theorem, we can interchange the source and the field point. As a result, we are able to calculate the interior field due to an exterior line source. This is used later for computing the exterior Green's function where we first obtain the electric and magnetic fields on the slab surface generated by an exterior line source. Having the electric and magnetic fields on the slab surface will provide the surface equivalent currents. These currents will be the sources of the scattered field in the exterior region. This method has been reported in [28].

5.1 Case 1: Source Inside, Field Point Outside

5.1.1 Electric Line Source

Fig. 5.1.a shows a finite dielectric slab of height $2L$ and thickness $2d$, having a permittivity of ϵ_2. A current line source which has a strength of I_s is placed inside the dielectric slab at $\boldsymbol{\rho}_s = x_s\hat{\boldsymbol{x}} + y_s\hat{\boldsymbol{y}}$. The field point is outside the dielectric slab.

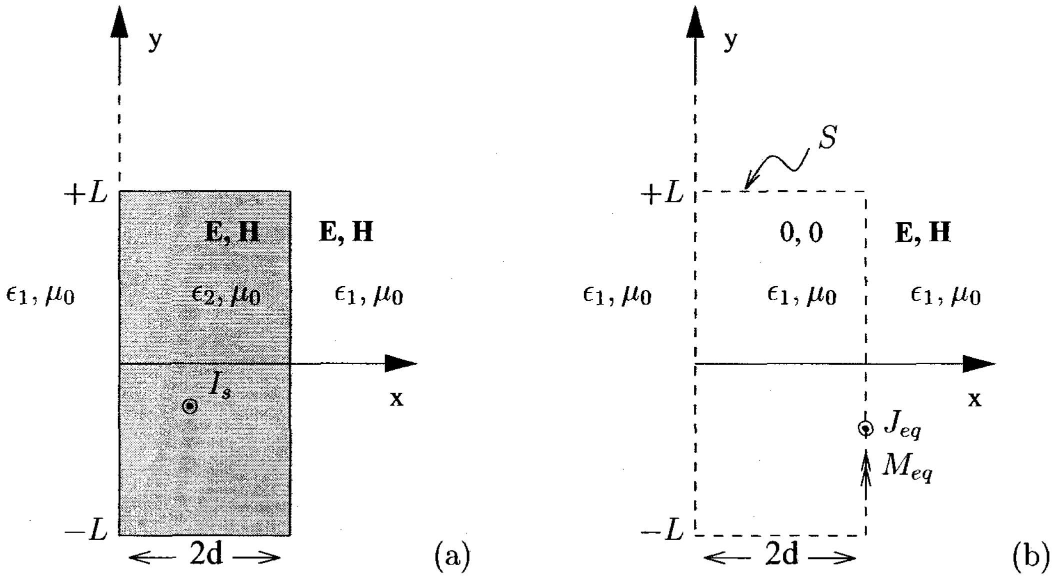

Figure 5.1: (a) An electric line source inside a finite dielectric slab. (b) Applying the surface equivalent theorem to obtain the exterior field, the dielectric slab is replaced by the equivalent surface currents J_{eq} and M_{eq}.

In order to obtain the electric field outside the dielectric slab, we use the surface equivalence principle and the interior Green's function as follows. Since the source is inside the dielectric slab, we can calculate the surface fields on the dielectric slab boundary by using the interior Green's function. Having the total field on the dielectric slab boundary, the equivalent currents on the dielectric slab surface can be obtained. By using the surface equivalence principle, we can replace the actual current source by the equivalent sources on the boundary of the dielectric slab. The equivalent sources generate the same electric field as the actual sources in the exterior region, and zero field in the interior region. The interior region material can be replaced with any material since the interior region has zero field. It is always convenient to replace the interior region material with the same material as the exterior region. As a result, the exterior field can be obtained by using the free space Green's function since the equivalent sources radiate in a homogeneous material having ϵ_1, μ_1 everywhere in space as shown in Fig. 5.1.b.

The procedure which was mentioned above is applied to the dielectric slab shown in Fig. 5.1.a. First, the fields on the dielectric slab surface should be calculated. A point on the surface of the dielectric slab is defined by $\boldsymbol{\rho}'_n$ as

$$\begin{aligned} &\boldsymbol{\rho}'_1 = y'\hat{\boldsymbol{y}} && -L \le y' \le L \\ &\boldsymbol{\rho}'_2 = 2d\hat{\boldsymbol{x}} + y'\hat{\boldsymbol{y}} && -L \le y' \le L \\ &\boldsymbol{\rho}'_3 = x'\hat{\boldsymbol{x}} - L\hat{\boldsymbol{y}} && 0 \le x' \le 2d \\ &\boldsymbol{\rho}'_4 = x'\hat{\boldsymbol{x}} + L\hat{\boldsymbol{y}} && 0 \le x' \le 2d. \end{aligned} \tag{5.1.1}$$

The electric field on the dielectric slab surface which is generated by the electric line source has only a z-directed component. It can be expressed as

$$\boldsymbol{E}(\boldsymbol{\rho}_s, \boldsymbol{\rho}'_n) = E_z(\boldsymbol{\rho}_s, \boldsymbol{\rho}'_n)\hat{\boldsymbol{z}} \tag{5.1.2}$$

where $E_z(\boldsymbol{\rho}_s, \boldsymbol{\rho}'_n)$ can be obtained according to (3.1.5) by using the interior Green's function as

$$E_z(\boldsymbol{\rho}_s, \boldsymbol{\rho}'_n) = -j\omega\mu_0 I_s G_{22}(\boldsymbol{\rho}_s, \boldsymbol{\rho}'_n). \tag{5.1.3}$$

The interior Green's function G_{22} is given in (4.4.10). Furthermore, the magnetic field on the surface of the dielectric slab is expressed as

$$\boldsymbol{H}(\boldsymbol{\rho}_s, \boldsymbol{\rho}'_n) = \begin{cases} H_x(\boldsymbol{\rho}_s, \boldsymbol{\rho}'_n)\hat{\boldsymbol{x}} & n = 3, 4 \\ H_y(\boldsymbol{\rho}_s, \boldsymbol{\rho}'_n)\hat{\boldsymbol{y}} & n = 1, 2 \end{cases} \tag{5.1.4}$$

where $H_x(\boldsymbol{\rho}_s, \boldsymbol{\rho}'_n)$ and $H_y(\boldsymbol{\rho}_s, \boldsymbol{\rho}'_n)$ can be obtained using Maxwell's equation ($\nabla \times \boldsymbol{E} = -j\omega\mu\boldsymbol{H}$) as

$$H_x(\boldsymbol{\rho}_s, \boldsymbol{\rho}'_n) = -\frac{1}{j\omega\mu_0} \frac{\partial E_z(\boldsymbol{\rho}_s, \boldsymbol{\rho})}{\partial y}\bigg|_{\boldsymbol{\rho}'_n} = I_s \frac{\partial G_{22}(\boldsymbol{\rho}', \boldsymbol{\rho})}{\partial y}\bigg|_{(\boldsymbol{\rho}_s, \boldsymbol{\rho}'_n)} \tag{5.1.5}$$

$$H_y(\boldsymbol{\rho}_s, \boldsymbol{\rho}'_n) = \frac{1}{j\omega\mu_0} \frac{\partial E_z(\boldsymbol{\rho}_s, \boldsymbol{\rho})}{\partial x}\bigg|_{\boldsymbol{\rho}'_n} = -I_s \frac{\partial G_{22}(\boldsymbol{\rho}', \boldsymbol{\rho})}{\partial x}\bigg|_{(\boldsymbol{\rho}_s, \boldsymbol{\rho}'_n)}. \tag{5.1.6}$$

It is noted that the vectors $\boldsymbol{\rho} = x\hat{\boldsymbol{x}} + y\hat{\boldsymbol{y}}$ and $\boldsymbol{\rho}' = x'\hat{\boldsymbol{x}} + y'\hat{\boldsymbol{y}}$, which are the Green's function variables, define the source and field point, respectively. The equivalent currents on the surface of the dielectric slab can be obtained by applying the boundary condition as

$$\boldsymbol{M}_{eq} = -\hat{\boldsymbol{n}} \times \boldsymbol{E}(\boldsymbol{\rho}_s, \boldsymbol{\rho}'_n) \tag{5.1.7}$$

$$\boldsymbol{J}_{eq} = \hat{\boldsymbol{n}} \times \boldsymbol{H}(\boldsymbol{\rho}_s, \boldsymbol{\rho}'_n) \tag{5.1.8}$$

where the unit vector $\hat{\boldsymbol{n}}$ is pointing toward the exterior region and is normal to the boundary. The equivalent electric and magnetic currents on the dielectric slab boundary are denoted by $\boldsymbol{J}_{eq}$ and $\boldsymbol{M}_{eq}$, respectively. Using (5.1.2), we can write (5.1.7) in scalar form as

$$[M_x(\boldsymbol{\rho}_s, \boldsymbol{\rho}'_n), M_y(\boldsymbol{\rho}_s, \boldsymbol{\rho}'_n)] = \begin{cases} [\,0\,,\ (-1)^n E_z(\boldsymbol{\rho}_s, \boldsymbol{\rho}'_n)] & n = 1, 2 \\ [(-1)^{(n-1)} E_z(\boldsymbol{\rho}_s, \boldsymbol{\rho}'_n)\ ,\ 0\,] & n = 3, 4 \end{cases} \tag{5.1.9}$$

where M_x and M_y are the x and y components of the equivalent magnetic current, or

$$\boldsymbol{M}_{eq} = M_x(\boldsymbol{\rho}_s, \boldsymbol{\rho}_n')\hat{\boldsymbol{x}} + M_y(\boldsymbol{\rho}_s, \boldsymbol{\rho}_n')\hat{\boldsymbol{y}}. \tag{5.1.10}$$

Similarly, we can write (5.1.8) in scalar form by using (5.1.4) as

$$J_z(\boldsymbol{\rho}_s, \boldsymbol{\rho}_n') = \begin{cases} (-1)^n H_y(\boldsymbol{\rho}_s, \boldsymbol{\rho}_n') & n = 1, 2 \\ (-1)^{(n-1)} H_x(\boldsymbol{\rho}_s, \boldsymbol{\rho}_n') & n = 3, 4 \end{cases} \tag{5.1.11}$$

where

$$\boldsymbol{J}_{eq} = J_z(\boldsymbol{\rho}_s, \boldsymbol{\rho}_n')\hat{\boldsymbol{z}}. \tag{5.1.12}$$

By using the free space Green's function, the exterior electric field at $\boldsymbol{\rho}_o = x_o\hat{\boldsymbol{x}} + y_o\hat{\boldsymbol{y}}$ generated by the surface equivalent electric current can be obtained. As a result, using (5.1.12) and (A.5-7) in (3.1.5) gives the electric field E_z^J generated by the surface electric current as

$$\begin{aligned} E_z^J(\boldsymbol{\rho}_s, \boldsymbol{\rho}_o) = &-\frac{w\mu_0}{4} \int_{-L}^{L} \Big[J_z(\boldsymbol{\rho}_s, \boldsymbol{\rho}_1') H_0^{(2)}(k_1|\boldsymbol{\rho}_o - \boldsymbol{\rho}_1'|) \\ &\qquad + J_z(\boldsymbol{\rho}_s, \boldsymbol{\rho}_2') H_0^{(2)}(k_1|\boldsymbol{\rho}_o - \boldsymbol{\rho}_2'|) \Big] dy' \\ &-\frac{w\mu_0}{4} \int_{0}^{2d} \Big[J_z(\boldsymbol{\rho}_s, \boldsymbol{\rho}_3') H_0^{(2)}(k_1|\boldsymbol{\rho}_o - \boldsymbol{\rho}_3'|) \\ &\qquad + J_z(\boldsymbol{\rho}_s, \boldsymbol{\rho}_4') H_0^{(2)}(k_1|\boldsymbol{\rho}_o - \boldsymbol{\rho}_4'|) \Big] dx'. \end{aligned} \tag{5.1.13}$$

Using (5.1.10), (5.1.1) and (A.5-8)-(A.5-9), we can write the exterior electric field generated by the equivalent magnetic surface current as

$$\begin{aligned}E_z^M(\boldsymbol{\rho}_s,\boldsymbol{\rho}_o) = \frac{k_1}{4j}\int_{-L}^{L}\Bigg[&M_y(\boldsymbol{\rho}_s,\boldsymbol{\rho}_1')\frac{x_o}{|\boldsymbol{\rho}_o-\boldsymbol{\rho}_1'|}H_1^{(2)}(k_1|\boldsymbol{\rho}_o-\boldsymbol{\rho}_1'|)\\ &+M_y(\boldsymbol{\rho}_s,\boldsymbol{\rho}_2')\frac{x_o-2d}{|\boldsymbol{\rho}_o-\boldsymbol{\rho}_2'|}H_1^{(2)}(k_1|\boldsymbol{\rho}_o-\boldsymbol{\rho}_2'|)\Bigg]dy'\\ -\frac{k_1}{4j}\int_{0}^{2d}\Bigg[&M_x(\boldsymbol{\rho}_s,\boldsymbol{\rho}_3')\frac{y_o+L}{|\boldsymbol{\rho}_o-\boldsymbol{\rho}_3'|}H_1^{(2)}(k_1|\boldsymbol{\rho}_o-\boldsymbol{\rho}_3'|)\\ &+M_x(\boldsymbol{\rho}_s,\boldsymbol{\rho}_4')\frac{y_o-L}{|\boldsymbol{\rho}_o-\boldsymbol{\rho}_4'|}H_1^{(2)}(k_1|\boldsymbol{\rho}_o-\boldsymbol{\rho}_4'|)\Bigg]dx'\end{aligned} \tag{5.1.14}$$

Using (5.1.5)-(5.1.6) and (5.1.11), we can write (5.1.13) as

$$\begin{aligned}E_z^J(\boldsymbol{\rho}_s,\boldsymbol{\rho}_o) = -\frac{\omega\mu_0}{4}I_s\int_{-L}^{L}\Bigg[&\left.\frac{\partial G_{22}(\boldsymbol{\rho}',\boldsymbol{\rho})}{\partial x}\right|_{(\boldsymbol{\rho}_s,\boldsymbol{\rho}_1')}H_0^{(2)}(k_1|\boldsymbol{\rho}_o-\boldsymbol{\rho}_1'|)\\ &-\left.\frac{\partial G_{22}(\boldsymbol{\rho}',\boldsymbol{\rho})}{\partial x}\right|_{(\boldsymbol{\rho}_s,\boldsymbol{\rho}_2')}H_0^{(2)}(k_1|\boldsymbol{\rho}_o-\boldsymbol{\rho}_2'|)\Bigg]dy'\\ -\frac{\omega\mu_0}{4}I_s\int_{0}^{2d}\Bigg[&\left.\frac{\partial G_{22}(\boldsymbol{\rho}',\boldsymbol{\rho})}{\partial y}\right|_{(\boldsymbol{\rho}_s,\boldsymbol{\rho}_3')}H_0^{(2)}(k_1|\boldsymbol{\rho}_o-\boldsymbol{\rho}_3'|)\\ &-\left.\frac{\partial G_{22}(\boldsymbol{\rho}',\boldsymbol{\rho})}{\partial y}\right|_{(\boldsymbol{\rho}_s,\boldsymbol{\rho}_4')}H_0^{(2)}(k_1|\boldsymbol{\rho}_o-\boldsymbol{\rho}_4'|)\Bigg]dx'.\end{aligned} \tag{5.1.15}$$

Similarly, the electric field due the equivalent magnetic surface current given in (5.1.14) can be written by using (5.1.3) and (5.1.9) as

$$\begin{aligned}E_z^M(\boldsymbol{\rho}_s,\boldsymbol{\rho}_o) = \frac{\omega\mu_0 k_1}{4}I_s\int_{-L}^{L}\Bigg[&G_{22}(\boldsymbol{\rho}_s,\boldsymbol{\rho}_1')\frac{x_o}{|\boldsymbol{\rho}_o-\boldsymbol{\rho}_1'|}H_1^{(2)}(k_1|\boldsymbol{\rho}_o-\boldsymbol{\rho}_1'|)\\ &-G_{22}(\boldsymbol{\rho}_s,\boldsymbol{\rho}_2')\frac{x_o-2d}{|\boldsymbol{\rho}_o-\boldsymbol{\rho}_2'|}H_1^{(2)}(k_1|\boldsymbol{\rho}_o-\boldsymbol{\rho}_2'|)\Bigg]dy'\\ +\frac{\omega\mu_0 k_1}{4}I_s\int_{0}^{2d}\Bigg[&G_{22}(\boldsymbol{\rho}_s,\boldsymbol{\rho}_3')\frac{y_o+L}{|\boldsymbol{\rho}_o-\boldsymbol{\rho}_3'|}H_1^{(2)}(k_1|\boldsymbol{\rho}_o-\boldsymbol{\rho}_3'|)\\ &-G_{22}(\boldsymbol{\rho}_s,\boldsymbol{\rho}_4')\frac{y_o-L}{|\boldsymbol{\rho}_o-\boldsymbol{\rho}_4'|}H_1^{(2)}(k_1|\boldsymbol{\rho}_o-\boldsymbol{\rho}_4'|)\Bigg]dx'.\end{aligned} \tag{5.1.16}$$

In summary, the field in the exterior region that is generated by the equivalent electric and magnetic surface currents can be written as

$$E_z(\boldsymbol{\rho}_s, \boldsymbol{\rho}_o) = E_z^J(\boldsymbol{\rho}_s, \boldsymbol{\rho}_o) + E_z^M(\boldsymbol{\rho}_s, \boldsymbol{\rho}_o) \tag{5.1.17}$$

where E_z^J and E_z^M are given in (5.1.15) and (5.1.16), respectively. By performing numerical integrations, (5.1.15) and (5.1.16) can be evaluated.

5.2 Case 2: Source Outside, Field Point Inside

In order to find the electric field inside a finite dielectric slab generated by a current line source in the exterior region, we can apply the reciprocity theorem so that the source and the field point can be interchanged. As a result, we can use the result that was obtained in Section 5.1.

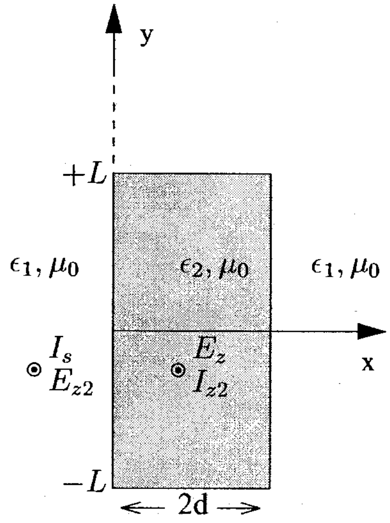

Figure 5.2: A finite dielectric slab.

Fig. 5.2 shows a primary current line source $I_s(\boldsymbol{\rho}_s)$ exterior to a finite dielectric slab which generates the electric field $E_z(\boldsymbol{\rho}_s, \boldsymbol{\rho}_o)$ at the observation point $\boldsymbol{\rho}_o$ in the interior region. To apply reciprocity, we assume another secondary current line source

$I_{z2}(\boldsymbol{\rho}_o)$ at the location of E_z which generates the $E_{z2}(\boldsymbol{\rho}_o, \boldsymbol{\rho}_s)$ at the location of primary current line source $I_s(\boldsymbol{\rho}_s)$. According to the reciprocity theorem, we have

$$I_s(\boldsymbol{\rho}_s)E_{z2}(\boldsymbol{\rho}_o, \boldsymbol{\rho}_s) = I_{z2}(\boldsymbol{\rho}_o)E_z(\boldsymbol{\rho}_s, \boldsymbol{\rho}_o) \tag{5.2.1}$$

which can be written as

$$E_z(\boldsymbol{\rho}_s, \boldsymbol{\rho}_o) = I_s(\boldsymbol{\rho}_s)E_{z2}((\boldsymbol{\rho}_o, \boldsymbol{\rho}_s). \tag{5.2.2}$$

where $I_{z2}(\boldsymbol{\rho}_o) = 1$ is assumed. The electric field outside the dielectric slab, which is generated by $I_{z2}(\boldsymbol{\rho}_o) = 1$, is denoted by E_{z2} and can be written as

$$E_{z2}(\boldsymbol{\rho}_o, \boldsymbol{\rho}_s) = E^J_{z2}(\boldsymbol{\rho}_o, \boldsymbol{\rho}_s) + E^M_{z2}(\boldsymbol{\rho}_o, \boldsymbol{\rho}_s) \tag{5.2.3}$$

where E^J_{z2} is the electric field generated by the electric surface current. Using (5.1.15), E^J_{z2} which is originally generated by $I_{z2}(\boldsymbol{\rho}_o) = 1$ can be written as

$$\begin{aligned} E^J_{z2}(\boldsymbol{\rho}_o, \boldsymbol{\rho}_s) = &-\frac{\omega\mu_0}{4}\int_{-L}^{L}\left[\left.\frac{\partial G_{22}(\boldsymbol{\rho}', \boldsymbol{\rho})}{\partial x}\right|_{(\boldsymbol{\rho}_o, \boldsymbol{\rho}'_1)} H_0^{(2)}(k_1|\boldsymbol{\rho}_s - \boldsymbol{\rho}'_1|)\right. \\ &\left.-\left.\frac{\partial G_{22}(\boldsymbol{\rho}', \boldsymbol{\rho})}{\partial x}\right|_{(\boldsymbol{\rho}_o, \boldsymbol{\rho}'_2)} H_0^{(2)}(k_1|\boldsymbol{\rho}_s - \boldsymbol{\rho}'_2|)\right] dy' \\ &-\frac{\omega\mu_0}{4}\int_{0}^{2d}\left[\left.\frac{\partial G_{22}(\boldsymbol{\rho}', \boldsymbol{\rho})}{\partial y}\right|_{(\boldsymbol{\rho}_o, \boldsymbol{\rho}'_3)} H_0^{(2)}(k_1|\boldsymbol{\rho}_s - \boldsymbol{\rho}'_3|)\right. \\ &\left.-\left.\frac{\partial G_{22}(\boldsymbol{\rho}', \boldsymbol{\rho})}{\partial y}\right|_{(\boldsymbol{\rho}_o, \boldsymbol{\rho}'_4)} H_0^{(2)}(k_1|\boldsymbol{\rho}_s - \boldsymbol{\rho}'_4|)\right] dx'. \end{aligned} \tag{5.2.4}$$

Similarly, the exterior electric field E^M_{z2} generated by the surface magnetic current can be written by using (5.1.16) as

$$\begin{aligned} E_{z2}^{M}(\boldsymbol{\rho}_o, \boldsymbol{\rho}_s) = \frac{\omega\mu_0 k_1}{4} \int_{-L}^{L} & \left[G_{22}(\boldsymbol{\rho}_o, \boldsymbol{\rho}_1') \frac{x_s}{|\boldsymbol{\rho}_s - \boldsymbol{\rho}_1'|} H_1^{(2)}(k_1 |\boldsymbol{\rho}_s - \boldsymbol{\rho}_1'|) \right. \\ & \left. - G_{22}(\boldsymbol{\rho}_o, \boldsymbol{\rho}_2') \frac{x_s - 2d}{|\boldsymbol{\rho}_s - \boldsymbol{\rho}_2'|} H_1^{(2)}(k_1 |\boldsymbol{\rho}_s - \boldsymbol{\rho}_2'|) \right] dy' \\ + \frac{\omega\mu_0 k_1}{4} \int_{0}^{2d} & \left[G_{22}(\boldsymbol{\rho}_o, \boldsymbol{\rho}_3') \frac{y_s + L}{|\boldsymbol{\rho}_s - \boldsymbol{\rho}_3'|} H_1^{(2)}(k_1 |\boldsymbol{\rho}_s - \boldsymbol{\rho}_3'|) \right. \\ & \left. - G_{22}(\boldsymbol{\rho}_o, \boldsymbol{\rho}_4') \frac{y_s - L}{|\boldsymbol{\rho}_s - \boldsymbol{\rho}_4'|} H_1^{(2)}(k_1 |\boldsymbol{\rho}_s - \boldsymbol{\rho}_4'|) \right] dx' \end{aligned} \tag{5.2.5}$$

where $I_{z2}(\boldsymbol{\rho}_o) = 1$ is assumed.

In summary, the interior electric field at $\boldsymbol{\rho}_o = x\hat{\boldsymbol{x}} + y\hat{\boldsymbol{y}}$ generated by an exterior line source I_s at $\boldsymbol{\rho}_s = x_s\hat{\boldsymbol{x}} + y_s\hat{\boldsymbol{y}}$ can be obtained by (5.2.2) with E_{z2}, E_{z2}^{J} and E_{z2}^{M} given in (5.2.3), (5.2.4) and (5.2.5), respectively.

5.3 Case 3: Source Outside, Field Point Outside

In this section, we will investigate a solution for the case when the source and the observation points are both outside the finite dielectric slab. In doing do, we use the interior Green's function solution. In order to obtain the exterior field due to an exterior source, we use the surface equivalence principle. Fig. 5.3.a shows a line source with the strength I_s outside a dielectric slab at $\boldsymbol{\rho}_s = x_s\hat{\boldsymbol{x}} + y_s\hat{\boldsymbol{y}}$. If the total electric and magnetic fields can be obtained on the surface of the dielectric slab, the surface equivalence principle can be used to obtain the scattered field in the exterior region. The total electric field on the surface of the dielectric slab can be obtained by the same procedure as described in Section 5.2. The scattered field can be written as

$$E_z(\boldsymbol{\rho}_s, \boldsymbol{\rho}_o) = E_z^{M}(\boldsymbol{\rho}_s, \boldsymbol{\rho}_o) + E_z^{J}(\boldsymbol{\rho}_s, \boldsymbol{\rho}_o) \tag{5.3.1}$$

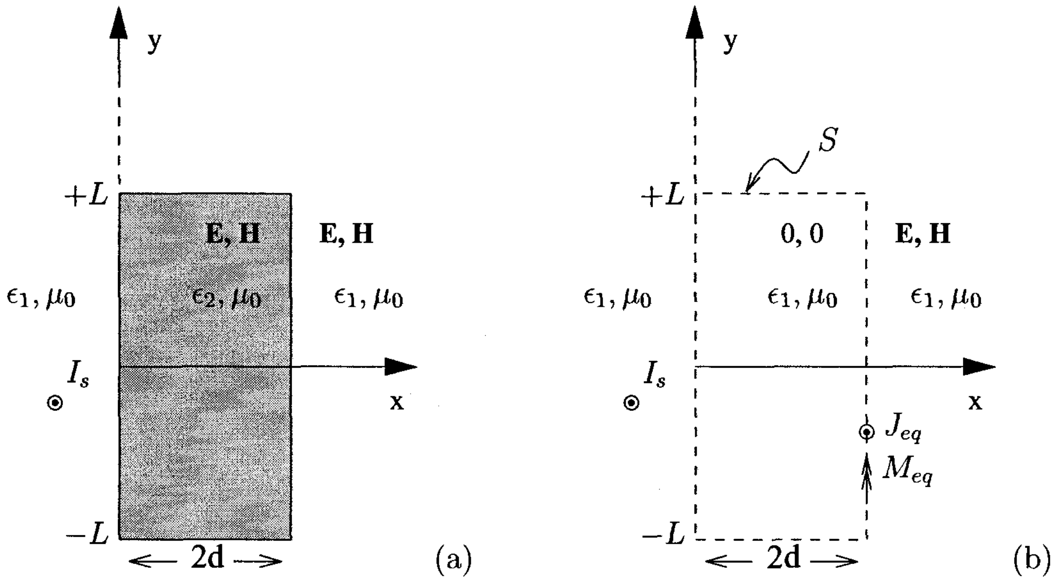

Figure 5.3: (a) An electric line source outside a finite dielectric slab. (b) Surface equivalence principle applied to the interior region.

where E_z^J and E_z^M are the electric fields due to the surface equivalent electric and magnetic current. Using (5.1.12) and (5.1.10), we can write E_z^J and E_z^M similar to (5.1.13) and (5.1.14) as

$$
\begin{aligned}
E_z^J(\boldsymbol{\rho}_s,\boldsymbol{\rho}_o) = -\frac{w\mu_0}{4}\int_{-L}^{L}\Big[& J_z(\boldsymbol{\rho}_s,\boldsymbol{\rho}_1'')H_0^{(2)}(k|\boldsymbol{\rho}_o-\boldsymbol{\rho}_1''|) \\
& + J_z(\boldsymbol{\rho}_s,\boldsymbol{\rho}_2'')H_0^{(2)}(k|\boldsymbol{\rho}_o-\boldsymbol{\rho}_2''|)\Big]dy'' \\
-\frac{w\mu_0}{4}\int_{0}^{2d}\Big[& J_z(\boldsymbol{\rho}_s,\boldsymbol{\rho}_3'')H_0^{(2)}(k|\boldsymbol{\rho}_o-\boldsymbol{\rho}_3''|) \\
& + J_z(\boldsymbol{\rho}_s,\boldsymbol{\rho}_4'')H_0^{(2)}(k|\boldsymbol{\rho}_o-\boldsymbol{\rho}_4''|)\Big]dx''
\end{aligned}
\tag{5.3.2}
$$

$$\begin{aligned}E_z^M(\boldsymbol{\rho}_s,\boldsymbol{\rho}_o) = \frac{k}{4j}\int_{-L}^{L}&\Bigg[M_y(\boldsymbol{\rho}_s,\boldsymbol{\rho}_1'')\frac{x_o}{|\boldsymbol{\rho}_o-\boldsymbol{\rho}_1''|}H_1^{(2)}(k|\boldsymbol{\rho}_o-\boldsymbol{\rho}_1''|)\\ &+M_y(\boldsymbol{\rho}_s,\boldsymbol{\rho}_2'')\frac{x_o-2d}{|\boldsymbol{\rho}_o-\boldsymbol{\rho}_2''|}H_1^{(2)}(k|\boldsymbol{\rho}_o-\boldsymbol{\rho}_2''|)\Bigg]dy''\\ -\frac{k}{4j}\int_{0}^{2d}&\Bigg[M_x(\boldsymbol{\rho}_s,\boldsymbol{\rho}_3'')\frac{y_o+L}{|\boldsymbol{\rho}_o-\boldsymbol{\rho}_3''|}H_1^{(2)}(k|\boldsymbol{\rho}_o-\boldsymbol{\rho}_3''|)\\ &+M_x(\boldsymbol{\rho}_s,\boldsymbol{\rho}_4'')\frac{y_o-L}{|\boldsymbol{\rho}_o-\boldsymbol{\rho}_4''|}H_1^{(2)}(k|\boldsymbol{\rho}_o-\boldsymbol{\rho}_4''|)\Bigg]dx''\end{aligned} \tag{5.3.3}$$

where $\boldsymbol{\rho}_n''$ denotes a point on the surface defined in (5.1.1). Using (5.1.9), M_x and M_y can be obtained as

$$M_y(\boldsymbol{\rho}_s,\boldsymbol{\rho}_n'') = (-1)^n E_z^s(\boldsymbol{\rho}_s,\boldsymbol{\rho}_n'') \qquad n=1,2 \tag{5.3.4}$$

$$M_x(\boldsymbol{\rho}_s,\boldsymbol{\rho}_n'') = (-1)^{(n-1)} E_z^s(\boldsymbol{\rho}_s,\boldsymbol{\rho}_n'') \qquad n=3,4 \tag{5.3.5}$$

where $E_z^s(\boldsymbol{\rho}_s,\boldsymbol{\rho}_n'')$ is the electric field on the surface of the dielectric slab generated by the exterior source. Using (5.2.2)-(5.2.5), $E_z^s(\boldsymbol{\rho}_s,\boldsymbol{\rho}_n'')$ becomes

$$E_z^s(\boldsymbol{\rho}_s,\boldsymbol{\rho}_n'') = E_{z2}^J(\boldsymbol{\rho}_s,\boldsymbol{\rho}_n'') + E_{z2}^M(\boldsymbol{\rho}_s,\boldsymbol{\rho}_n'') \tag{5.3.6}$$

and

$$\begin{aligned}E_{z2}^J(\boldsymbol{\rho}_s,\boldsymbol{\rho}_n'') = -\frac{\omega\mu_0}{4}I_s\int_{-L}^{L}&\Bigg[\frac{\partial G_{22}(\boldsymbol{\rho}',\boldsymbol{\rho})}{\partial x}\bigg|_{(\boldsymbol{\rho}_n'',\boldsymbol{\rho}_1')}H_0^{(2)}(k_1|\boldsymbol{\rho}_s-\boldsymbol{\rho}_1'|)\\ &-\frac{\partial G_{22}(\boldsymbol{\rho}',\boldsymbol{\rho})}{\partial x}\bigg|_{(\boldsymbol{\rho}_n'',\boldsymbol{\rho}_2')}H_0^{(2)}(k_1|\boldsymbol{\rho}_s-\boldsymbol{\rho}_2'|)\Bigg]dy'\\ -\frac{\omega\mu_0}{4}I_s\int_{0}^{2d}&\Bigg[\frac{\partial G_{22}(\boldsymbol{\rho}',\boldsymbol{\rho})}{\partial y}\bigg|_{(\boldsymbol{\rho}_n'',\boldsymbol{\rho}_3')}H_0^{(2)}(k_1|\boldsymbol{\rho}_s-\boldsymbol{\rho}_3'|)\\ &-\frac{\partial G_{22}(\boldsymbol{\rho}',\boldsymbol{\rho})}{\partial y}\bigg|_{(\boldsymbol{\rho}_n'',\boldsymbol{\rho}_4')}H_0^{(2)}(k_1|\boldsymbol{\rho}_s-\boldsymbol{\rho}_4'|)\Bigg]dx'.\end{aligned} \tag{5.3.7}$$

where $n = 1, 2, 3, 4$. Furthermore, using (5.2.5) $E_{z2}^{M}(\boldsymbol{\rho}_s, \boldsymbol{\rho}_n'')$ becomes

$$\begin{aligned} E_{z2}^{M}(\boldsymbol{\rho}_s, \boldsymbol{\rho}_n'') = {} & \frac{\omega\mu_0 k_1}{4} I_s \int_{-L}^{L} \left[G_{22}(\boldsymbol{\rho}'', \boldsymbol{\rho}_1') \frac{x_s}{|\boldsymbol{\rho}_s - \boldsymbol{\rho}_1'|} H_1^{(2)}(k_1 |\boldsymbol{\rho}_s - \boldsymbol{\rho}_1'|) \right. \\ & \left. - G_{22}(\boldsymbol{\rho}'', \boldsymbol{\rho}_2') \frac{x_s - 2d}{|\boldsymbol{\rho}_s - \boldsymbol{\rho}_2'|} H_1^{(2)}(k_1 |\boldsymbol{\rho}_s - \boldsymbol{\rho}_2'|) \right] dy' \\ & + \frac{\omega\mu_0 k_1}{4} I_s \int_{0}^{2d} \left[G_{22}(\boldsymbol{\rho}'', \boldsymbol{\rho}_3') \frac{y_s + L}{|\boldsymbol{\rho}_s - \boldsymbol{\rho}_3'|} H_1^{(2)}(k_1 |\boldsymbol{\rho}_s - \boldsymbol{\rho}_3'|) \right. \\ & \left. - G_{22}(\boldsymbol{\rho}'', \boldsymbol{\rho}_4') \frac{y_s - L}{|\boldsymbol{\rho}_s - \boldsymbol{\rho}_4'|} H_1^{(2)}(k_1 |\boldsymbol{\rho}_s - \boldsymbol{\rho}_4'|) \right] dx' \end{aligned} \tag{5.3.8}$$

The surface electric current $J_z(\boldsymbol{\rho}_s, \boldsymbol{\rho}_n'')$ in (5.3.2) can be obtained by using (5.1.11) as

$$J_z(\boldsymbol{\rho}_s, \boldsymbol{\rho}_n'') = \begin{cases} (-1)^n H_y^s(\boldsymbol{\rho}_s, \boldsymbol{\rho}_n'') & n = 1, 2 \\ (-1)^{(n-1)} H_x^s(\boldsymbol{\rho}_s, \boldsymbol{\rho}_n'') & n = 3, 4 \end{cases} \tag{5.3.9}$$

where $H_x^s(\boldsymbol{\rho}_s, \boldsymbol{\rho}_{3,4}'')$ and $H_y^s(\boldsymbol{\rho}_s, \boldsymbol{\rho}_{1,2}'')$ are the magnetic fields on the surface of the dielectric slab generated by the exterior source I_s. The magnetic field $H_x^s(\boldsymbol{\rho}_s, \boldsymbol{\rho}_{3,4}'')$ can be obtained by using (5.1.5) and (5.2.2)-(5.2.5) as

$$H_x^s(\boldsymbol{\rho}_s, \boldsymbol{\rho}_{3,4}'') = H_x^J(\boldsymbol{\rho}_s, \boldsymbol{\rho}_{3,4}'') + H_x^M(\boldsymbol{\rho}_s, \boldsymbol{\rho}_{3,4}'') \tag{5.3.10}$$

where

$$\begin{aligned} H_x^J(\boldsymbol{\rho}_s, \boldsymbol{\rho}_n'') = {} & -\frac{j}{4} I_s \int_{-L}^{L} \left[\left. \frac{\partial G_{22}(\boldsymbol{\rho}', \boldsymbol{\rho})}{\partial y' \partial x} \right|_{(\boldsymbol{\rho}_n'', \boldsymbol{\rho}_1')} H_0^{(2)}(k_1 |\boldsymbol{\rho}_s - \boldsymbol{\rho}_1'|) \right. \\ & \left. - \left. \frac{\partial G_{22}(\boldsymbol{\rho}', \boldsymbol{\rho})}{\partial y' \partial x} \right|_{(\boldsymbol{\rho}_n'', \boldsymbol{\rho}_2')} H_0^{(2)}(k_1 |\boldsymbol{\rho}_s - \boldsymbol{\rho}_2'|) \right] dy' \\ & - \frac{j}{4} I_s \int_{0}^{2d} \left[\left. \frac{\partial G_{22}(\boldsymbol{\rho}', \boldsymbol{\rho})}{\partial y' \partial y} \right|_{(\boldsymbol{\rho}_n'', \boldsymbol{\rho}_3')} H_0^{(2)}(k_1 |\boldsymbol{\rho}_s - \boldsymbol{\rho}_3'|) \right. \\ & \left. - \left. \frac{\partial G_{22}(\boldsymbol{\rho}', \boldsymbol{\rho})}{\partial y' \partial y} \right|_{(\boldsymbol{\rho}_n'', \boldsymbol{\rho}_4')} H_0^{(2)}(k_1 |\boldsymbol{\rho}_s - \boldsymbol{\rho}_4'|) \right] dx'. \end{aligned} \tag{5.3.11}$$

Using (5.1.5) and (5.2.5), $H_x^M(\boldsymbol{\rho}_s, \boldsymbol{\rho}_n'')$ becomes

$$\begin{aligned} H_x^M(\boldsymbol{\rho}_s, \boldsymbol{\rho}_n'') = -\frac{k_1}{4j} I_s \int_{-L}^{L} \Bigg[& \frac{\partial G_{22}(\boldsymbol{\rho}', \boldsymbol{\rho})}{\partial y'}\bigg|_{(\boldsymbol{\rho}_n'', \boldsymbol{\rho}_1')} H_1^{(2)}(k_1|\boldsymbol{\rho}_s - \boldsymbol{\rho}_1'|) \frac{x_s}{|\boldsymbol{\rho}_s - \boldsymbol{\rho}_1'|} \\ & - \frac{\partial G_{22}(\boldsymbol{\rho}', \boldsymbol{\rho})}{\partial y'}\bigg|_{(\boldsymbol{\rho}_n'', \boldsymbol{\rho}_2')} H_1^{(2)}(k_1|\boldsymbol{\rho}_s - \boldsymbol{\rho}_2'|) \frac{x_s - 2d}{|\boldsymbol{\rho}_s - \boldsymbol{\rho}_2'|} \Bigg] dy' \\ -\frac{k_1}{4j} I_s \int_{0}^{2d} \Bigg[& \frac{\partial G_{22}(\boldsymbol{\rho}', \boldsymbol{\rho})}{\partial y'}\bigg|_{(\boldsymbol{\rho}_n'', \boldsymbol{\rho}_3')} H_1^{(2)}(k_1|\boldsymbol{\rho}_s - \boldsymbol{\rho}_3'|) \frac{y_s + L}{|\boldsymbol{\rho}_s - \boldsymbol{\rho}_3'|} \\ & - \frac{\partial G_{22}(\boldsymbol{\rho}', \boldsymbol{\rho})}{\partial y'}\bigg|_{(\boldsymbol{\rho}_n'', \boldsymbol{\rho}_4')} H_1^{(2)}(k_1|\boldsymbol{\rho}_s - \boldsymbol{\rho}_4'|) \frac{y_s - L}{|\boldsymbol{\rho}_s - \boldsymbol{\rho}_4'|} \Bigg] dx' \end{aligned} \tag{5.3.12}$$

where $n = 3, 4$ in (5.3.11) and (5.3.12). The magnetic field on the surface of the dielectric $H_y^s(\boldsymbol{\rho}_s, \boldsymbol{\rho}_{1,2}'')$ can be obtained by using (5.1.6) and (5.2.2)-(5.2.5) as

$$H_y(\boldsymbol{\rho}_s, \boldsymbol{\rho}_{1,2}'') = H_y^J(\boldsymbol{\rho}_s, \boldsymbol{\rho}_{1,2}'') + H_y^M(\boldsymbol{\rho}_s, \boldsymbol{\rho}_{1,2}'') \tag{5.3.13}$$

where

$$\begin{aligned} H_y^J(\boldsymbol{\rho}_s, \boldsymbol{\rho}_n'') = \frac{j}{4} I_s \int_{-L}^{L} \Bigg[& \frac{\partial G_{22}(\boldsymbol{\rho}', \boldsymbol{\rho})}{\partial x' \partial x}\bigg|_{(\boldsymbol{\rho}_n'', \boldsymbol{\rho}_1')} H_0^{(2)}(k_1|\boldsymbol{\rho}_s - \boldsymbol{\rho}_1'|) \\ & - \frac{\partial G_{22}(\boldsymbol{\rho}', \boldsymbol{\rho})}{\partial x' \partial x}\bigg|_{(\boldsymbol{\rho}_n'', \boldsymbol{\rho}_2')} H_0^{(2)}(k_1|\boldsymbol{\rho}_s - \boldsymbol{\rho}_2'|) \Bigg] dy' \\ +\frac{j}{4} I_s \int_{0}^{2d} \Bigg[& \frac{\partial G_{22}(\boldsymbol{\rho}', \boldsymbol{\rho})}{\partial x' \partial y}\bigg|_{(\boldsymbol{\rho}_n'', \boldsymbol{\rho}_3')} H_0^{(2)}(k_1|\boldsymbol{\rho}_s - \boldsymbol{\rho}_3'|) \\ & - \frac{\partial G_{22}(\boldsymbol{\rho}', \boldsymbol{\rho})}{\partial x' \partial y}\bigg|_{(\boldsymbol{\rho}_n'', \boldsymbol{\rho}_4')} H_0^{(2)}(k_1|\boldsymbol{\rho}_s - \boldsymbol{\rho}_4'|) \Bigg] dx'. \end{aligned} \tag{5.3.14}$$

Using (5.1.6) and (5.2.5), H_y^M can be written as

$$
\begin{aligned}
H_y^M(\boldsymbol{\rho}_s, \boldsymbol{\rho}_n'') = \frac{k_1}{4j} \int_{-L}^{L} \Bigg[& \left.\frac{\partial G_{22}(\boldsymbol{\rho}', \boldsymbol{\rho})}{\partial x'}\right|_{(\boldsymbol{\rho}_n'', \boldsymbol{\rho}_1')} H_1^{(2)}(k_1|\boldsymbol{\rho}_s - \boldsymbol{\rho}_1'|) \frac{x_s}{|\boldsymbol{\rho}_s - \boldsymbol{\rho}_1'|} \\
& - \left.\frac{\partial G_{22}(\boldsymbol{\rho}', \boldsymbol{\rho})}{\partial x'}\right|_{(\boldsymbol{\rho}_n'', \boldsymbol{\rho}_2')} H_1^{(2)}(k_1|\boldsymbol{\rho}_s - \boldsymbol{\rho}_2'|) \frac{x_s - 2d}{|\boldsymbol{\rho}_s - \boldsymbol{\rho}_2'|} \Bigg] dy' \\
+ \frac{k_1}{4j} \int_{0}^{2d} \Bigg[& \left.\frac{\partial G_{22}(\boldsymbol{\rho}', \boldsymbol{\rho})}{\partial x'}\right|_{(\boldsymbol{\rho}_n'', \boldsymbol{\rho}_3')} H_1^{(2)}(k_1|\boldsymbol{\rho}_s - \boldsymbol{\rho}_3'|) \frac{y_s + L}{|\boldsymbol{\rho}_s - \boldsymbol{\rho}_3'|} \\
& - \left.\frac{\partial G_{22}(\boldsymbol{\rho}', \boldsymbol{\rho})}{\partial x'}\right|_{(\boldsymbol{\rho}_n'', \boldsymbol{\rho}_4')} H_1^{(2)}(k_1|\boldsymbol{\rho}_s - \boldsymbol{\rho}_4'|) \frac{y_s - L}{|\boldsymbol{\rho}_s - \boldsymbol{\rho}_4'|} \Bigg] dx'
\end{aligned}
\tag{5.3.15}
$$

where $n = 1, 2$ in (5.3.14) and (5.3.15).

In summary, the exterior electric field at the observation point $\boldsymbol{\rho}_o = x_o\hat{\boldsymbol{x}} + y_o\hat{\boldsymbol{y}}$, which is generated by the exterior source at $\boldsymbol{\rho}_s = x_s\hat{\boldsymbol{x}} + y_s\hat{\boldsymbol{y}}$, can be obtained by (5.3.1) with E_z^J and E_z^M given in (5.3.2)-(5.3.3) and using (5.3.4)-(5.3.15).

The solution presented in this section requires the numerical integration of the double integral on the surface of the dielectric slab, which will be discussed in the next section.

5.4 Numerical Integration

In the previous sections of this chapter, the electric field was presented in terms of the interior Green's function where the numerical integration was required. In this section, the numerical integration will be presented. In doing so, the height and the width of the dielectric slab is divided into $2p$ and 2ℓ cells, respectively. Fig. 5.4 shows the surface segmentation of a finite dielectric slab. The slab has a thickness of $2d$ and height of $2L$. The total number of cells on the slab surface is $4t$ where

$$t = p + \ell. \tag{5.4.1}$$

The cell sizes in the x and y direction are denoted by δ_x and δ_y where typically

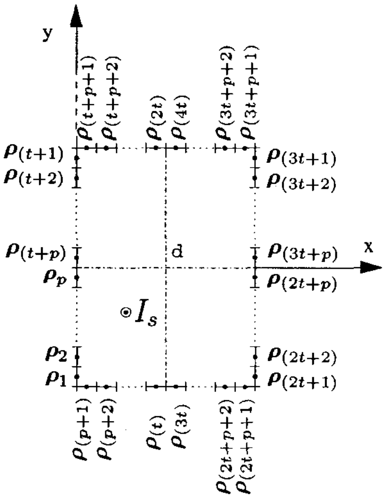

Figure 5.4: The dielectric slab surface divided into $4p + 4\ell$ cells.

$\delta_{x,y} < 0.1\lambda_2$, and λ_2 is the wavelength inside the dielectric slab. The center of the n'th cell is denoted by

$$\boldsymbol{\rho}_n = x_n \hat{\boldsymbol{x}} + y_n \hat{\boldsymbol{y}} \tag{5.4.2}$$

where

$$x_n = \begin{cases} 0 & 1 \leq n \leq p \\ (n - p - 1/2)\delta_x & p + 1 \leq n \leq t \end{cases} \tag{5.4.3}$$

$$y_n = \begin{cases} -L + (n - 1/2)\delta_y & 1 \leq n \leq p \\ -L & p + 1 \leq n \leq t. \end{cases} \tag{5.4.4}$$

By applying the symmetrical properties of the slab with respect to $x = d$ and/or $y = 0$, the center of the n'th cells for $t < n$ can be expressed as

$$\boldsymbol{\rho}_n = \begin{cases} x_{(n-t)}\hat{\boldsymbol{x}} - y_{(n-t)}\hat{\boldsymbol{y}} & t+1 \leq n \leq 2t \\ [2d - x_{(n-2t)}]\hat{\boldsymbol{x}} + y_{(n-2t)}\hat{\boldsymbol{y}} & 2t+1 \leq n \leq 3t \\ [2d - x_{(n-3t)}]\hat{\boldsymbol{x}} - y_{(n-3t)}\hat{\boldsymbol{y}} & 3t+1 \leq n \leq 4t \end{cases} \tag{5.4.5}$$

Since the cell size is chosen small enough compared to the wavelength, the equivalent surface currents can be assumed to be constant on each cell, and the equivalent currents density can be approximated as

$$J_z(\boldsymbol{\rho}_t) = \sum_{n=1}^{4t} I_n P_n(\boldsymbol{\rho}_t) \tag{5.4.6}$$

$$M_t(\boldsymbol{\rho}_t) = \sum_{n=1}^{4t} K_n P_n(\boldsymbol{\rho}_t) \tag{5.4.7}$$

where $\boldsymbol{\rho}_t$ denotes the position on the slab contour, and

$$P_n(\boldsymbol{\rho}_t) = \begin{cases} 1 & \text{on } n'\text{th cell} \\ 0 & \text{otherwise.} \end{cases} \tag{5.4.8}$$

defines the pulse function. In order to express (5.1.13) and (5.1.14) in a simple form, the asymptotic expression for the Hankel function of the second kind can be used. The asymptotic expression is

$$H_q^{(2)}(x) = \sqrt{\frac{2}{\pi x}} e^{-j(x-q(\pi/2)-\pi/4)} \tag{5.4.9}$$

where q denotes the order of the Hankel function. Using (5.4.6) and (5.4.9), we can write (5.1.13) as

$$E_z^J = -w\mu_0 \sum_{n=1}^{4t} I_n \frac{e^{-j(k|\boldsymbol{\rho}_o - \boldsymbol{\rho}_n| - \pi/4)}}{\sqrt{8\pi k|\boldsymbol{\rho}_o - \boldsymbol{\rho}_n|}} \delta_n \text{sinc}[k\cos(\phi_n)\delta_n/2)] \tag{5.4.10}$$

where

$$\delta_n = \begin{cases} \delta_y & it+1 \leq n \leq it+p \\ \delta_x & it+p+1 \leq n \leq (i+1)t \end{cases} \tag{5.4.11}$$

for $i = 0, 1, 2, 3$, and

$$\cos(\phi_n) = \begin{cases} (y_o - y_n)/|\boldsymbol{\rho}_o - \boldsymbol{\rho}_n| & it+1 \leq n \leq it+p \\ (x_o - x_n)/|\boldsymbol{\rho}_o - \boldsymbol{\rho}_n| & it+p+1 \leq n \leq (i+1)t. \end{cases} \tag{5.4.12}$$

The sinc function is defined as $\text{sinc}(x) = \sin(x)/x$. Similarly, we can use (5.4.7) and (5.4.9) to write (5.1.14) as

$$E_z^M = -jk \sum_{n=1}^{4t} K_n(|\hat{\boldsymbol{n}}_n \cdot \hat{\boldsymbol{x}}| - |\hat{\boldsymbol{n}}_n \cdot \hat{\boldsymbol{y}}|) \frac{e^{-j(k|\boldsymbol{\rho}_o - \boldsymbol{\rho}_n| - 3\pi/4)}}{\sqrt{8\pi k|\boldsymbol{\rho}_o - \boldsymbol{\rho}_n|}} \delta_n \sin\phi_n \text{sinc}[k\cos(\phi_n)\delta_n/2)] \tag{5.4.13}$$

where

$$\sin(\phi_n) = \begin{cases} (x_o - x_n)/|\boldsymbol{\rho}_o - \boldsymbol{\rho}_n| & it+1 \leq n \leq it+p \\ (y_o - y_n)/|\boldsymbol{\rho}_o - \boldsymbol{\rho}_n| & it+p+1 \leq n \leq (i+1)t. \end{cases} \tag{5.4.14}$$

The unit vector $\hat{\boldsymbol{n}}_n$ is normal to the n'th cell and it points out toward the exterior region. As a result, we can write the Green's function G_{12} which gives the exterior field generated by a line source inside the dielectric slab. Using (3.1.5), (5.1.17), (5.4.10) and (5.4.13), the Green's function G_{12} can be expressed as

$$\begin{aligned} G_{12}(\boldsymbol{\rho}_s, \boldsymbol{\rho}_o) = -j \sum_{n=1}^{4t} \Bigg[\bigg(I_n - K_n(|\hat{\boldsymbol{n}}_n \cdot \hat{\boldsymbol{x}}| - |\hat{\boldsymbol{n}}_n \cdot \hat{\boldsymbol{y}}|) \frac{\sin\phi_n}{\eta} \bigg) \\ \cdot \frac{e^{-j(k|\boldsymbol{\rho}_o - \boldsymbol{\rho}_n| - \pi/4)}}{\sqrt{8\pi k|\boldsymbol{\rho}_o - \boldsymbol{\rho}_n|}} \delta_n \mathrm{sinc}[k\cos(\phi_n)\delta_n/2)] \Bigg] \end{aligned} \tag{5.4.15}$$

where

$$I_n = \begin{cases} \nu_n \dfrac{\partial G_{22}(\boldsymbol{\rho}', \boldsymbol{\rho})}{\partial x} \bigg|_{(\boldsymbol{\rho}_s, \boldsymbol{\rho}_n)} & it + 1 \le n \le it + p \\ \nu_n \dfrac{\partial G_{22}(\boldsymbol{\rho}', \boldsymbol{\rho})}{\partial y} \bigg|_{(\boldsymbol{\rho}_s, \boldsymbol{\rho}_n)} & it + p + 1 \le n \le (i+1)t \end{cases} \tag{5.4.16}$$

$$K_n = j\nu_n' \omega \mu_0 G_{22}(\boldsymbol{\rho}_n, \boldsymbol{\rho}_s) \tag{5.4.17}$$

and

$$\nu_n = -\hat{\boldsymbol{n}}_n \cdot (\hat{\boldsymbol{x}} + \hat{\boldsymbol{y}}). \tag{5.4.18}$$

$$\nu_n' = -\hat{\boldsymbol{n}}_n \cdot (\hat{\boldsymbol{x}} - \hat{\boldsymbol{y}}). \tag{5.4.19}$$

The result in (5.4.15) is also expressible in matrix form as

$$\begin{aligned} G_{12}(\boldsymbol{\rho}_s, \boldsymbol{\rho}_o) &= \sum_{n=1}^{4t} [I_n(\boldsymbol{\rho}_s) P_n(\boldsymbol{\rho}_o) + K_n(\boldsymbol{\rho}_s) Q_n(\boldsymbol{\rho}_o)] \\ &= \boldsymbol{I}_e \boldsymbol{P}_o + \boldsymbol{K}_e \boldsymbol{Q}_o \end{aligned} \tag{5.4.20}$$

where I_n and K_n are elements of the row vectors $\boldsymbol{I}_e$ and $\boldsymbol{K}_e$, respectively. Furthermore, $P_n(\boldsymbol{\rho}_o)$ and $Q_n(\boldsymbol{\rho}_o)$ which are the elements of the column vectors $\boldsymbol{P}_o$ and $\boldsymbol{Q}_o$

can be written as

$$P_n(\boldsymbol{\rho}_o) = -j\frac{e^{-j(k|\boldsymbol{\rho}_o-\boldsymbol{\rho}_n|-\pi/4)}}{\sqrt{8\pi k|\boldsymbol{\rho}_o-\boldsymbol{\rho}_n|}}\delta_n \mathrm{sinc}[k\cos(\phi_n)\delta_n/2)] \tag{5.4.21}$$

$$Q_n(\boldsymbol{\rho}_o) = -\left(|\hat{\boldsymbol{n}}_n\cdot\hat{\boldsymbol{x}}| - |\hat{\boldsymbol{n}}_n\cdot\hat{\boldsymbol{y}}|\right)\frac{\sin\phi_n}{\eta}P_n. \tag{5.4.22}$$

It is noted that in (5.4.16) and (5.4.17), we compute G_{22} and its derivative at $\boldsymbol{\rho}_n$ which is the center of the n'th cell. This is a good approximation if the source position is not close to the n'th cell and the cells are small. To improve accuracy when $|\boldsymbol{\rho}_s-\boldsymbol{\rho}_n| \leq \lambda_2$, we calculate the mean value of I_n and K_n on the n'th cell. In doing so, (5.4.16) and (5.4.17) become

$$I_n = \begin{cases} \nu_n/\delta_y \displaystyle\int_{\boldsymbol{\rho}_n-\frac{\delta_y}{2}\hat{\boldsymbol{y}}}^{\boldsymbol{\rho}_n+\frac{\delta_y}{2}\hat{\boldsymbol{y}}} \left.\frac{\partial G_{22}(\boldsymbol{\rho}',\boldsymbol{\rho})}{\partial x}\right|_{(\boldsymbol{\rho}_s,\boldsymbol{\rho})} dy & it+1 \leq n \leq it+p \\ \\ \nu_n/\delta_x \displaystyle\int_{\boldsymbol{\rho}_n-\frac{\delta_x}{2}\hat{\boldsymbol{x}}}^{\boldsymbol{\rho}_n+\frac{\delta_x}{2}\hat{\boldsymbol{x}}} \left.\frac{\partial G_{22}(\boldsymbol{\rho}',\boldsymbol{\rho})}{\partial y}\right|_{(\boldsymbol{\rho}_s,\boldsymbol{\rho})} dx & it+p+1 \leq n \leq (i+1)t \end{cases} \tag{5.4.23}$$

$$K_n = j\nu_n'\omega\mu_0 \begin{cases} \displaystyle\int_{\boldsymbol{\rho}_n-\frac{\delta_y}{2}\hat{\boldsymbol{y}}}^{\boldsymbol{\rho}_n+\frac{\delta_y}{2}\hat{\boldsymbol{y}}} \frac{G_{22}(\boldsymbol{\rho}_s,\boldsymbol{\rho})}{\delta_y} dy & it+1 \leq n \leq it+p \\ \\ \displaystyle\int_{\boldsymbol{\rho}_n-\frac{\delta_x}{2}\hat{\boldsymbol{x}}}^{\boldsymbol{\rho}_n+\frac{\delta_x}{2}\hat{\boldsymbol{x}}} \frac{G_{22}(\boldsymbol{\rho}_s,\boldsymbol{\rho})}{\delta_x} dx & it+p+1 \leq n \leq (i+1)t \end{cases} . \tag{5.4.24}$$

When the source is at the center of the n'th cell, I_n and K_n become singular. Evaluating the mean value of I_n and K_n is sometimes referred to as "self term evaluation." The self terms are evaluated by extracting the singular term from G_{22} as given in (A.8-12)-(A.8-14). The singular term is the free space Green's function G_f and its derivative. For more on self term evaluation, the reader is referred to Appendix A.8.

The interior field generated by an exterior line source is denoted by G_{21} and can be obtained by applying the reciprocity theorem as

$$G_{21}(\boldsymbol{\rho}_s, \boldsymbol{\rho}_o) = G_{12}(\boldsymbol{\rho}_o, \boldsymbol{\rho}_s). \tag{5.4.25}$$

where G_{21} is given in (5.4.15). This means that the source and the field point positions should be interchanged in order to use G_{12} for computing G_{21}.

To obtain the exterior field generated by an exterior line source which is denoted by G_{11}, we apply the equivalence principle to the exterior region. As a result, the total exterior field can be expressed in terms of incident and scattered field as

$$G_{11} = G_f + G_s \tag{5.4.26}$$

where the incident field is denoted by G_f which is the free space Green's function and is given in (A.5-7). To calculate the scattered field G_s, we should find the surface equivalent currents. Using G_{21}, we can obtain the total electric and magnetic fields on the surface of the slab. Having the total electric and magnetic fields, we can calculate the surface equivalent currents. According to the surface equivalence principle, the surface currents give the scattered field similar to (5.4.20) as

$$\begin{aligned} G_s(\boldsymbol{\rho}_s, \boldsymbol{\rho}_o) =& \sum_{n=1}^{4t} \left[I_n^s(\boldsymbol{\rho}_s) P_n(\boldsymbol{\rho}_o) + K_n^s(\boldsymbol{\rho}_s) Q_n(\boldsymbol{\rho}_o) \right] \\ =& \boldsymbol{I}_s \boldsymbol{P}_o + \boldsymbol{K}_s \boldsymbol{Q}_o \end{aligned} \tag{5.4.27}$$

where I_n^s and K_n^s are the elements of the row vector $\boldsymbol{I}_s$ and $\boldsymbol{K}_s$, respectively. Since

I_n^s and K_n^s are the equivalent currents on the n'th cell, they can be expressed as

$$I_n^s(\boldsymbol{\rho}_s) = \begin{cases} \nu_n \dfrac{\partial G_{12}(\boldsymbol{\rho}',\boldsymbol{\rho})}{\partial x'}\Bigg|_{(\boldsymbol{\rho}_n,\boldsymbol{\rho}_s)} & it+1 \le n \le it+p \\ \nu_n \dfrac{\partial G_{12}(\boldsymbol{\rho}',\boldsymbol{\rho})}{\partial y'}\Bigg|_{(\boldsymbol{\rho}_n,\boldsymbol{\rho}_s)} & it+p+1 \le n \le (i+1)t \end{cases} \tag{5.4.28}$$

$$K_n^s(\boldsymbol{\rho}_s) = j\nu_n' \omega \mu_0 G_{12}(\boldsymbol{\rho}_n, \boldsymbol{\rho}_s). \tag{5.4.29}$$

To use the symmetrical properties of the slab, we define the source and field point images with respect to the slab's symmetrical planes $x = d$ and $y = 0$ as

$$\boldsymbol{\rho}_{s,o}^{(0)} = x_{s,o}\hat{\boldsymbol{x}} + y_{s,o}\hat{\boldsymbol{y}} \tag{5.4.30}$$

$$\boldsymbol{\rho}_{s,o}^{(1)} = x_{s,o}\hat{\boldsymbol{x}} - y_{s,o}\hat{\boldsymbol{y}} \tag{5.4.31}$$

$$\boldsymbol{\rho}_{s,o}^{(2)} = (2d - x_{s,o})\hat{\boldsymbol{x}} + y_{s,o}\hat{\boldsymbol{y}} \tag{5.4.32}$$

$$\boldsymbol{\rho}_{s,o}^{(3)} = (2d - x_{s,o})\hat{\boldsymbol{x}} - y_{s,o}\hat{\boldsymbol{y}} \tag{5.4.33}$$

where $\boldsymbol{\rho}_s^{(0)}$ and $\boldsymbol{\rho}_o^{(0)}$ define the source and field points, respectively. By using the symmetrical property of the slab with respect to the plane $y = 0$, the equivalent electric current on the $(t+1)'$th cell generated by a line source $I_s(\boldsymbol{\rho}_s)$ is equivalent to the electric current on the first cell generated by the image source $I_s(\boldsymbol{\rho}_s^{(1)})$. Using other symmetrical properties of the slab, we can write

$$I_n^s(\boldsymbol{\rho}_s) = I_{(n-it)}^s(\boldsymbol{\rho}_s^{(i)}) \qquad it+1 \le n \le (i+1)t \tag{5.4.34}$$

$$K_n^s(\boldsymbol{\rho}_s) = \nu_n K_{(n-it)}^s(\boldsymbol{\rho}_s^{(i)}) \qquad it+1 \le n \le (i+1)t \tag{5.4.35}$$

where $i = 0, 1, 2, 3$. Furthermore, we can use the symmetrical properties of the slab for calculating the field point as

$$P_n(\boldsymbol{\rho}_o) = P_{(n-it)}(\boldsymbol{\rho}_o^{(i)}) \qquad it+1 \le n \le (i+1)t \tag{5.4.36}$$

$$Q_n(\boldsymbol{\rho}_o) = \nu_n Q_{(n-it)}(\boldsymbol{\rho}_o^{(i)}) \qquad it+1 \le n \le (i+1)t. \tag{5.4.37}$$

Using the symmetrical properties of the slab given in (5.4.34)-(5.4.37), we can write (5.4.27) as

$$G_s(\boldsymbol{\rho}_s, \boldsymbol{\rho}_o) = \sum_{i=0}^{3}\sum_{n=1}^{t} \left[I_n^s(\boldsymbol{\rho}_s^{(i)}) P_n(\boldsymbol{\rho}_o^{(i)}) + K_n^s(\boldsymbol{\rho}_s^{(i)}) Q_n(\boldsymbol{\rho}_o^{(i)}) \right]. \tag{5.4.38}$$

It is noted that $I_n^s(\boldsymbol{\rho}_s^{(i)})$ and $K_n^s(\boldsymbol{\rho}_s^{(i)})$ can be written using (5.4.28)-(5.4.29) and (5.4.20) as

$$I_n^s(\boldsymbol{\rho}_s^{(i)}) = \sum_{m=1}^{4t} \left[P_m(\boldsymbol{\rho}_s^{(i)}) I_{mn}^I + Q_m(\boldsymbol{\rho}_s^{(i)}) K_{mn}^I \right] \tag{5.4.39}$$

$$K_n^s(\boldsymbol{\rho}_s^{(i)}) = \sum_{m=1}^{4t} \left[P_m(\boldsymbol{\rho}_s^{(i)}) I_{mn}^K + Q_m(\boldsymbol{\rho}_s^{(i)}) K_{mn}^K \right] \tag{5.4.40}$$

where

$$K_{mn}^I = \begin{cases} j\nu_m' \omega\mu \left. \frac{\partial G_{22}(\boldsymbol{\rho}',\boldsymbol{\rho})}{\partial x'} \right|_{(\boldsymbol{\rho}_n,\boldsymbol{\rho}_m)} & 1 \le n \le p \\ j\nu_m' \omega\mu \left. \frac{\partial G_{22}(\boldsymbol{\rho}',\boldsymbol{\rho})}{\partial y'} \right|_{(\boldsymbol{\rho}_n,\boldsymbol{\rho}_m)} & p+1 \le n \le t \end{cases} \tag{5.4.41}$$

$$I_{mn}^K = \begin{cases} j\nu_n' \nu_m \omega\mu \left. \frac{\partial G_{22}(\boldsymbol{\rho}',\boldsymbol{\rho})}{\partial x} \right|_{(\boldsymbol{\rho}_n,\boldsymbol{\rho}_m)} & it+1 \le m \le it+p \\ j\nu_n' \nu_m \omega\mu \left. \frac{\partial G_{22}(\boldsymbol{\rho}',\boldsymbol{\rho})}{\partial y} \right|_{(\boldsymbol{\rho}_n,\boldsymbol{\rho}_m)} & it+p+1 \le m \le (i+1)t \end{cases} \tag{5.4.42}$$

$$K_{mn}^K = -\nu_n' \nu_m \omega^2 \mu^2 G_{22}(\boldsymbol{\rho}_n, \boldsymbol{\rho}_m). \tag{5.4.43}$$

Furthermore, I^I_{mn} can be expressed for $1 \le n \le p$ as

$$I^I_{mn} = \begin{cases} \nu_m \left.\dfrac{\partial^2 G_{22}(\boldsymbol{\rho}',\boldsymbol{\rho})}{\partial x' \partial x}\right|_{(\boldsymbol{\rho}_n,\boldsymbol{\rho}_m)} & it+1 \le m \le it+p \\ \nu_m \left.\dfrac{\partial^2 G_{22}(\boldsymbol{\rho}',\boldsymbol{\rho})}{\partial x' \partial y}\right|_{(\boldsymbol{\rho}_n,\boldsymbol{\rho}_m)} & it+p+1 \le m \le (i+1)p \end{cases} \tag{5.4.44}$$

and

$$I^I_{mn} = \begin{cases} \nu_m \left.\dfrac{\partial^2 G_{22}(\boldsymbol{\rho}',\boldsymbol{\rho})}{\partial y' \partial x}\right|_{(\boldsymbol{\rho}_n,\boldsymbol{\rho}_m)} & it+1 \le m \le it+p \\ \nu_m \left.\dfrac{\partial^2 G_{22}(\boldsymbol{\rho}',\boldsymbol{\rho})}{\partial y' \partial y}\right|_{(\boldsymbol{\rho}_n,\boldsymbol{\rho}_m)} & it+p+1 \le m \le (i+1)p \end{cases} \tag{5.4.45}$$

when $1+p \le n \le t$. Similar to (5.4.20), it is useful to represent the result in (5.4.38) in matrix form as

$$G_s(\boldsymbol{\rho}_s,\boldsymbol{\rho}_o) = \sum_{i=0}^{3} \left[(\boldsymbol{P}^{(i)}_s \boldsymbol{I}^I + \boldsymbol{Q}^{(i)}_s \boldsymbol{K}^I)\boldsymbol{P}^{(i)}_o + (\boldsymbol{P}^{(i)}_s \boldsymbol{I}^K + \boldsymbol{Q}^{(i)}_s \boldsymbol{K}^K)\boldsymbol{Q}^{(i)}_o \right] \tag{5.4.46}$$

where $\boldsymbol{I}^I$, $\boldsymbol{K}^I$, $\boldsymbol{I}^K$ and $\boldsymbol{K}^K$ are $4t \times t$ matrices with elements I^I_{mn}, K^I_{mn}, I^K_{mn} and K^K_{mn}, respectively. Using (5.4.21) and (5.4.22), the elements of the column vectors $\boldsymbol{P}^{(i)}_o$ and $\boldsymbol{Q}^{(i)}_o$ are $P_n(\boldsymbol{\rho}^{(i)}_o)$ and $Q_n(\boldsymbol{\rho}^{(i)}_o)$ given in (5.4.36) and (5.4.37), respectively. The elements of the row vectors $\boldsymbol{P}^{(i)}_s$ and $\boldsymbol{Q}^{(i)}_s$, which are $P_m(\boldsymbol{\rho}^{(i)}_s)$ and $Q_m(\boldsymbol{\rho}^{(i)}_s)$, can also be obtained from (5.4.21) and (5.4.22).

It is noted that the geometrical symmetry of the dielectric slab is used in the formulation to reduce the elements of $\boldsymbol{I}^I$, $\boldsymbol{K}^I$, $\boldsymbol{I}^K$ and $\boldsymbol{K}^K$ which are the most time consuming part of the computation in the numerical approach. Once $\boldsymbol{I}^I$, $\boldsymbol{K}^I$, $\boldsymbol{I}^K$ and $\boldsymbol{K}^K$ are computed, the electric field for any arbitrary source and observation point can be obtained.

To improve accuracy in calculating (5.4.41)-(5.4.45) when $(\boldsymbol{\rho}_n - \boldsymbol{\rho}_m) \le \lambda_2$, we calculate the mean value for the near-neighbor terms similar to (5.4.23) and (5.4.24) (λ_2 is the wave length inside the dielectric slab). We should also evaluate the mean value for the diagonal elements of $\boldsymbol{I}^I$, $\boldsymbol{K}^I$, $\boldsymbol{I}^K$ and $\boldsymbol{K}^K$, referred to as self-term evaluation when $\boldsymbol{\rho}_n = \boldsymbol{\rho}_m$. The self-term evaluation is discussed in Appendix A.8.

5.5 Results and Discussion

The computer code implementing the numerical procedure explained in the previous section has been tested here. The results are compared with the results generated by a SIE/MoM code. The reader is referred to Subsection 6.1.2 for more details on the SIE/MoM formulations.

Referring to Fig. 5.1, the dielectric slab has a height $2L = 0.5$ m and thickness $2d = 0.2$ m. We choose a frequency $f = 1.8$ GHz. The relative permittivity and conductivity of the slab are $\epsilon_r = 6$ and $\sigma = 0.195$ mS/m, respectively. The exterior medium is free space, $\epsilon_1 = \epsilon_0$. The source strength is normalized so that it generates 1 V/m at a distance of 1 m in free space, and 0 dB corresponds to 1 V/m.

First, we study the case where the exterior field is generated by an interior line source.

Fig. 5.5 shows the electric surface current distribution on the dielectric slab with respect to the parametric variable t which represent the surface position in a clockwise direction, and $t = 0$ corresponds to $(x, y) = (-L/2, 0)$. The source is at $(x_s, y_s) = (0.1, 0)$ m. Similarly, the magnetic surface current distribution is shown in Fig. 5.6 where the magnetic surface current is assumed to be in a clockwise direction. The magnitude and phase of the electric and magnetic surface currents are obtained using the GF and SIE/MoM approaches. All the GF results are in a very good agreement with the results obtained using SIE/MoM.

The exterior electric field can be obtained using the G_{12} formulation given in (5.4.15)-(5.4.17). Fig. 5.7 shows the exterior electric field at $(x_o, y_o) = (-1, y)$ m. The result computed by the GF and SIE/MoM agree very well. To observe the effect

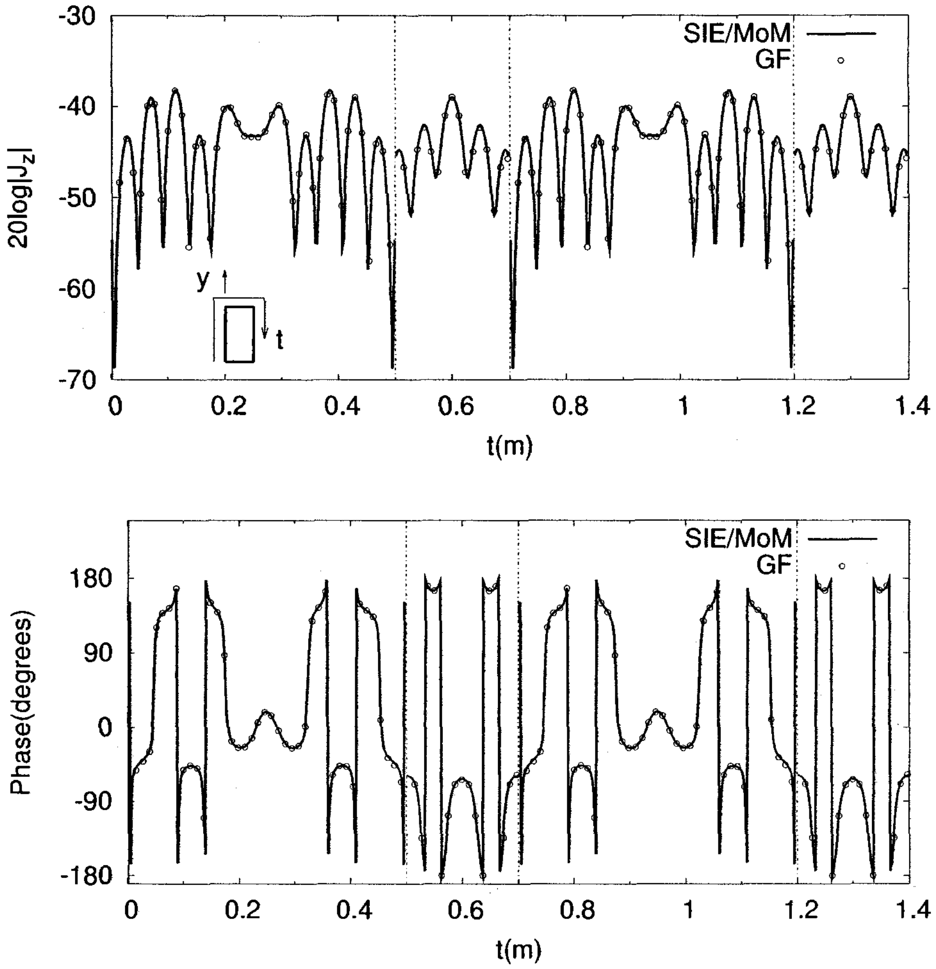

Figure 5.5: The magnitude and phase of the equivalent electric current on the surface of the slab when the line source is in the interior region. Source is at $(x_s, y_s) = (0.1, 0)$ m. The slab has a thickness of $2d = 0.2$ m and height of $2L = 0.5$ m.

of the finiteness of the slab on the exterior field, the result is also compared with the infinite slab solution. It is noted that in this case, the source is not very close to the end cap.

We can now consider a case when the source is closer to the end cap. Fig. 5.8 shows the exterior electric field generated by a line source at $(x_s, y_s) = (0.01, 0.24)$ m. The field point is at $(x_o, y_o) = (-3, y)$ m. The finite and infinite slab solution are compared. Since the source is close to the end cap, the exterior field is highly affected

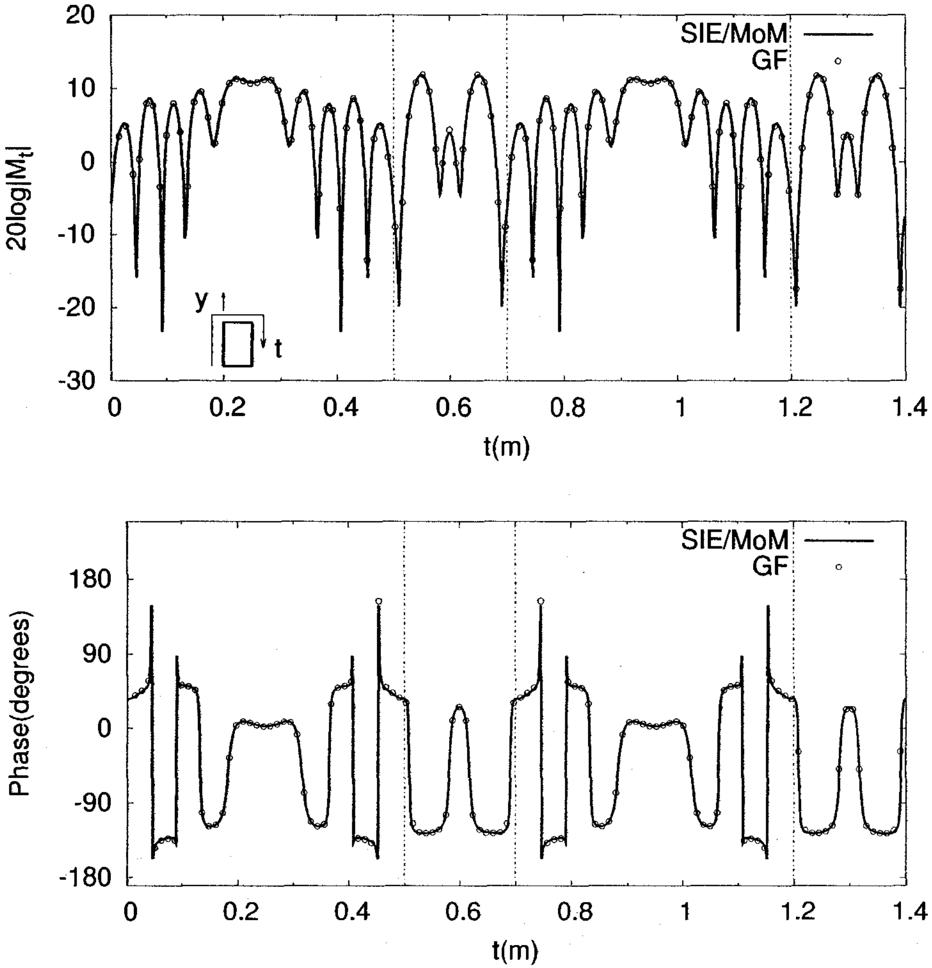

Figure 5.6: The magnitude and phase of the equivalent magnetic current on the surface of the slab when the line source is in the interior region. Source is at $(x_s, y_s) = (0.1, 0)$ m. The slab has a thickness of $2d = 0.2$ m and height of $2L = 0.5$ m.

by the end cap.

It is expected that by increasing the slab length, the GF result should converge to the infinite slab. This is first verified in Fig. 5.9a. The infinite slab solution is compared with GF-FS when $2L = 5$ m and $2L = 15$ m. We keep the source and field point positions unchanged. It is observed that the end cap diffraction becomes smaller when $2L = 15$ m. This happens since the end cap is much further away from the field point when we increase the slab length. In addition, the surface wave

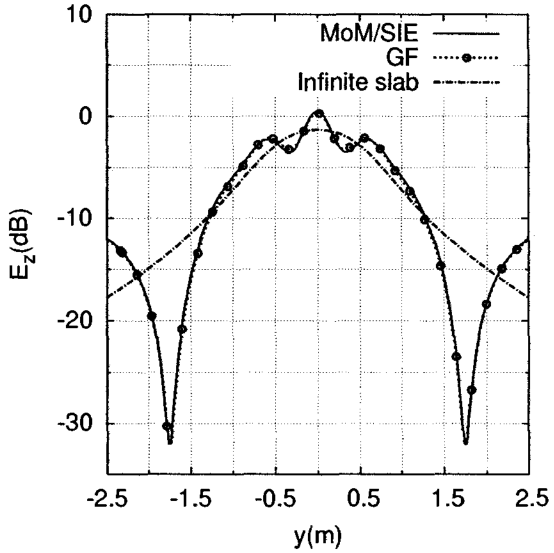

Figure 5.7: The comparison of the exterior electric field generated by a line source inside the finite and infinite slab. Source is at $(x_s, y_s) = (0.1, 0.)$ m, and the field point is at $(x_o, y_o) = (-1, y)$ m.

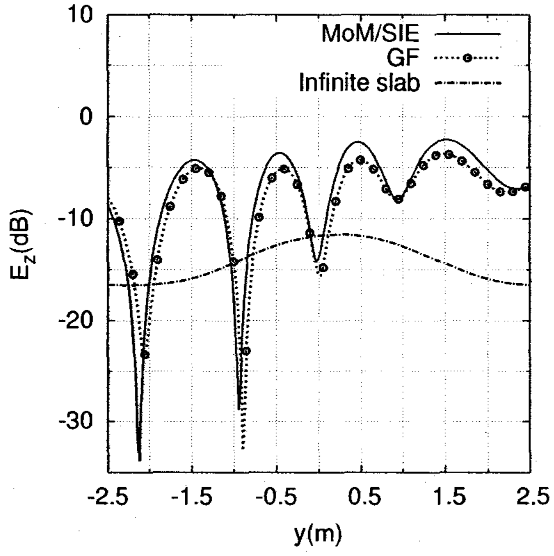

Figure 5.8: The exterior electric field generated by a line source inside the finite and infinite slab. Source is at $(x_s, y_s) = (0.01, 0.24)$ m, and the field point is at $(x_o, y_o) = (-3, y)$ m.

generated by the source decays before reaching the end cap since the slab is lossy. The effect of the slab loss on the exterior field can be observed by increasing the slab

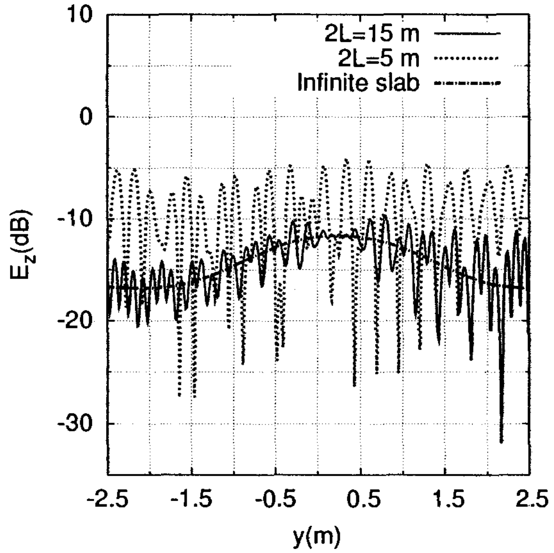

(a)

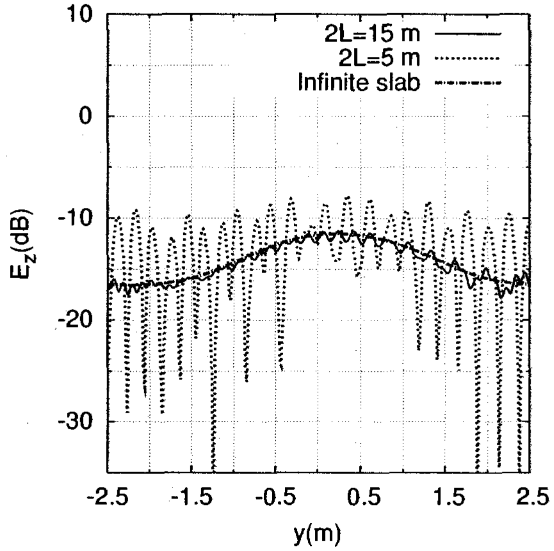

(b)

Figure 5.9: The effect of increasing the slab height in the exterior field. Finite slab solution is compared with the infinite case. Source is at $(x_s, y_s) = (0.01, 0.24)$ m, and the field point is at $(x_o, y_o) = (-3, y)$ m. (a) $\sigma = 0.195$ mS/m (b) $\sigma = 1.95$ mS/m

conductivity. Fig. 5.9.b shows the exterior field when we increase the slab conductivity to $\sigma = 1.95$ mS/m. The result shows that the GF-FS result for $2L = 15$ m converges better to the infinite slab solution when we add a small amount of loss to the dielectric

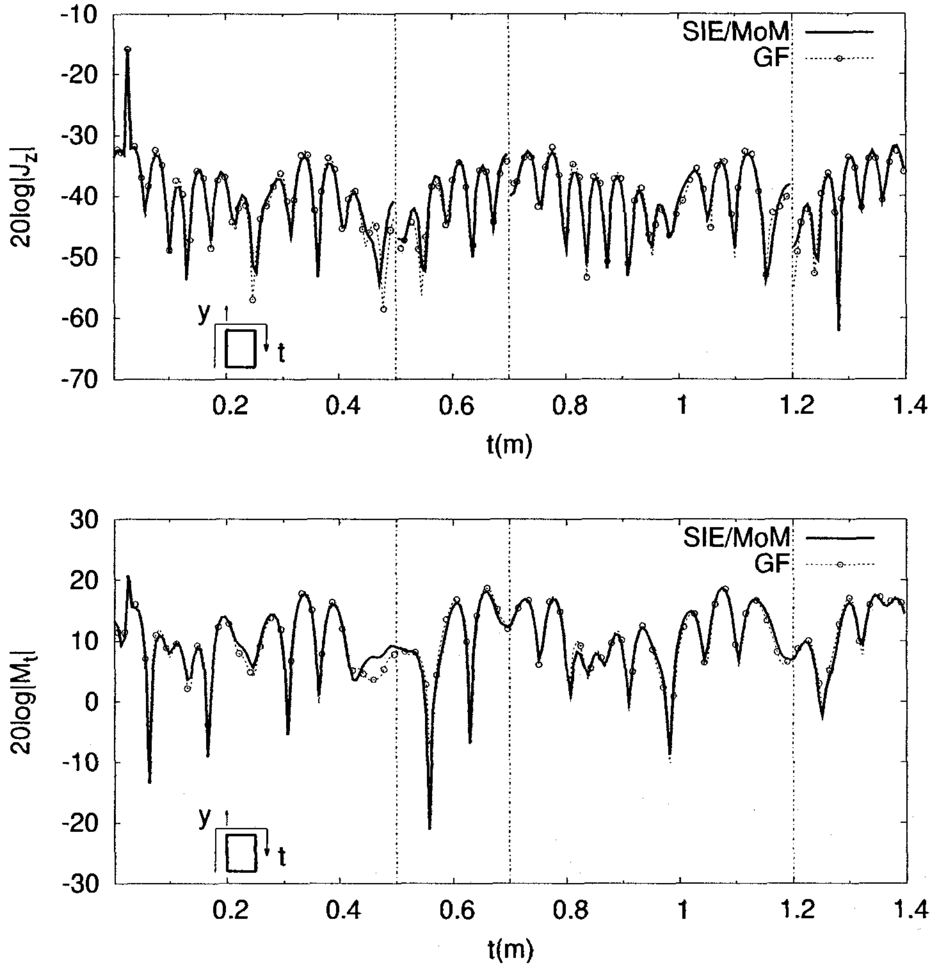

Figure 5.10: Surface equivalent currents generated by a line source on the surface of a finite dielectric slab with thickness of $2d = 0.2$ m and height of $2L = 0.5$ m. The line source is at $(x_s, y_s) = (0, -0.2226)$ m.

slab material.

We now consider a case when the current line source is on the surface of the finite slab with height $2L = 0.5$ m, and thickness $2d = 0.2$ m. The slab conductivity is $\sigma = 0.195$ mS/m. Fig. 5.10 shows the electric and magnetic surface current densities when the source is at $(x_s, y_s) = (0, -0.2226)$ m which corresponds to $t = 0.0274$ m, and $\boldsymbol{\rho}_5$, the center of the fifth cell. The slab height is divided into 82 cells, or $p = 41$. It is noted that the magnetic surface current should be singular at the source position.

However, the surface currents close to the source are computed here by using (5.4.23)-(5.4.24) which gives the mean value of the current over the cell extent. The mean value of the equivalent current is computed over the fifth cell and its six neighboring cells. It is also observed that the equivalent currents obtained by the GF do not match the currents computed by SIE/MoM at about $t = 0.48$ m. This happens near the end cap. In calculating the GF result, the end cap scattering matrix is used. The scattering matrix is calculated by finding the pulse basis currents at the end cap. However, a pulse basis current have a near field contribution that is not included in the total field near the end cap. It is observed that this near field contribution is strong near the end cap, and it becomes weak away from the end cap.

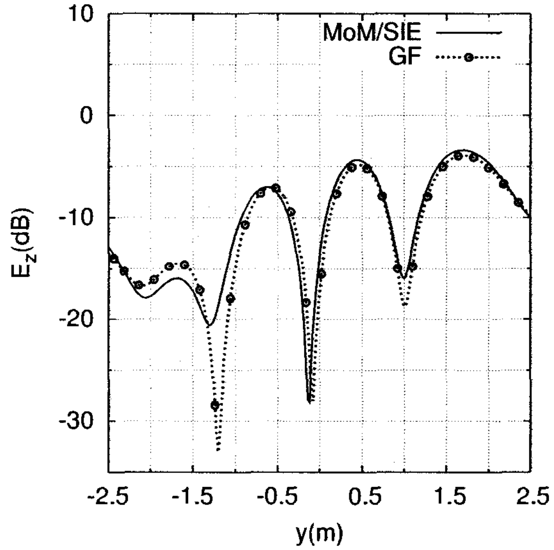

Figure 5.11: The exterior electric field generated by a line source on a surface of a finite dielectric slab. Source is at $(x_s, y_s) = (0, -0.2226)$ m, and the field point is at $(x_o, y_o) = (-3, y)$ m.

It is useful to compare the exterior field obtained by the surface currents. Fig. 5.11 shows the electric field outside the dielectric slab at $(x_o, y_o) = (-3, y)$ m. The result show that the error generated in the equivalent surface currents near the end cap does

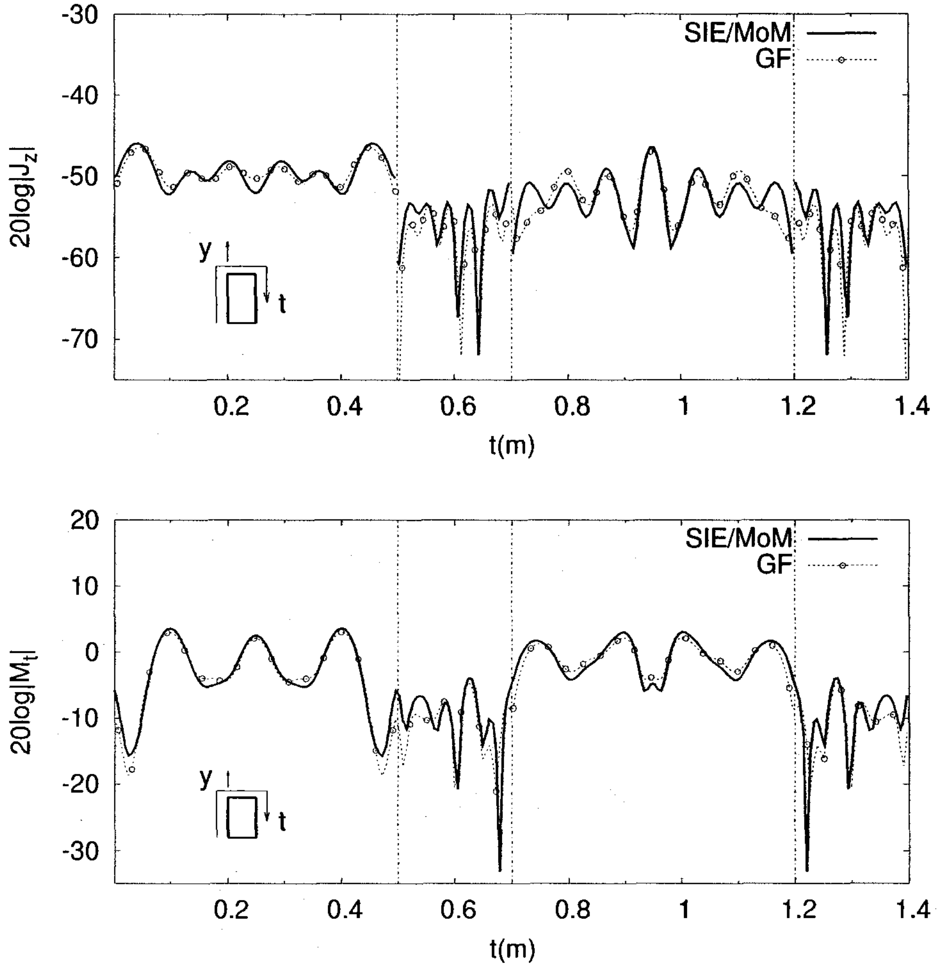

Figure 5.12: Surface equivalent currents generated by a line source at $(x_s, y_s) = (-1, 0)$ m.

not highly affect the exterior field.

To study the case when the source and the field point are both outside the finite slab, we place a line source at $(x_s, y_s) = (-1, 0)$ m. The slab size and slab characteristics are kept unchanged. Fig. 5.12 shows the electric and magnetic equivalent currents on the slab surface. The equivalent currents are obtained using SIE/MoM and GF techniques, and the results are compared. Having the equivalent surface currents, we can obtain the scattered electric field at an arbitrary point. Fig. 5.13 shows

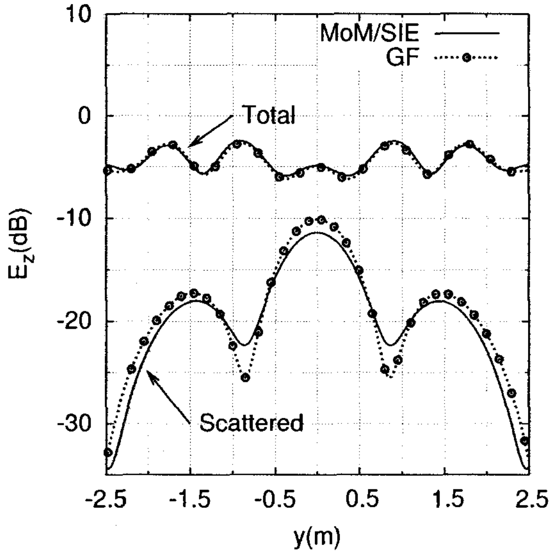

Figure 5.13: The total and scattered electric field generated by a line source outside a finite dielectric slab. Source is at $(x_s, y_s) = (-1, 0)$ m, and the field point is at $(x_o, y_o) = (-3, y)$ m.

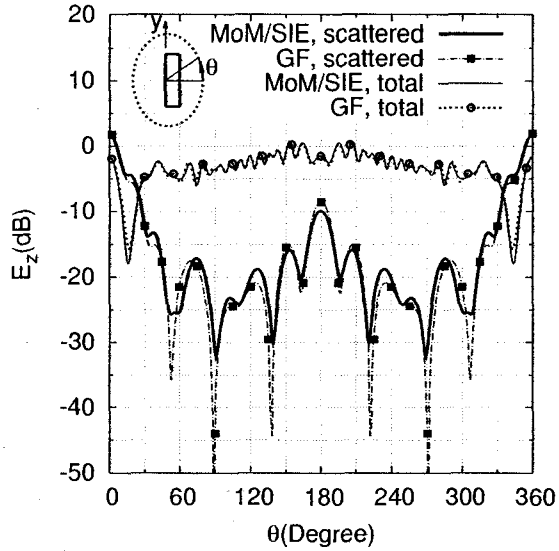

Figure 5.14: The total and scattered electric field generated by a line source outside a finite dielectric slab. Source is at $(x_s, y_s) = (-2, 0)$ m, and the field point is at $(x_o, y_o) = (\cos\theta, \sin\theta)$ m.

the scattered electric field at $(x_o, y_o) = (-3, y)$ m. It also shows the total electric field which is the summation of the incident and scattered fields, given in (5.4.26). It is noted that the scattered field includes both the reflected and diffracted fields by the FS. The result shows that the scattered field obtained by the GF method provides a satisfactory accuracy for computing the total field.

Fig. 5.14 shows another test case when the electric field is computed on a circular path around the FS. The field point is at $(x_o, y_o) = (\cos\theta, \sin\theta)$ m generated by a line source at $(x_s, y_s) = (-2, 0)$ m where the angle θ is measured counter-clockwise from the positive x axis. It is observed that the scattered field becomes strong in the range $-30 \leq \theta \leq 30$ where the slab is placed between the source and the field point. In this range, the total electric field represents the transmitted field plus the diffracted field.

Chapter 6

Analysis of a Finite Reinforced Concrete Slab

In this chapter, a 2D finite reinforced concrete slab is modeled by two different techniques. First, the MoM/GF is presented for solving this problem. The second approach uses the SIE/MoM. In doing so, the reinforced concrete is modeled by an array of metallic circular cylinders embedded inside a lossy dielectric material. (In civil engineering, the metallic circular cylinders representing the reinforcement rods are usually called rebars.)

In the MoM/GF approach, the MoM is applied for calculating the unknown induced currents on the surface of the rods by means of the finite slab GF. The interior GF is used in forming the impedance matrix in the MoM. By solving the system of equations in the MoM, the induced currents on the rods are calculated. Then, the scattered field due to the metallic rods is calculated from the induced currents. This requires using the finite slab GF.

The SIE/MoM is also applied to a finite reinforced concrete model where the MoM is used to calculate the unknown currents on the surface of the dielectric slab and the surface of the rods.

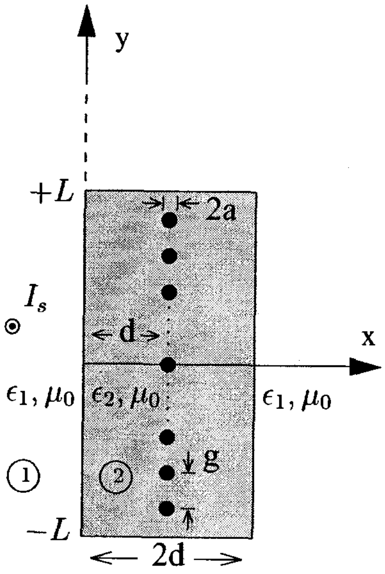

Figure 6.1: A model for a finite reinforced concrete slab. There are N_c PEC rods (•) embedded in a finite dielectric slab with height $2L$ and thickness $2d$. An electric line source of strength I_s is placed at $\boldsymbol{\rho}_s$ to the left of the slab.

6.1 Finite Reinforced Concrete Slab

Fig. 6.1 shows an array of N_c circular cylinders representing the metallic rods inside a finite, thick dielectric slab of height 2L and thickness 2d. The dielectric slab and exterior region permittivities are denoted by ϵ_2 and ϵ_1, respectively. All materials are assumed to be non-magnetic, so $\mu_1 = \mu_2 = \mu_0$. The center of each rod is denoted by $\boldsymbol{\rho}_k = x_k\hat{\boldsymbol{x}} + y_k\hat{\boldsymbol{y}}$, and $k = 1, 2, ...N_c$. All the rods are placed symmetrically about the x-axis at the center of the slab, so $x_k = d$. The rod spacing and rod diameter are denoted by g and $2a$, respectively. An electric line source of strength I_s is placed at $\boldsymbol{\rho}_s = x_s\hat{\boldsymbol{x}} + y_s\hat{\boldsymbol{y}}$ in the exterior region, and the field point is at $\boldsymbol{\rho}_o = x_o\hat{\boldsymbol{x}} + y_o\hat{\boldsymbol{y}}$.

Since the practical rods are usually electrically thick above UHF, it is possible to replace each rod by a circular array of thin wires subject to the "same surface area" rule of thumb [39]. That is, the total surface area of the thin wires should be equal to the surface area of the original rod. As a result, the radius of each wire should be

$b = a/N_w$, where N_w is the number of wires used to model each rod. The center of the thin wires are located at $\theta = 0°, \pm 360°/N_w, \pm 720°/N_w, \ldots$ on the surface of each rod where θ is measured counter-clockwise from the positive x axis. Fig. 6.2 shows the wire grid modeling of N_c thick rods where each rod is modeled with N_w thin wires. The first approach for solving this model will be the MoM/GF.

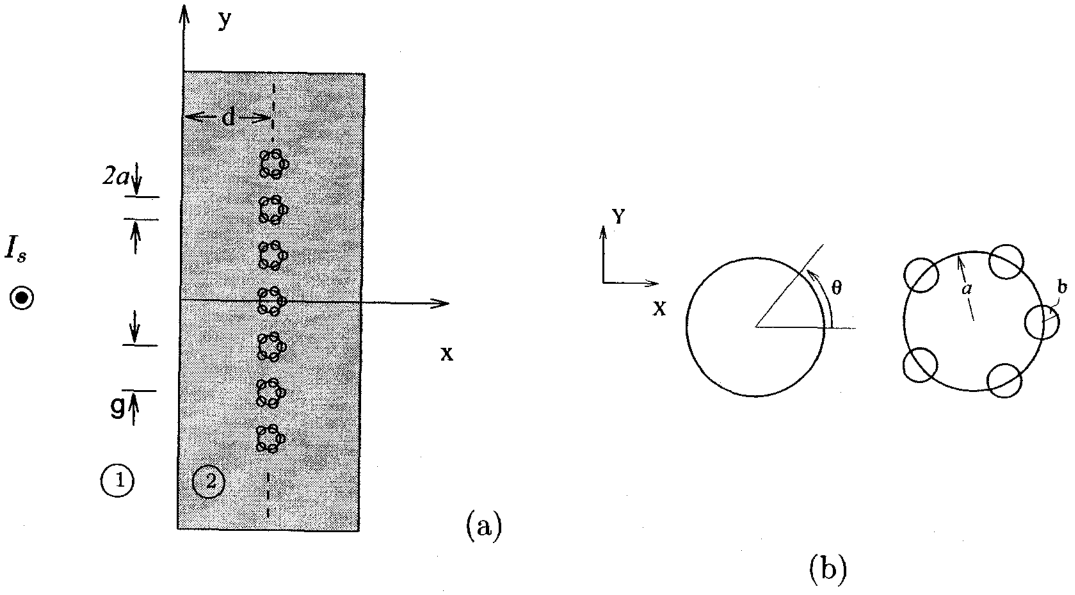

Figure 6.2: (a) Geometry of N_c rods inside a finite dielectric slab. Each rod has a diameter of $2a$ and placed at $x = d$. (b) Wire grid modeling of a rod with N_w wires.

6.1.1 MoM/GF

The electric field integral equation (EFIE) formulation is formed here in order to obtain the electric currents induced on the thin wires. The MoM is applied to solve the integral equations. The unknown induced current on the n'th wire placed at $\boldsymbol{\rho}_n = x_n\hat{\boldsymbol{x}} + y_n\hat{\boldsymbol{y}}$ is denoted by $I_n(\boldsymbol{\rho}_n)$ where $n = 1, 2, \ldots, N_cN_w$. These currents generate the scattered field in the presence of the finite dielectric slab. The scattered field can be written as

$$E^s(\boldsymbol{\rho}_o) = -j\omega\mu_0 \sum_{1}^{N_c N_w} I_n(\boldsymbol{\rho}_n) G_{ij}(\boldsymbol{\rho}_n, \boldsymbol{\rho}_o) \tag{6.1.1}$$

where G_{ij} is the finite slab Green's function, and i and j correspond to the field and source point position, respectively. In (6.1.1), we have $j = 2$ since the wires are inside Region ②. The total electric field, which is the scattered field plus the incident field, can be written as

$$E(\boldsymbol{\rho}_o) = E^i(\boldsymbol{\rho}_o) + E^s(\boldsymbol{\rho}_o). \tag{6.1.2}$$

The incident field $E^i(\boldsymbol{\rho}_o)$ can be written as

$$E^i(\boldsymbol{\rho}_o) = -j\omega\mu_0 I_s G_{ij}(\boldsymbol{\rho}_s, \boldsymbol{\rho}_o). \tag{6.1.3}$$

where $i = j = 1$ since the source and field points are outside the slab.

In order to form the system of equations, we should apply the boundary condition on the surface of the thin wires. This requires zero tangential electric field on the surface of the wires. However, it is easier to apply the point matching method at the center of each PEC wire. As a result, (6.1.2) becomes

$$E^s(\boldsymbol{\rho}_n) = -E^i(\boldsymbol{\rho}_n); \qquad n = 1, 2, ... N_c N_w \tag{6.1.4}$$

where the center of the n'th wire is denoted by $\boldsymbol{\rho}_n$. This forms the $N_c N_w \times N_c N_w$ system of equations

$$[Z][I] = [E^i] \tag{6.1.5}$$

where the elements of the impedance matrix $[Z]$ are given by

$$Z_{mn} = -j\omega\mu_0 G_{22}(\boldsymbol{\rho}_n, \boldsymbol{\rho}_m). \tag{6.1.6}$$

For the line source in the exterior region, the elements of the excitation column $[E^i]$ can be obtained from

$$E_n^i = -j\omega\mu_0 I_s G_{21}(\boldsymbol{\rho}_s, \boldsymbol{\rho}_n). \tag{6.1.7}$$

The solution to the system of equations (6.1.5) gives the unknown wire currents I_n's. Having the induced currents on the wires, the scattered field by the wires can be obtained by using (6.1.1). The total scattered field is the field scattered by the wires plus the finite dielectric slab.

6.1.2 SIE/MoM

The SIE/MoM can also be applied to the reinforced concrete slab shown in Fig. 6.2. The EFIE formulation is formed to calculate the unknown electric and magnetic surface currents on the dielectric slab surface, and the unknown electric currents of the wires. In doing so, the surface equivalence principle is first applied to Region ①. The equivalent electric and magnetic surface currents are placed on the slab surface. Since the source is assumed to be in Region ①, the total exterior electric field can be written as

$$\boldsymbol{E} = \boldsymbol{E}^i(I_s) + \boldsymbol{E}^s(\boldsymbol{J}_1^{eq}, \boldsymbol{M}_1^{eq}) \tag{6.1.8}$$

where $\boldsymbol{E}^i$ is the incident field generated by the source I_s in the absence of the slab, and $\boldsymbol{E}^s$ is the scattered field by Region ②. The incident field $\boldsymbol{E}^i$ can be obtained by using (3.1.5) and the free space Green's function given in (A.5-7). The equivalent surface currents generate the scattered field in the exterior region. Furthermore, it is convenient to have a zero total field in Region ②. This defines the surface equivalent electric and magnetic currents as

$$\boldsymbol{J}_1^{eq} = \hat{\boldsymbol{n}}_1 \times \boldsymbol{H} \tag{6.1.9}$$

$$\boldsymbol{M}_1^{eq} = \boldsymbol{E} \times \hat{\boldsymbol{n}}_1 \tag{6.1.10}$$

where $\boldsymbol{H}$ is the total magnetic field vector, and $\hat{\boldsymbol{n}}_1$ is the normal unit vector pointing toward the exterior region. Since the total field in Region ② for the equivalent problem is zero, it is useful to replace everything in Region ② with the same material that is used in Region ①. As a result, the problem becomes homogeneous and the free space Green's function can be used. The equivalent exterior problem is shown in Fig. 6.3.a. The unit vector $\hat{\boldsymbol{t}}$ which is tangent to the boundary S is defined so that $\hat{\boldsymbol{n}}_1 \times \hat{\boldsymbol{t}} = \hat{\boldsymbol{z}}$. The surface equivalent magnetic current can be represented by a scalar tangential component M_t where $\boldsymbol{M}_1^{eq} = M_t\hat{\boldsymbol{t}}$. Similarly, we have $\boldsymbol{J}_1^{eq} = J_z\hat{\boldsymbol{z}}$. After using (6.1.8) in (6.1.10), we can form the EFIE for the exterior region as

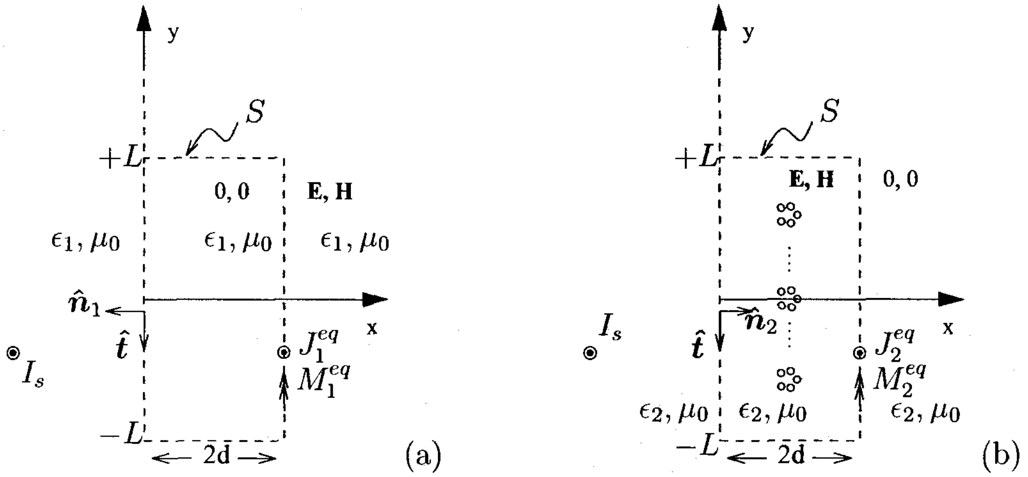

Figure 6.3: (a) The equivalent exterior problem. (b) The equivalent interior problem.

$$E_z^i(\ell) = M_t(\ell) - E_z^s(\ell) \tag{6.1.11}$$

where

$$\begin{aligned}E_z^s(\ell) = &-\frac{\omega\mu_0}{4}\oint_S J_z(\ell')H_0^{(2)}(k_1\rho)d\ell' \\ &-\frac{k_1}{4j}\oint_S \hat{\boldsymbol{t}}(\ell')\cdot(\hat{\boldsymbol{y}}\frac{x(\ell')-x(\ell)}{\rho} - \hat{\boldsymbol{x}}\frac{y(\ell')-y(\ell)}{\rho})M_t(\ell')H_1^{(2)}(k_1\rho)d\ell'\end{aligned} \tag{6.1.12}$$

and

$$\rho = \sqrt{(x(\ell)-x(\ell'))^2 + (y(\ell)-y(\ell'))^2}. \tag{6.1.13}$$

It is noted that E_z^s is generated by the equivalent electric and magnetic currents, and the electric field generated by M_y and M_x is given in (A.5-8)-(A.5-9). The parametric variable ℓ' denotes the surface position. The line integral in (6.1.12) is taken in the direction of increasing ℓ.

Now we apply the surface equivalence principle to Region ②. After generating zero fields in the exterior region, the exterior region material can be replaced with the material of Region ②. To produce null fields in the exterior region, The equivalent electric surface current $\boldsymbol{J}_2^{eq}$ and the magnetic surface current $\boldsymbol{M}_2^{eq}$ are placed on the slab surface as shown in Fig. 6.3.b. These currents satisfy the boundary condition due to the field discontinuities as

$$\boldsymbol{J}_2^{eq} = \hat{\boldsymbol{n}}_2 \times \boldsymbol{H} \tag{6.1.14}$$

$$\boldsymbol{M}_2^{eq} = \boldsymbol{E} \times \hat{\boldsymbol{n}}_2 \tag{6.1.15}$$

where $\hat{\boldsymbol{n}}_2$ is a normal unit vector to the slab surface which is pointing inward. Furthermore, the equivalent electric currents, which are denoted by I_χ's, replace the thin wires. It is noted that the equivalent magnetic currents on the wires are zero since the tangential electric field should vanish on the wire surface. Since the tangential fields should be continuous at the slab boundary (using (6.1.9)-(6.1.10) and

(6.1.14)-(6.1.15)), we should have

$$\boldsymbol{J}_1^{eq} = -\boldsymbol{J}_2^{eq} \tag{6.1.16}$$

$$\boldsymbol{M}_1^{eq} = -\boldsymbol{M}_2^{eq}. \tag{6.1.17}$$

The total electric field in Region ② can be written as

$$E = E^{s2}(\boldsymbol{J}_2^{eq}, \boldsymbol{M}_2^{eq}, I_\chi) \qquad \chi = 1, 2, ...N_c N_w. \tag{6.1.18}$$

By using (6.1.17)-(6.1.18) in (6.1.15), the EFIE formulation for Region ② becomes

$$\begin{aligned} 0 &= -M_t(\ell) - E^{s2}(\boldsymbol{J}_2^{eq}, \boldsymbol{M}_2^{eq}, I_\chi) && \ell \in \text{boundary S} \\ 0 &= -E^{s2}(\boldsymbol{J}_2^{eq}, \boldsymbol{M}_2^{eq}, I_\chi) && \ell \in \text{thin wire surface} \end{aligned} \tag{6.1.19}$$

where the scattered field in Region ② is given by

$$\begin{aligned} E^{s2}(\boldsymbol{J}_2^{eq}, \boldsymbol{M}_2^{eq}, I_\chi) = & -\frac{\omega\mu_0}{4}\oint_S J_z(\ell')H_0^{(2)}(k_2\rho)d\ell' \\ & -\frac{k_2}{4j}\oint_S \hat{\boldsymbol{t}}(\ell')\cdot(\hat{\boldsymbol{y}}\frac{x(\ell')-x(\ell)}{\rho} - \hat{\boldsymbol{x}}\frac{y(\ell')-y(\ell)}{\rho})M_t(\ell')H_1^{(2)}(k_2\rho)d\ell' \\ & -\frac{\omega\mu_0}{4}\sum_{\chi=1}^{N_cN_w} I_\chi(\boldsymbol{\rho}_\chi)H_0^{(2)}(k_2\rho_w) \end{aligned} \tag{6.1.20}$$

and

$$\rho_w = \sqrt{(x(\ell)-x_\chi)^2 + (y(\ell)-y_\chi)^2}. \tag{6.1.21}$$

The MoM is now used to solve the EFIE and to calculate the unknown currents on the slab surface and thin wires. Fig. 6.4 shows the slab surface segmentation. The dielectric slab height and width are divided into M and N cells, respectively. This

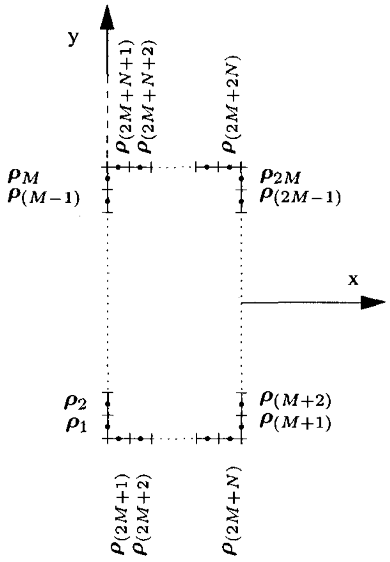

Figure 6.4: The finite slab is divided into $2(M+N)$ cells.

leads to $2M+2N$ cells on the slab surface. The cell sizes in the x and y direction are denoted by δ_x and δ_y, respectively. The pulse basis functions can be used to approximate the electric and magnetic current distribution as

$$J_z(\boldsymbol{\rho}_t) = \sum_{n=1}^{2M+2N} I_n P_n(\boldsymbol{\rho}_t) \tag{6.1.22}$$

$$M_t(\boldsymbol{\rho}_t) = \sum_{n=1}^{2M+2N} K_n P_n(\boldsymbol{\rho}_t) \tag{6.1.23}$$

where $P_n(\boldsymbol{\rho}_t)$ is given in (5.4.8). The unknown coefficients I_n and K_n represent the unknown electric and magnetic currents on the n'th cell where $n = 1, 2, ..., 2M+2N$. To discretize (6.1.11) and (6.1.19) and form the system of equations, (6.1.11) and (6.1.19) are enforced at the center of each cell and on the surface of each wire. The

$(2M+2N+N_cN_w)\times(2M+2N+N_cN_w)$ system of equations form the matrix equation

$$\begin{bmatrix} \boldsymbol{E}^{inc} \\ \mathbf{0} \\ \mathbf{0} \end{bmatrix} = \begin{bmatrix} \boldsymbol{Z}^{(11)} & \boldsymbol{Z}^{(12)} & \mathbf{0} \\ \boldsymbol{Z}^{(21)} & \boldsymbol{Z}^{(22)} & \boldsymbol{Z}^{(23)} \\ \boldsymbol{Z}^{(31)} & \boldsymbol{Z}^{(32)} & \boldsymbol{Z}^{(33)} \end{bmatrix} \begin{bmatrix} \boldsymbol{I} \\ \boldsymbol{K} \\ \boldsymbol{I}_\chi \end{bmatrix} \tag{6.1.24}$$

where the elements of each submatrix are given as

$$Z_{mn}^{11} = \frac{\omega\mu_0}{4}\int_{\boldsymbol{\rho}_n-\frac{\boldsymbol{\delta}_n}{2}}^{\boldsymbol{\rho}_n+\frac{\boldsymbol{\delta}_n}{2}} H_0^{(2)}(k_1\rho_m)d\ell' \tag{6.1.25}$$

$$Z_{mn}^{12} = \frac{k_1}{4j}\int_{\boldsymbol{\rho}_n-\frac{\boldsymbol{\delta}_n}{2}}^{\boldsymbol{\rho}_n+\frac{\boldsymbol{\delta}_n}{2}} \hat{\boldsymbol{t}}(\ell')\cdot(\hat{\boldsymbol{y}}\frac{x(\ell')-x_m}{\rho_m} - \hat{\boldsymbol{x}}\frac{y(\ell')-y_m}{\rho_m})H_1^{(2)}(k_1\rho_m)d\ell' \tag{6.1.26}$$

$$Z_{mn}^{21} = \frac{\omega\mu_0}{4}\int_{\boldsymbol{\rho}_n-\frac{\boldsymbol{\delta}_n}{2}}^{\boldsymbol{\rho}_n+\frac{\boldsymbol{\delta}_n}{2}} H_0^{(2)}(k_2\rho_m)d\ell' \tag{6.1.27}$$

$$Z_{mn}^{22} = \frac{k_2}{4j}\int_{\boldsymbol{\rho}_n-\frac{\boldsymbol{\delta}_n}{2}}^{\boldsymbol{\rho}_n+\frac{\boldsymbol{\delta}_n}{2}} \hat{\boldsymbol{t}}(\ell')\cdot(\hat{\boldsymbol{y}}\frac{x(\ell')-x_m}{\rho_m} - \hat{\boldsymbol{x}}\frac{y(\ell')-y_m}{\rho_m})H_1^{(2)}(k_2\rho_m)d\ell' \tag{6.1.28}$$

$$Z_{m\chi}^{23} = \frac{\omega\mu_0}{4}H_0^{(2)}(k_2\rho_{m\chi}) \tag{6.1.29}$$

$$Z_{\nu n}^{31} = \frac{\omega\mu_0}{4}\int_{\boldsymbol{\rho}_n-\frac{\boldsymbol{\delta}_n}{2}}^{\boldsymbol{\rho}_n+\frac{\boldsymbol{\delta}_n}{2}} H_0^{(2)}(k_2\rho_\nu)d\ell' \tag{6.1.30}$$

$$Z_{\nu n}^{32} = \frac{k_2}{4j}\int_{\boldsymbol{\rho}_n-\frac{\boldsymbol{\delta}_n}{2}}^{\boldsymbol{\rho}_n+\frac{\boldsymbol{\delta}_n}{2}} \hat{\boldsymbol{t}}(\ell')\cdot(\hat{\boldsymbol{y}}\frac{x(\ell')-x_\nu}{\rho_\nu} - \hat{\boldsymbol{x}}\frac{y(\ell')-y_\nu}{\rho_\nu})H_1^{(2)}(k_2\rho_\nu)d\ell' \tag{6.1.31}$$

$$Z_{\nu\chi}^{33} = \frac{\omega\mu_0}{4}H_0^{(2)}(k_2\rho_{\nu\chi}) \tag{6.1.32}$$

It is noted that the indices m and n are used for the surface cells, so $m,n = 1,2,...,(2M+2N)$. Furthermore, the variables ν and χ refer to the wires, and

$\nu, \chi = 1, 2, ..., N_c N_w$. The Euler's constant is $\gamma = 1.781072$. We also have

$$\rho_{m,\nu} = \sqrt{(x(\ell') - x_{m,\nu})^2 + (y(\ell') - y_{m,\nu})^2} \tag{6.1.33}$$

$$\rho_{m\chi,\nu\chi} = \sqrt{(x_\chi - x_{m,\nu})^2 + (y_\chi - y_{m,\nu})^2}. \tag{6.1.34}$$

$$\boldsymbol{\delta}_n = \begin{cases} \delta_y \hat{\boldsymbol{y}} & 1 \leq n \leq 2M \\ \delta_x \hat{\boldsymbol{x}} & 2M + 1 \leq n \leq 2M + 2N \end{cases} \tag{6.1.35}$$

The self term impedance terms Z^{11}_{mm} and Z^{21}_{mm} can be obtained for (6.1.25) and (6.1.27) by using (A.8-4). Applying the reciprocity theorem and using (A.7-4) and (A.7-15), the self term elements of $\boldsymbol{Z}^{12}$ and $\boldsymbol{Z}^{22}$ becomes

$$Z^{12}_{mm} = \frac{1}{2} \tag{6.1.36}$$

$$Z^{22}_{mm} = -\frac{1}{2}. \tag{6.1.37}$$

The self impedance terms of $\boldsymbol{Z}^{33}$ can be obtained by means of the thin wire approximation. Letting $\rho_{\nu\chi} = b$ in (6.1.32) and using the small argument formulation for the Hankel function, the self term elements of $\boldsymbol{Z}^{33}$ become

$$Z^{33}_{\nu\nu} = \frac{\omega\mu_0}{4}(1 - j\frac{2}{\pi}\ln(\gamma k_2 b/2)). \tag{6.1.38}$$

The elements of the column vector $\boldsymbol{E}^{inc}$ in (6.1.24) are given as

$$E^{inc}_m = -\frac{\omega\mu_0}{4} H^{(2)}_0(k_1 \rho_{sm}) \tag{6.1.39}$$

where

$$\rho_{sm} = \sqrt{(x_s - x_m)^2 + (y_s - y_m)^2}. \tag{6.1.40}$$

The unknown currents are obtained by solving the system of equations (6.1.24). Having the unknown currents, the exterior field can be obtained using (6.1.8) and (6.1.12). Similarly, the electric field in Region ② is obtained by using (6.1.18) and (6.1.20).

6.2 Results and Discussion

The results obtained by the implemented Fortran codes based on the MoM/GF and SIE/MoM techniques are compared here. It is important to note that the size of the impedance matrix in SIE/MoM approach directly depends on the surface area of the dielectric slab. As a result, the SIE/MoM technique is not computationally efficient when the slab is electrically large.

To validate the MoM/GF technique, we chose the frequency $f = 1.8$ GHz, slab height $2L = 50$ cm and slab thickness $2d = 20$ cm. The properties of the dielectric slab material were characterized by $\epsilon_r = 6$ and $\sigma_2 = 0.195$ mS/m. The exterior region permittivity was $\epsilon_1 = \epsilon_0$. We placed $N_c = 5$ rods inside the the slab. The rods were $g = 5$ cm away from each other, so $x_k = 10$ cm and $y_k = 0, \pm 5, \pm 10$ cm. The diameter of each rod was $2a = 2$ cm. Modeling every rod by a wire grid, $N_w = 5$ wires were required for modeling each rod. This was in accordance with [44], which suggested the grid size of 0.2λ or less. Using the equal surface area rule, the diameter of the thin wires became $2b = 0.4$ cm. Referring to Fig. 6.2.b, the center of the thin wires are located at $\theta = 0^\circ, \pm 72^\circ, \pm 144^\circ$ on the surface of each rod. Fig. 6.5 shows the exterior scattered electric field on a circular path defined by $(x_o, y_o) = (0.4\cos\theta, 0.4\sin\theta)$ m where the angle θ is measured counter-clockwise from the positive x axis. The electric field is generated by a line source I_s at $(x_s, y_s) = (-0.2, 0)$ m. Results have been generated by MoM/GF, SIE/MoM and HFSS. To form a 2D waveguide structure using HFSS, we placed our structure between two PEC parallel plates 1 cm apart at $z = \pm 0.5$ cm. We formed a $1.2 \times 1.2 \times 0.01$ m air box embedding the structure. The

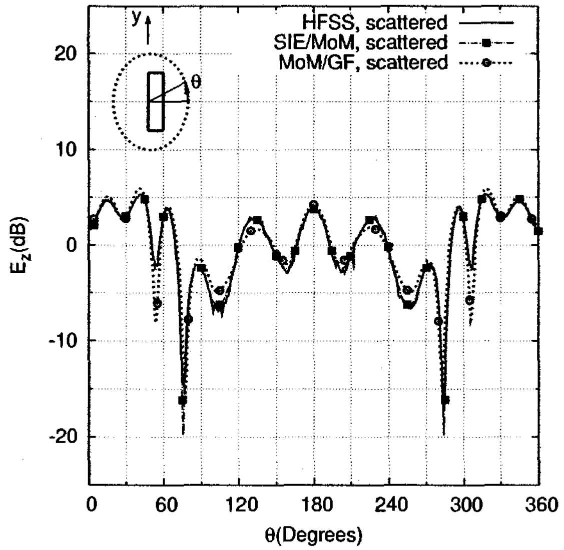

Figure 6.5: The field scattered by a finite reinforced concrete slab. The source is at $(x_s, y_s) = (-0.2, 0)$ m, and the field point is at $(x_o, y_o) = (0.4\cos\theta, 0.4\sin\theta)$ m. $N_c = 5$ rods are inside a $2L \times 2d = 0.5 \times 0.2$ m finite dielectric slab.

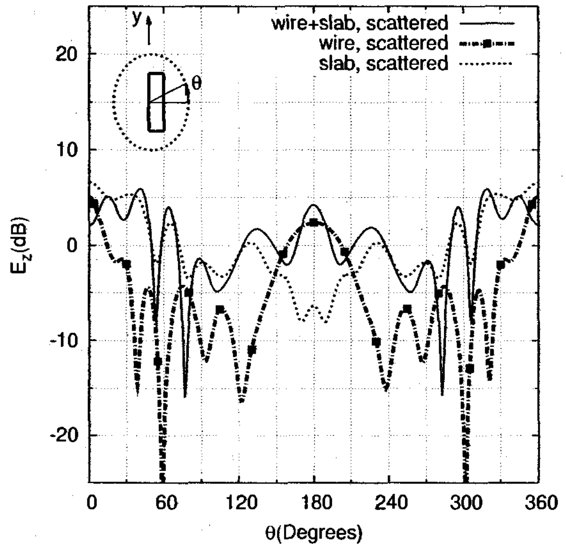

Figure 6.6: The field scattered by a finite reinforced concrete slab, calculated by the MoM/GF technique. The source is at $(x_s, y_s) = (-0.2, 0)$ m, and the field point is at $(x_o, y_o) = (0.4\cos\theta, 0.4\sin\theta)$ m.

four faces of the air box parallel to the z axis were defined as radiation boundaries. The rods were modeled by circular PEC cylinders in HFSS unlike MoM/GF and

SIE/MoM for which wire grid modeling was used. The final mesh in HFSS had 46928 tetrahedra. The SIE/MoM solved a 485×485 impedance matrix, while the impedance matrix in MoM/GF had a dimension of 25×25.

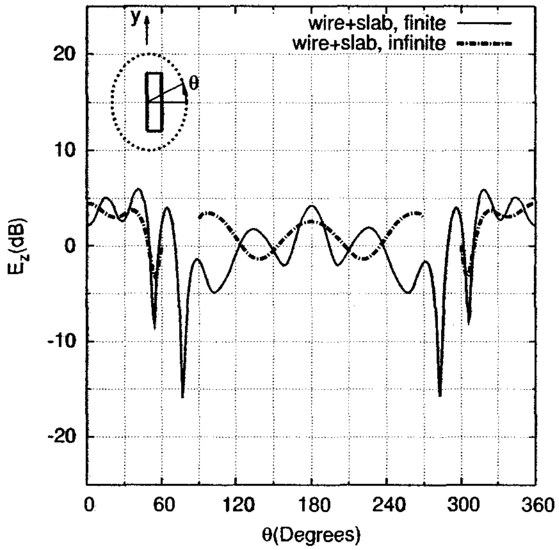

Figure 6.7: Comparing the scattered field by a finite and infinite reinforced concrete slab. The MoM/GF technique has been used. The source is at $(x_s, y_s) = (-0.2, 0)$ m, and the field point is at $(x_o, y_o) = (0.4\cos\theta, 0.4\sin\theta)$ m. The finite slab size is $2L \times 2d = 0.5 \times 0.2$ m. $N_c = 5$ rods were placed inside the finite and infinite slab.

It is noted that the scattered field generated by MoM/GF is the field scattered by the dielectric slab plus the field scattered by the wires. Fig. 6.6 shows the components of the scattered field separately. It is seen that the forward scattering is larger than the backward scattering for both wires and slab.

To observe the effect caused by the finiteness of the dielectric slab, we can compare the finite slab with the infinite slab. In order to do that, we let $2L \to \infty$. The MoM/GF is used for modeling wires inside the infinite slab [39]. This is done by using infinite slab GF in (6.1.1), (6.1.3) and (6.1.6)-(6.1.7). The thin wires inside the infinite slab have the same size and same geometry as they had in the finite slab. The dielectric characteristics are also the same in both finite and infinite slabs.

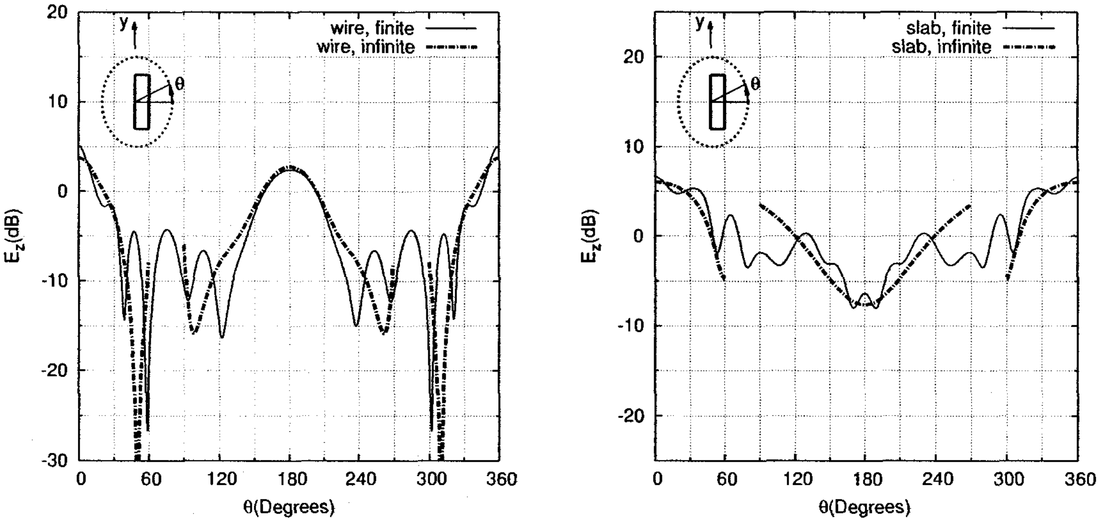

(a) (b)

Figure 6.8: (a) The comparison of the scattered field by the wires inside a finite and infinite dielectric slab. (b) The comparison of the scattered field by the finite and infinite dielectric slab.

Fig. 6.7 shows the scattered field for the reinforced concrete slab when the slab is finite and infinite. $N_c = 5$ rods were placed inside the finite and infinite slab. The diameter and the geometry of the rods were kept unchanged. When $60^\circ < \theta < 90^\circ$ and $240^\circ < \theta < 270^\circ$, the field points are not shown for the infinite slab since the field points in these ranges are inside the dielectric slab. The result shows that the finiteness of the slab can highly affect the scattered field, specially close to the slab surface when $90^\circ < \theta < 120^\circ$. Since the scattered field can be decomposed into the wire and slab contributions, it is possible to investigate each separately.

Fig. 6.8.a shows the scattered field contributed by the wires only, when the wires are inside the finite and infinite slab. The result shows the effect of the slab finiteness on the wires. It can be observed that the slab finiteness has a small effect on the forward and backward scattering contributed by wires. A similar comparison in Fig. 6.8.b shows the scattered field contributed by the slab for the finite and infinite case, when the wires are removed. The effect of the end caps in this example on the

forward and backward scattering is less than 2 dB.

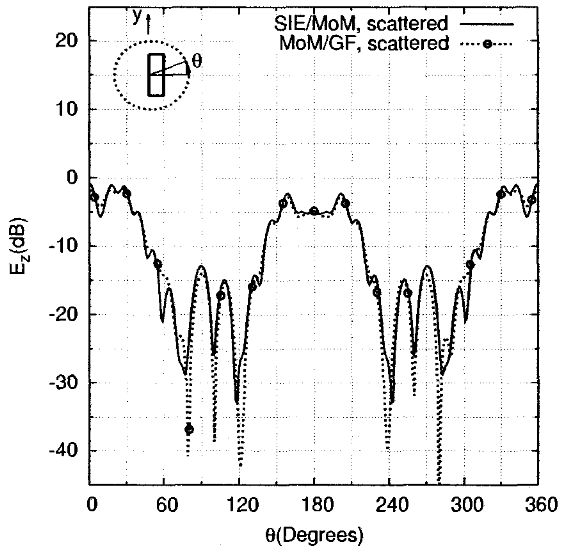

Figure 6.9: The scattered field for a finite reinforced concrete slab. The source is at $(x_s, y_s) = (-2, 0)$ m, and the field point is at $(x_o, y_o) = (\cos\theta, \sin\theta)$ m. $N_c = 19$ rods are placed inside a $2L \times 2d = 1 \times 0.2$ m finite dielectric slab. The rod spacing is $g = 5$ cm.

To generate results for larger slab dimensions, we increased the slab height to $2L = 1$ m. We also increased the number of rods inside the slab to $N_c = 19$. Other parameters were kept unchanged. The source was at $(x_s, y_s) = (-2, 0)$ m, and the field point was computed at $(x_o, y_o) = (\cos\theta, \sin\theta)$ m. Fig. 6.9 shows the scattered field calculated by MoM/SIE and MoM/GF. Since the finite element method which uses volume discretization could result in a large number of unknowns for this problem, we did not use HFSS. The size of the impedance matrix in the SIE/MoM approach was 883 × 883, while the MoM/GF solved a smaller impedance matrix having the dimension of 95 × 95.

Fig. 6.10.a shows the components of the scattered field which are the contributions due to the wires and the slab without the wires. When the wires are removed, it is shown that the forward scattering for the slab is about 11 dB stronger than the

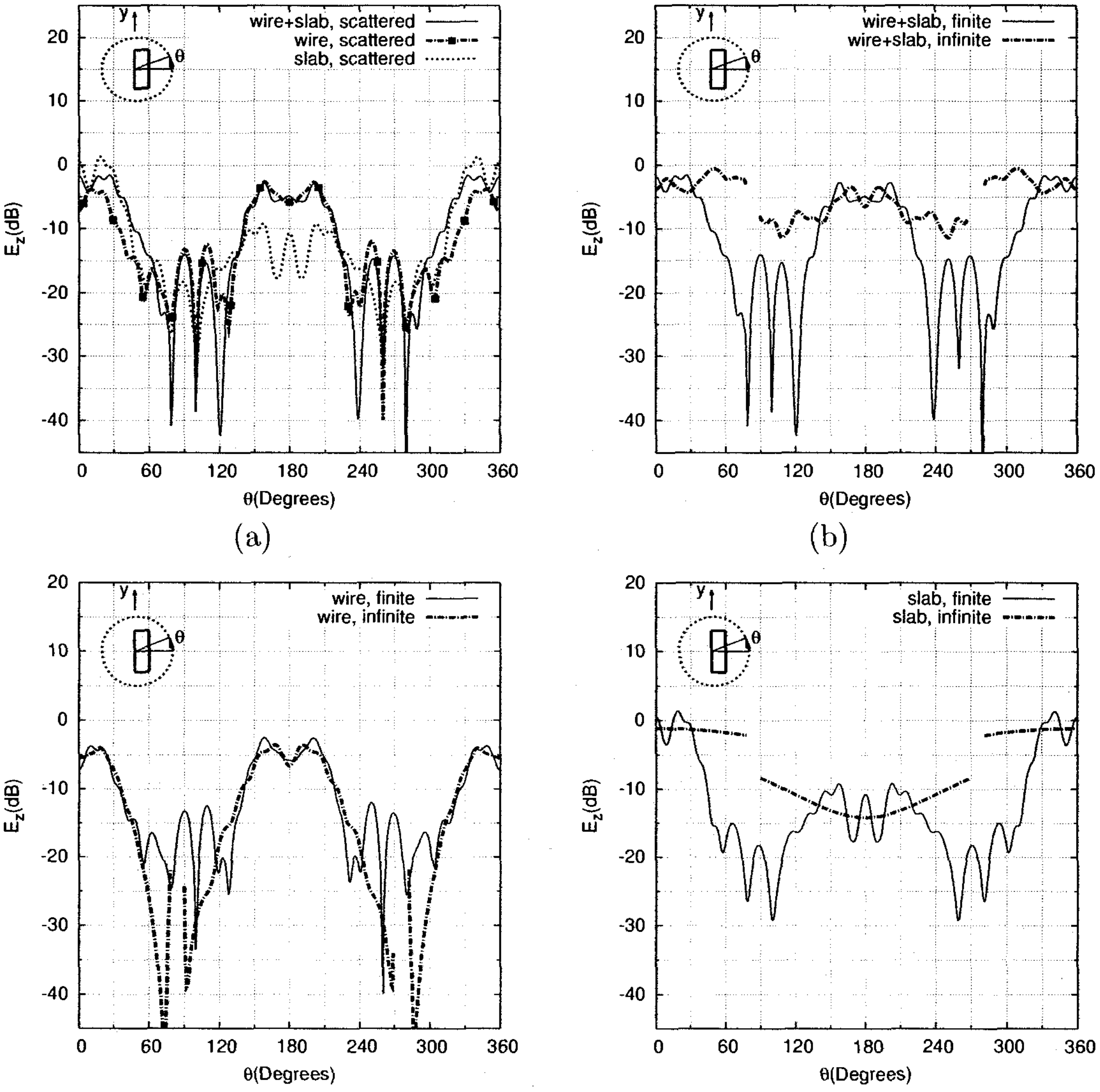

(a) (b)

(c) (d)

Figure 6.10: (a) The scattered field for the reinforced concrete slab. The scattered field consists of the contribution due to the wires and the slab without wires. The scattered field at $(x_o, y_o) = (\cos\theta, \sin\theta)$ m generated by a line source at $(x_s, y_s) = (-2, 0)$ m behind (b) a finite and infinite reinforced concrete slab, (c) the wires inside the finite and infinite dielectric slab, and (d) the finite and infinite dielectric slab when the wires are removed. The finite reinforced concrete model has a dimension of $2L \times 2d = 1 \times 0.2$ m in (a), (b), (c), and (d). The number of rods $N_c = 19$ is used. The rod spacing is $g = 5$ cm.

backward scattering.

Fig. 6.10.b compares the scattered field for a finite and infinite reinforced slab.

For this example, the finiteness effect is not very strong in the specular directions ($137^\circ < \theta < 223^\circ$). However, the end caps highly affect the scattered field when the field points are in off-specular directions ($90^\circ < \theta < 137^\circ$, $223^\circ < \theta < 270^\circ$). Fig. 6.10.c shows the scattering contribution due to the wires inside the finite and infinite slab. The result shows that the end caps affect the scattered field by the wires when the field point is close to the infinite slab surface ($90^\circ < \theta < 120^\circ$, $240^\circ < \theta < 270^\circ$). In these regions, the surface waves generated by the wires are strong. Fig. 6.10.d also compares the scattered field contribution for the finite and infinite slab. It can be observed that the end cap effect on the backward and forward scattering is 3.5 dB and 1.7 dB, respectively. This effect becomes strong when the field point is in off-specular directions.

Following the trend of increasing the length, we changed the slab length to $2L = 5$ m. Fig. 6.11 shows the scattered field generated for a line source at $(x_s, y_s) = (-2, 0)$ m behind the finite reinforced slab. Fig. 6.11.a shows the electric field when the field point is at $(x_o, y_o) = (-3, y)$ m. Furthermore, Fig. 6.11.b shows the scattered field at $(x_o, y_o) = (3, y)$ m. $N_c = 33$ rods are placed inside the slab, and the rod spacing is $g = 15.24$ cm (6 in). We also chose the wire diameter to be $2a = 1.91$ cm (3/4 in). The scattered field results generated by MoM/GF and SIE/MoM techniques are compared. A very good agreement is observed. The size of the impedance matrix solved by SIE/MoM technique was 3569×3569, unlike the MoM/GF approach which used the impedance matrix having the size of 165×165.

Fig. 6.12 compares the finite and infinite case when the field point is at $(x_o, y_o) = (-3, y)$ m (shown in Fig. 6.12.a, Fig. 6.12.c and Fig. 6.12.e) and at $(x_o, y_o) = (3, y)$ m (shown in Fig. 6.12.b, Fig. 6.12.d and Fig. 6.12.f). The source is at $(x_s, y_s) = (-2, 0)$ m. The finite slab results were obtained using MoM/GF. The contributions due to the wires and slab are also compared separately. The results shown

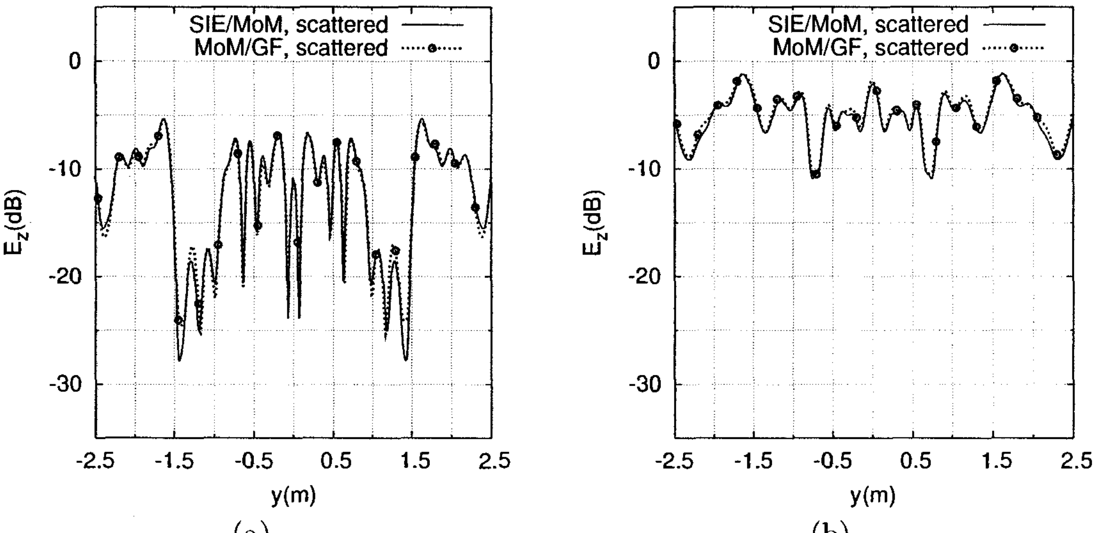

(a)

(b)

Figure 6.11: The scattered field for a finite reinforced concrete slab. The source is at $(x_s, y_s) = (-2, 0)$ m. $N_c = 33$ rods are placed inside a $2L \times 2d = 5 \times 0.2$ m finite dielectric slab. The rod spacing is $g = 15.24$ cm. The field point is at (a) $(x_o, y_o) = (-3, y)$ m, (b) $(x_o, y_o) = (3, y)$ m.

in Fig. 6.12.c and Fig. 6.12.d suggest that the end cap effect on the scattered field due to the wires is small. Fig. 6.12.e and Fig. 6.12.f also show the effect of the end cap contribution by comparing the finite and infinite dielectric slab. The end cap contribution appears to have a negligible effect on the forward scattering.

It might be speculated that when $2L = 5$ m, the infinite slab Green's function can be used for calculating the scattering by a finite reinforced slab if the field point is not close to the end caps. Furthermore, it appears that the end cap contribution to the scattered field can be neglected since the contribution is very small. In order to verify this speculation, it is useful to find a case when the end cap contributions are strong compared to the transmitted field. In doing so, we first change the rod spacing inside the infinite slab and we obtain a rod spacing that highly blocks the transmitted field. Next, we compare the finite and infinite cases with the obtained rod spacing. It is anticipated that the end caps might alter the transmitted field when the transmitted

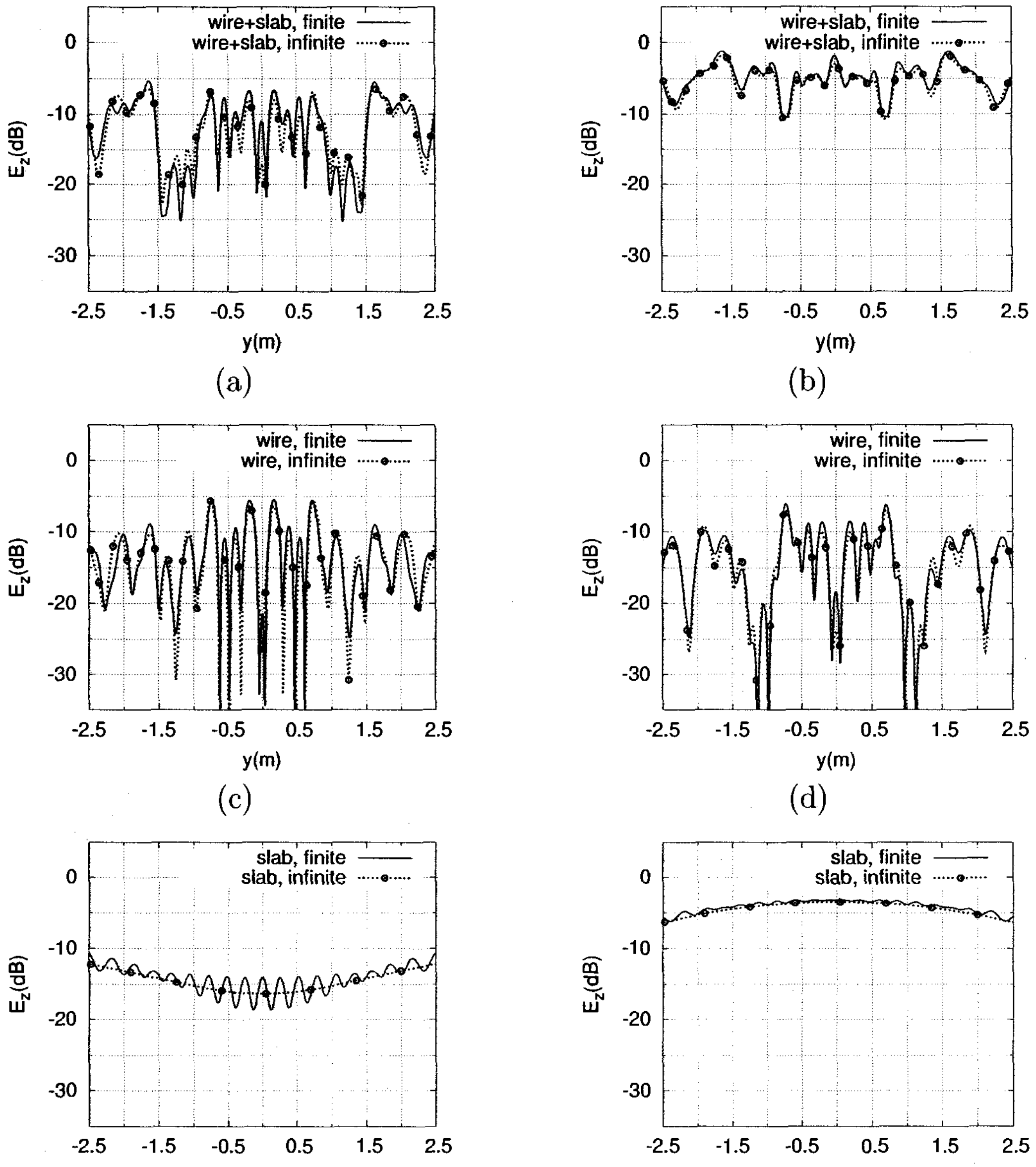

(a) (b)

(c) (d)

(e) (f)

Figure 6.12: (a,b) The scattered field for the reinforced concrete slab. The scattered field consists of the contribution due to the wires shown in (c-d), and the contribution due to the slab without wires shown in (e-f). The scattered field (a,c,e) at $(x_o, y_o) = (-3, y)$ m and (b,d,f) at $(x_o, y_o) = (3, y)$ m. The finite slab dimension is $2L \times 2d = 5 \times 0.2$ m. $N_c = 33$ rods are placed inside the dielectric slab. The rod spacing is $g = 15.24$ cm. The source is at $(x_s, y_s) = (-2, 0)$ m.

field is small.

Fig. 6.13 shows the effect of the rod spacing on the average of the transmitted field which has been calculated along the line $(x_o, y_o) = (3, -2.5 < y < 2.5)$ m. The source is at $(x_s, y_s) = (-2, 0)$ m behind an infinite dielectric slab embedding $N_c = 33$ rods. All the other parameters are kept unchanged. The average transmitted electric field becomes minimum when $g = 0.1057$ m.

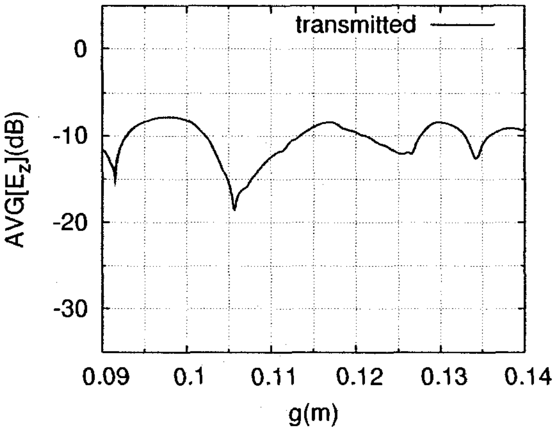

Figure 6.13: Effect of the rod spacing on the average of the transmitted electric field along the line $(x_o, y_o) = (3, -2.5 < y < 2.5)$ m. $N_c = 33$ rods are placed inside an infinite dielectric slab.

Fig. 6.14 shows the transmitted electric field at $(x_o, y_o) = (3, y)$ m when the rod spacing is $g = 0.1057$ m. The finite and infinite slab results are compared. $N_c = 33$ rods are placed inside the infinite and the finite slab of size $2L \times 2d = 5 \times 0.2$ m. It is shown that the results obtained for the finite slab do not match the infinite slab results. This shows that the effect of the end cap contribution is strong if the transmitted field is weaker.

By increasing the slab length to $2L = 10$ m, it was possible to place $N_c = 65$ rods inside the slab where the rods are $g = 0.1524$ m away from each other. Fig. 6.15.a shows the transmitted electric field through the finite and infinite models at $(x_o, y_o) =$

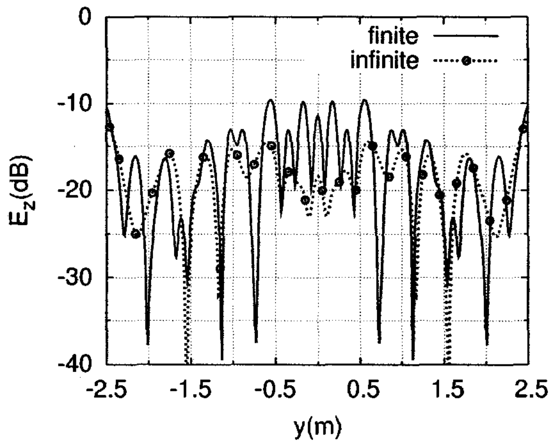

Figure 6.14: Comparing the transmitted electric field through identical finite and infinite reinforced slab. The source is at $(x_s, y_s) = (-2, 0)$ m, and the field point is at $(x_o, y_o) = (3, y)$ m. $N_c = 33$ rods are placed with a spacing of $g = 0.1057$ m inside the finite and infinite slab. The finite slab length is $2L = 5$ m.

$(3, y)$ m. The agreement is very good, showing that the effect of the end caps is weakened when they are far away.

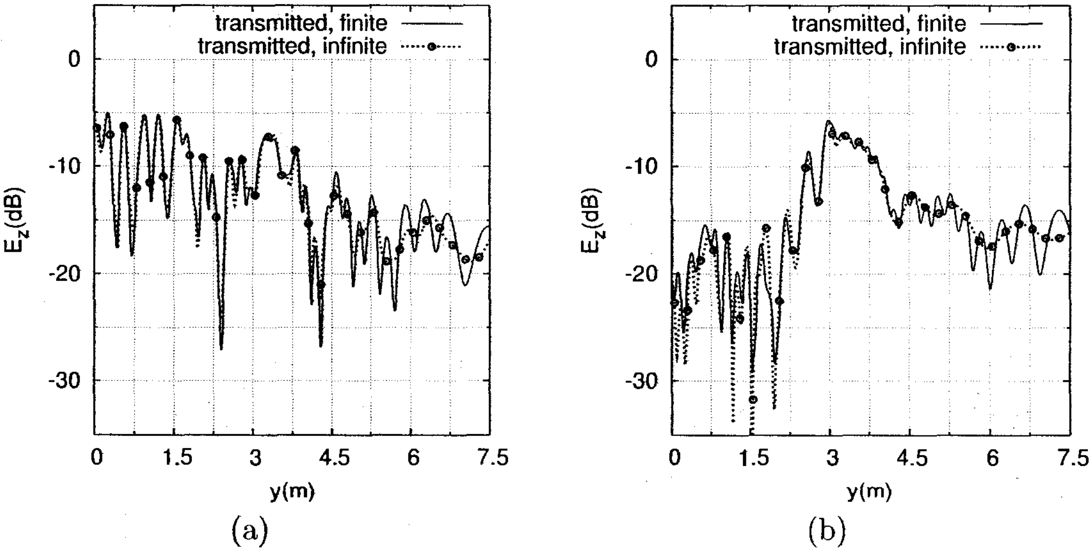

(a)

(b)

Figure 6.15: The transmitted electric field at $(x_o, y_o) = (3, y)$ m. The source is at $(x_s, y_s) = (-2, 0)$ m. $N_c = 65$ rods are placed inside a $2L \times 2d = 10 \times 0.2$ m finite dielectric slab. The rod spacing is (a) $g = 0.1524$ m, (b) $g = 0.1057$ m.

Fig. 6.15.b shows the transmitted field when the rod spacing is reduced to $g = 0.1057$ m. The center of the rods are placed at $x_k = 0.1$ m, $y_k = -3.3824, -3.2767, ..., 3.3824$ m. It is observed that the reinforced slab shows a good shielding behavior when $g = 0.1057$ m.

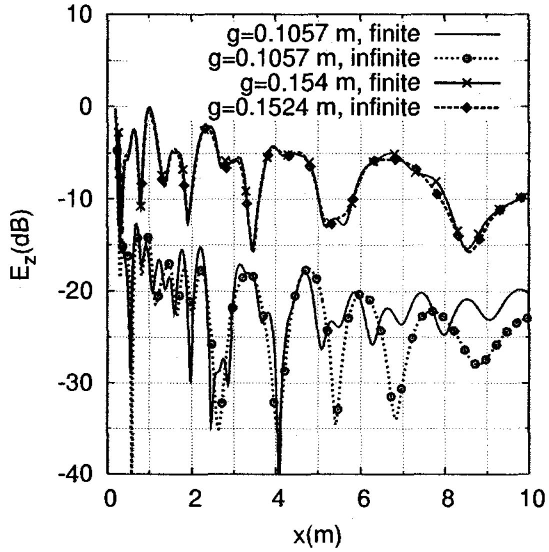

Figure 6.16: The transmitted field for normal incidence. The source is at $(x_s, y_s) = (-2, 0)$ m, and the field point is at $(x_o, y_o) = (x, 0)$ m. $N_c = 65$ rods are placed inside the finite and infinite slab. The finite slab dimension is $2L \times 2d = 10 \times 0.2$ m.

Fig. 6.16 shows the transmitted field through the finite and infinite reinforced slab for normal incidence. The finite and infinite slab results are compared when the rod spacing is $g = 0.1057$ m and $g = 0.1524$ m. The source is at $(x_s, y_s) = (-2, 0)$ m, and the field point is at $(x_o, y_o) = (x, 0)$ m. The result shows the range dependence of the transmitted field. It is seen that when $g = 0.1057$ m, the slab shows a very good shielding property. For this rod spacing, the end cap effect becomes strong when the field point is away from the slab surface ($4.5\ m < x$). When the rod spacing is $g = 0.1524$ m, the end cap contribution to the transmitted field is small.

The analysis of the reinforced concrete was used to study the reflection and transmission of electromagnetic waves for some cases of practical interest. The result showed that the end cap contribution in the transmitted field is negligible when the transmitted field is strong. It was possible to increase the shielding effectiveness of the reinforced concrete by changing the rod spacing. As a result, the transmitted field became weaker by increasing the shielding effectiveness of the reinforced concrete, and the end caps showed a stronger effect on the transmitted field. Another way to weaken the transmitted field, which is not included in the results, is to choose the slab thickness $2d = n\lambda_2/2 + \lambda_2/4$ where $n = 1, 2, 3...$ and λ_2 is the wavelength inside the slab.

Chapter 7

Conclusions

A Green's function/method of moment approach has been developed for modeling a finite reinforced concrete slab. The key step was to obtain an accurate interior Green's function for a thick and finite dielectric slab.

In doing so, an interior Green's function solution was presented for a thick and finite dielectric slab. The solution was based on the separation of variables method which gave an exact solution for a separable dielectric slab. The solution was expressed as a contribution of the surface wave modes plus a residual part which accounted for all other contributions. It was found that the separable slab solution becomes an inaccurate representation of the finite slab when the G_x and G_y surface wave poles are close to each other. This situation can be physically interpreted as a resonance of a surface wave mode.

The separable slab solution was modified by using the method of moments to solve for the surface wave reflection coefficients at the finite slab end caps. The resulting solution represents the physical finite slab that we wish to model, rather than the separable slab. Since the slab was thick, mode conversions occurred when a surface wave mode reached the end caps. The contribution by the surface wave modes was calculated by using the scattering matrix of the end cap and accounting for the multiple reflections of the modes inside the slab. It was found that the residual part of the separable slab solution could be used for the finite slab, without any modifications. The residual part of the separable slab solution was evaluated by the numerical integration of Sommerfeld integral. The result was compared with an HFSS solution and also a surface integral equation/method of moments; the accuracy was found to be satisfactory.

The Green's function for arbitrary source and field point positions, i.e. the cases when the source and/or the field points are inside/outside the finite slab, were obtained by using the interior Green's function. The case when an interior source generates the exterior field was treated by computing the surface equivalent currents from the interior Green's function and then using the surface equivalence principle with the free-space Green's function to compute the exterior field. Applying the reciprocity theorem, we could interchange the source and the field point. As a result, we were able to calculate the Green's function for the case when the interior field was generated by an exterior line source. This was used later for computing the exterior Green's function where we first obtained the electric and magnetic fields on the slab surface generated by an exterior line source. Having the electric and magnetic fields on the slab surface provided the surface equivalent currents. These currents were the sources of the scattered field in the exterior region.

Having the Green's function for the finite dielectric slab, it was possible to model the finite reinforced concrete using Green's function/method of moments. Since the metallic bars inside the slab are electrically thick, each metallic bar could be replaced by a circular array of thin wires subject to the "same surface area" rule of thumb. The unknown induced currents on the surface of the thin wires were computed using the method of moments. The induced currents on the wires gave the scattered field by the wires after using the finite slab Green's function. The Green's function/method of moments results were also compared with the results obtained from a surface integral equation/method of moments code. The Green's function/method of moments approach was computationally more efficient since the number of unknowns were reduced compared to the surface integral equation/method of moments. As a result, this provided a considerable memory saving in the computational modeling when the computational speed was not considered. Although the procedure for computing the exterior Green's function reduced the memory needs, it is not efficient when the computational time is an issue.

The analysis of the reinforced concrete was used to study the reflection and transmission of electromagnetic waves for some cases of practical interest. The result showed that the end cap contribution in the transmitted field is negligible when the transmitted field is strong. It was possible to increase the shielding effectiveness of the reinforced concrete by changing the rod spacing. As a result, the transmitted field became weaker by increasing the shielding effectiveness of the reinforced concrete, and the end caps showed a stronger effect on the transmitted field.

7.1 Future Work

A problem of interest is to extend the two-dimensional model to a three-dimensional geometry with a point source. The challenge is to reduce the memory usage when modeling a three-dimensional structure which is electrically large. Some remarks are given here with respect to how the 2D solution could be extended to the 3D case. A 3D cylindrical structure in front of a point source can be modeled by using a spectrum of 2D problems and applying the inverse Fourier transform technique. The technique of using 2D solutions to construct a 3D solution is well known and is described in Harrington [45] and elsewhere. The technique is readily adaptable to the 2D finite slab if we assume that the boundaries of the the 3D problem are in the x-y plane and the structure cross section does not change along the z axis. Then the Fourier transform with respect to the z-axis can be applied. As a result the structure becomes a 2D problem which is a function of z-directed wave number k_z. For computing the fields for the 3D case, the 2D problem should be solved for an infinite number of k_z's before applying the Fourier transform.

In this approach, it is possible to use a finite number of k_z's. For more details on using the spectrum of 2D solutions for solving 3D cylindrical problems, the reader is referred to a summary of this approach by Kildal *et al.* [46].

The present work models parallel rods inside the dielectric slab. Another area of future research is to consider a cross-grid of wires that truly models an actual rebar structure.

In the approach presented in this thesis, a solution for the separable slab problem was presented. A future study on ray optical interpretations of reflection at the dielectric corners might give a better picture of the field distribution inside the separable slab.

A problem of interest which could be an area for further research is the computational speed improvement for calculating the exterior Green's function presented in this thesis.

Bibliography

[1] E. H. Newman, "An overview of the hybrid MM/Green's function method in electromagnetics," *Proc. IEEE*, vol. 76, no. 3, pp. 270–282, Mar. 1988.

[2] R. Paknys, "Reflection and transmission by reinforced concrete-numerical and asymptotic analysis," *IEEE Trans. Antennas Propagat.*, vol. 51, no. 10, pp. 2852–2861, Oct. 2003.

[3] E. A. Marcatili, "Dielectric rectangular waveguide and directional coupler for integrated optics," *Bell Syst. Tech. J.*, vol. 48, pp. 2071–2102, Sept. 1969.

[4] M. R. Knox and P. P. Toulios, "Integrated circuits for the millimeter through optical frequency range," in *Proc. Symp. Submillimeter Waves*, Brooklyn, NY, 1970, pp. 497–516.

[5] S. A. Bokhari, J. Mosig, and F. Gardiol, "Radiation pattern computation of microstrip antennas on finite size ground planes," *Proc. Inst. Elect. Eng., Pt. H*, vol. 139, no. 3, pp. 278–286, June 1992.

[6] S. Maci, L. Borselli, and L. Rossi, "Diffraction at the edge of a truncated grounded dielectric slab," *IEEE Trans. Antennas Propagat.*, vol. 44, no. 6, pp. 863–873, June 1996.

[7] S. Maci, L. Borselli, and A. Cucurachi, "Diffraction from a truncated grounded dielectric slab: a comparative full-wave/physical-optics analysis," *IEEE Trans. Antennas Propagat.*, vol. 48, no. 1, pp. 48–57, Jan. 2000.

[8] V. Volski and G. Vandenbosch, "Diffraction of a surface wave at the truncation of a dielectric structure," *IEEE Trans. Antennas Propagat.*, vol. 50, no. 12, pp. 1779–1785, Dec. 2002.

[9] E. Jorgensen, S. Maci, and A. Toccafondi, "Fringe integral equation method for a truncated grounded dielectric slab," *IEEE Trans. Antennas Propagat.*, vol. 49, no. 8, pp. 1210–1217, Aug. 2001.

[10] A. A. Shishegar and R. Faraji-Dana, "A closed-form spatial green's function for finite dielectric structure," *Electromagn.*, vol. 23, no. 7, pp. 579–594, Oct. 2003.

[11] H. Derudder, F. Olyslager, D. D. Zutter, and S. V. den Berghe, "Efficient mode-matching analysis of discontinuities in finite planar substrates using perfectly matched layers," *IEEE Trans. Antennas Propagat.*, vol. 49, no. 2, pp. 185–195, Feb. 2001.

[12] J. E. Goell, "A circular-harmonic computer analysis of rectangular dielectric waveguides," *Bell Syst. Tech. J.*, vol. 48, pp. 2133–2160, Sept. 1969.

[13] A. Cullen, O. zkan, and L. Jackson, "Point-matching technique for rectangular-cross-section dielectric rod," *Electron. Lett.*, vol. 7, pp. 497–499, Aug. 1971.

[14] J. H. Richmond, "Scattering by a dielectric cylinder of arbitrary cross section shape," *IEEE Trans. Antennas Propagat.*, vol. 13, no. 3, pp. 334–341, May 1965.

[15] J. H. Richmond, "Scattering by thin dielectric strips," *IEEE Trans. Antennas Propagat.*, vol. 33, no. 1, pp. 64–68, Jan. 1985.

[16] T. K. Wu and L. L. Tsai, "Scattering by arbitrarily cross-sectioned layered lossy dielectric cylinders," *IEEE Trans. Antennas Propagat.*, vol. 25, no. 4, pp. 518–524, July 1977.

[17] Y. Chang and R. F. Harrington, "A surface formulation for characteristic modes of material bodies," Syracuse Univ., Electrical and Computer Engr. Dept. Tech. Rept., Contract No. N00014-67-A-0378-006, 1975.

[18] A. J. Poggio and E. K. Miller, "Integral equation solutions of three-dimensional scattering problems," in *Computer Techniques for Electromagnetics*, R. Mittra, Ed. New York: Pergamon Press, 1973.

[19] T. K. Wu, "Electromagnetic scattering from arbitrarily-shaped lossy dielectric bodies," Ph.D. dissertation, Univ. of Miss., May 1976.

[20] T. K. Wu and L. L. Tsai, "Scattering from arbitrarily-shaped lossy dielectric bodies of revolution," *Radio Science*, vol. 12, pp. 709–718, 1977.

[21] A. Kishk and L. Shafai, "Different formulations for numerical solution of single or multibodies of revolution with mixed boundary conditions," *IEEE Trans. Antennas Propagat.*, vol. 34, no. 5, pp. 666–673, May 1986.

[22] M. A. Rahman and J. B. Davies, "Finite-element analysis of optical and microwave waveguide problems," *IEEE Trans. Microwave Theory Tech.*, vol. 32, no. 1, pp. 20–28, Jan. 1984.

[23] R. Mittra and O. Ramahi, "Absorbing boundary conditions for direct solution of partial differential equations arising in electromagnetic scattering problems," in *Finite Element and Finite Difference Methods in Electromagnetic Scattering*, M. A. Morgan, Ed. New York: Elsevier, 1990.

[24] O. M. Ramahi and R. Mittra, "Finite-element analysis of dielectric scatterers using the absorbing boundary condition," *IEEE Trans. Magn.*, vol. 25, no. 4, pp. 3043–3045, July 1989.

[25] E. Schweig and W. B. Bridges, "Computer analysis of dielectric waveguides: A finite-difference method," *IEEE Trans. Microwave Theory Tech.*, vol. 32, no. 5, pp. 531–541, May 1984.

[26] W. Burnside and K. Burgener, "High frequency scattering by a thin lossless dielectric slab," *IEEE Trans. Antennas Propagat.*, vol. 31, no. 1, pp. 104–110, Jan. 1983.

[27] A. Parsa and R. Paknys, "Interior green's function solution for a thick and finite dielectric slab," *IEEE Trans. Antennas Propagat.*, vol. 55, no. 12, pp. 3504–3514, Dec. 2007.

[28] A. Parsa and R. Paknys, "Approximate green's function for a finite and electrically thick dielectric slab," in *Second European Conf. on Antennas and Propagation (EuCAP 2007)*, Edinburgh, UK, Nov. 11–16, 2007, paper We2.5.7, pp. 1–6.

[29] S. V. Savov and M. H. A. J. Herben, "Modal transmission-line modeling of propagation of plane radiowaves through multilayer periodic building structures," *IEEE Trans. Antennas Propagat.*, vol. 51, no. 9, pp. 2244–2251, Sept. 2003.

[30] E. Richalot, M. Bonilla, M. F. Wong, V. Fouad-Hanna, H. Baudrand, and J. Wiart, "Electromagnetic propagation into reinforced-concrete walls," *IEEE Trans. Microwave Theory Tech.*, vol. 48, no. 3, pp. 357–366, Mar. 2000.

[31] M. Chia, "The effects of reinforced concrete walls/floors on wireless personal communications systems (PCS)," in *IEEE Antennas and Propagation Society*

International Symposium, Newport Beach, CA, USA, June 18–23, 1995, pp. 1956–1959.

[32] R. A. Dalke, C. L. Holloway, P. McKennna, M. Johansson, and A. S. Ali, "Effects of reinforced concrete structures on RF communications," *IEEE Trans. Electromagn. Compat.*, vol. 42, no. 4, pp. 486–496, Nov. 2000.

[33] C. Bin, Y. Yun, G. Cheng, Z. Bihua, and W. Wei, "Analysis of shielding effectiveness of reinforced-concrete in high power electromagnetic environment," in *Asia-Pacific Conference on Environmental Electromagnetics*, Hangzhou, China, Nov. 4–7, 2003, pp. 547–553.

[34] H. M. Elkamchouchi and A. T. Abdelkader, "Shielding effectiveness of reinforced concrete structures in cellular communication bands," in *Radio Science Conference, (NRSC 2002)*, Alexandria, Egypt, Mar. 19–21, 2002, pp. 192–199.

[35] D. Pena, R. Feick, H. D. Hristov, and W. Grote, "Measurement and modeling of propagation losses in brick and concrete walls for the 900-MHz band," *IEEE Trans. Antennas Propagat.*, vol. 51, no. 1, pp. 31–39, Jan. 2003.

[36] Y. P. Zhang and Y. Hwang, "Measurements of the characteristics of indoor penetration loss," in *IEEE Vehicular Technology Conference*, Stockholm, Sweden, June 8–10, 1994, pp. 1741–1744.

[37] H. W. Arnold, R. R. Murray, and D. C. Cox, "815 MHz radio attenuation measured within two commercial buildings," *IEEE Trans. Antennas Propagat.*, vol. 37, no. 10, pp. 1335–1339, Oct. 1989.

[38] Z. Bihua, G. Cheng, C. Bin, and C. Ziming, "Experimental investigation of EMP shielding effectiveness of reinforced-concrete cell model," in *Asia-Pacific Conference on Environmental Electromagnetics*, Shanghai, China, May 3–7, 2000, pp. 296–300.

[39] A. Parsa and R. Paknys, "Reflection and transmission by thick wires in reinforced concrete," in *Proc. Int. Symp. Antenna Technology and Applied Electromagnetics and URSI Conf. (ANTEM 2006/URSI)*, Montreal, Canada, July 17–19, 2006, pp. 251–254.

[40] R. E. Collin, *Field Theory of Guided Waves.* New York: IEEE Press, 1991, pp. 64–80.

[41] L. B. Felsen and N. Marcuvitz, *Radiation and Scattering of Waves.* NJ: Prentice-Hall, 1973, pp. 538–552.

[42] High Frequency Structure Simulator (HFSS), Ansoft Co., Pittsburgh, PA.

[43] T. Itoh, *Numerical Techniques for Microwave and Millimeter-Wave Passive Structures.* New York: Wiley, 1989, pp. 622–636.

[44] A. Ludwig, "Wire grid modeling of surfaces," *IEEE Trans. Antennas Propagat.*, vol. 35, pp. 1045–1048, Sept. 1987.

[45] R. F. Harrington, *Time-Harmonic Electromagnetic Fields.* New York: IEEE Press, 2001, pp. 242–250.

[46] P.-S. Kildal, S. R. Rengarajan, and A. Moldsvor, "Analysis of nearly cylindrical antennas and scattering problems using a spectrum of two-dimensional solutions," *IEEE Trans. Antennas Propagat.*, vol. 44, no. 8, pp. 1183–1192, Aug. 1996.

[47] L. B. Felsen and N. Marcuvitz, *Radiation and Scattering of Waves.* NJ: Prentice-Hall, 1973, pp. 550–552.

[48] K. Liu and C. Balanis, "Simplified formulations for two-dimensional TE-polarization field computations," *IEEE Trans. Antennas Propagat.*, vol. 39, pp. 259–262, Feb. 1991.

[49] A. F. Peterson, S. L. Ray, and R. Mittra, *Computational Methods for Electromagnetics.* New York: IEEE Press, 1998, pp. 39–40.

Appendix A

A.1 Dielectric Slab Bisected by PMC and PEC Ground Planes

In this appendix, we show that the GF solution for a dielectric slab can be obtained by solving the problem of the bisected dielectric slab backed by a PEC and PMC ground plane [47], respectively. We show that the GF can be written as

$$G(x, x_s; y, y_s) = \frac{G^m(x, x_s; y, y_s) + G^e(x, x_s; y, y_s)}{2} \qquad (A.1-1)$$

where G^m and G^e are the GF solution for the bisected dielectric slab backed by PMC and PEC, respectively. We assume a line source of strength I_s located at (x_s, y_s) inside a dielectric slab of thickness d, where the slab is grounded by a PMC or PEC sheets as shown in Fig. A.1.a and Fig. A.2.a, respectively. Applying image theory, the source can be imaged as shown in Fig. A.1.b and Fig. A.2.b. The superposition of the four sources inside the slab of thickness $2d$ shown in Fig. A.1.b and Fig. A.2.b can be expressed by a source at (x_s, y_s) of strength $2I_s$. As a result, the Green's function can be expressed by

$$G(x, x_s; y, y_s) = \frac{G^m(x, x_s; y, y_s) + G^e(x, x_s; y, y_s)}{2} \qquad -\infty \le x, x_s \le d \quad (A.1-2)$$

in Regions 1 and 2a. Similarly, we can reverse the line source direction in Fig. A.2 for the PEC-backed slab and use the superposition to get the transmitted field

$$G(x, 2d - x_s, y, y_s) = \frac{G^m(x, x_s; y, y_s) - G^e(x, x_s; y, y_s)}{2} \qquad -\infty \leq x, x_s \leq d \tag{A.1-3}$$

which is the GF for a line source in Region 2b or 3 at $(2d - x_s, y_s)$ and field point in Region 1 or 2a.

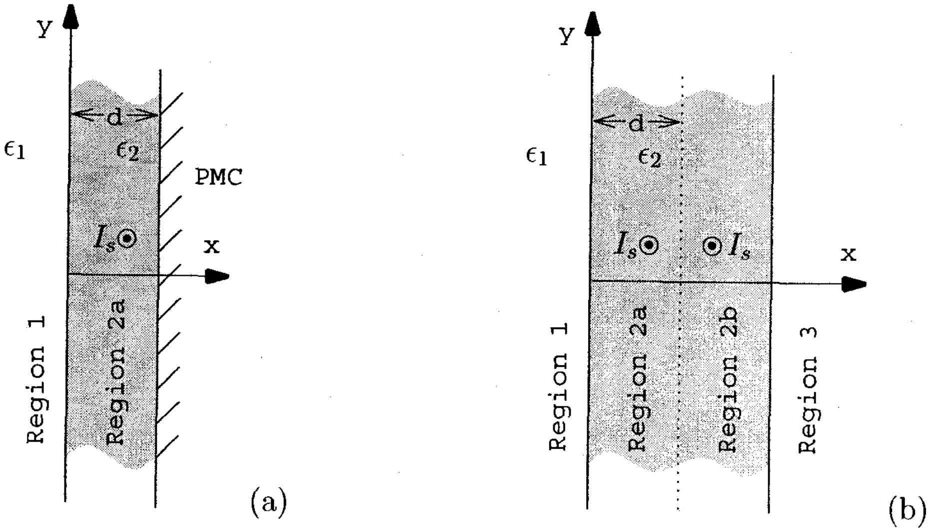

Figure A.1: (a) An electric line source inside a dielectric slab backed by a PMC ground plane. (b) A line source and its image with respect to $x = d$ inside a dielectric slab.

A.2 1D Green's Function for Dielectric Slab Backed by PMC Plane

Fig. A.3 shows the 1D problem for a dielectric slab of thickness d backed by a PMC ground plane. We assume that the source at x_s and the field point at x are both inside the dielectric region. The dielectric region occupies the region between $x = 0$

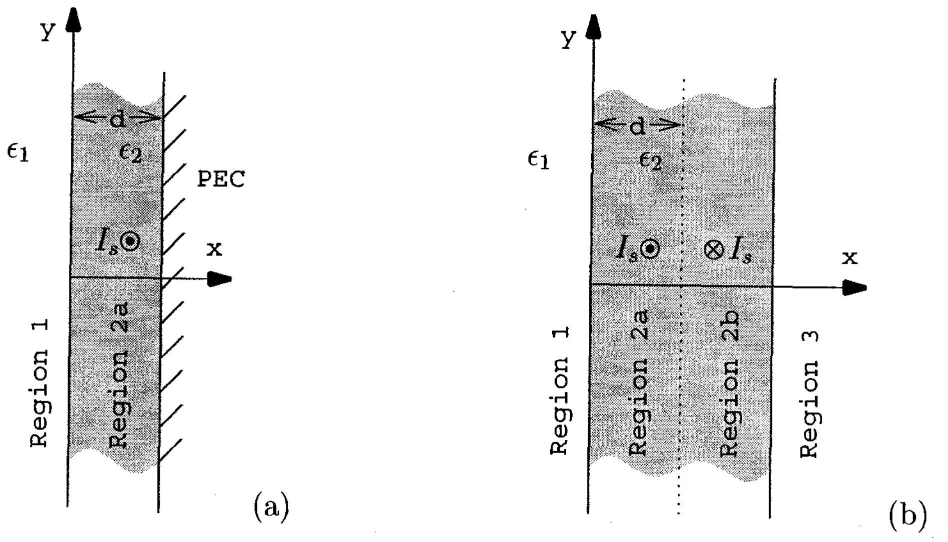

Figure A.2: (a) An electric line source inside a dielectric slab backed by a PEC ground plane. (b) A line source and its image with respect to $x = d$ inside a dielectric slab.

and $x = d$. According to (3.2.6) and (3.2.7), the Green's function should satisfy

$$\frac{d^2G_x}{dx^2} + \kappa_1^2 G_x = -\delta(x - x_s) \qquad x < 0 \tag{A.2-1}$$

$$\frac{d^2G_x}{dx^2} + \kappa_2^2 G_x = -\delta(x - x_s) \qquad 0 \le x \le d. \tag{A.2-2}$$

where κ_1 and κ_2 were defined in (3.2.11) and (3.2.12). The solution should satisfy the

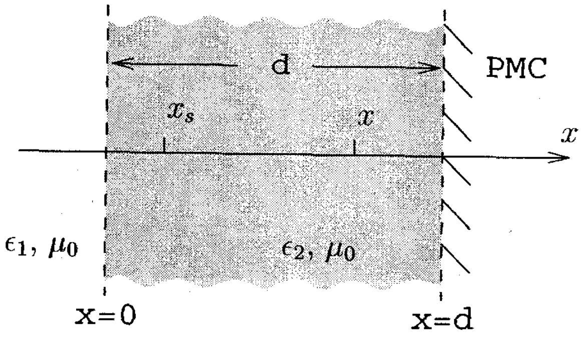

Figure A.3: Dielectric slab backed by PMC.

radiation condition and the boundary conditions at $x = 0$ and $x = d$. The boundary conditions require that $G(x, x_s)$ and $\frac{1}{\mu} dG(x, x_s)/dx$ should be continuous at $x = 0$, and $dG(x, x_s)/dx = 0$ at $x = d$. To construct the Green's function, we follow the UT method [40] which expresses the Green's function as

$$G(x, x_s) = \frac{U(x)T(x_s)}{W(T, U)} \qquad x \leq x_s \tag{A.2-3}$$

$$G(x, x_s) = \frac{U(x_s)T(x)}{W(T, U)} \qquad x_s \leq x \tag{A.2-4}$$

where $T(x)$ and $U(x)$ are independent solutions of the homogeneous wave equation. $W(T, U)$ is the Wronskian of T and U defined as

$$W(T, U) = T(x_s)U'(x_s) - T'(x_s)U(x_s) \tag{$A.2-5$}$$

which is independent of x_s. $T(x)$ satisfies the homogeneous differential equation

$$\frac{d^2T(x)}{dx^2} + \kappa_1^2 T(x) = 0 \qquad x_s < x \leq d \tag{A.2-6}$$

and the boundary condition at $x = d$. It is noted that $U(x)$ satisfies the radiation condition, the boundary condition at $x = 0$ and the homogeneous differential equations

$$\frac{d^2U(x)}{dx^2} + \kappa_1^2 U(x) = 0 \qquad x < 0 \tag{A.2-7}$$

$$\frac{d^2U(x)}{dx^2} + \kappa_2^2 U(x) = 0 \qquad x \leq x_s. \tag{A.2-8}$$

The solutions for the (A.2-6)-(A.2-8) can be written as

$$T(x) = e^{-j\kappa_2(d-x)} + e^{j\kappa_2(d-x)} \qquad x_s \le x \le d \qquad \text{(A.2-9)}$$

$$U(x) = e^{j\kappa_2 x} + Ae^{-j\kappa_2 x} \qquad 0 \le x \le x_s \qquad \text{(A.2-10)}$$

$$U(x) = Be^{j\kappa_1 x} \qquad x < 0 \qquad \text{(A.2-11)}$$

where the boundary condition at $x = d$ and the radiation condition are already imposed. Forcing the boundary condition at the air-dielectric interface, we should have

$$U(x = 0^+) = U(x = 0^-) \qquad (A.2-12)$$

$$\frac{1}{\mu_0}\frac{\partial U(x = 0^+)}{\partial x} = \frac{1}{\mu_0}\frac{\partial U(x = 0^-)}{\partial x} \qquad (A.2-13)$$

which gives the unknowns A and B as

$$A = \frac{\sqrt{\lambda_{x2}} - \sqrt{\lambda_{x1}}}{\sqrt{\lambda_{x2}} + \sqrt{\lambda_{x1}}} \qquad (A.2-14)$$

$$B = \frac{2\sqrt{\lambda_{x2}}}{\sqrt{\lambda_{x2}} + \sqrt{\lambda_{x1}}}. \qquad (A.2-15)$$

The Wronskian of T and U can obtained as

$$W = 2j\kappa_2(e^{j\kappa_2 d} - Ae^{-j\kappa_2 d}). \qquad (A.2-16)$$

Using (A.2-3) and (A.2-4), we have

$$G(x, x_s) = \frac{\left(e^{j\kappa_2 x} + Ae^{-j\kappa_2 x}\right)\left(e^{-j\kappa_2(d-x_s)} + e^{j\kappa_2(d-x_s)}\right)}{2j\kappa_2\left(e^{j\kappa_2 d} - Ae^{-j\kappa_2 d}\right)} \qquad x \le x_s \qquad \text{(A.2-17)}$$

$$G(x, x_s) = \frac{\left(e^{j\kappa_2 x_s} + Ae^{-j\kappa_2 x_s}\right)\left(e^{-j\kappa_2(d-x)} + e^{j\kappa_2(d-x)}\right)}{2j\kappa_2\left(e^{j\kappa_2 d} - Ae^{-j\kappa_2 d}\right)} \qquad x_s \le x \qquad \text{(A.2-18)}$$

where $0 \leq x, x_s \leq d$. The concise expression for the GF becomes

$$G^m_{22x}(x_<, x_>; \kappa_1, \kappa_2) \quad = \quad \frac{\left(e^{j\kappa_2 x_<} + Ae^{-j\kappa_2 x_<}\right)\left(e^{-j\kappa_2(d-x_>)} + e^{j\kappa_2(d-x_>)}\right)}{2j\kappa_2\left(e^{j\kappa_2 d} - Ae^{-j\kappa_2 d}\right)}. \qquad \text{(A.2-19)}$$

It is possible to write (A.2-19) in a trigonometric format as

$$G^m_{22x} = \frac{j\kappa_1 \sin \kappa_2 x_< + \kappa_2 \cos \kappa_2 x_<}{j\kappa_1 \cos \kappa_2 d - \kappa_2 \sin \kappa_2 d} \cdot \frac{\cos \kappa_2(d - x_>)}{\kappa_2} \qquad (A.2-20)$$

where $x_<$ is the smaller of x and x_s, and $x_>$ is the larger of x and x_s.

A.3 1D Green's Function for Dielectric Slab Backed by PEC Plane

The 1D problem for a dielectric slab of thickness d backed by PEC ground plane is shown in Fig. A.4. We assume that the source at x_s and the field point at x are both inside the slab. According to (3.2.6) and (3.2.7), the Green's function should satisfy

$$\frac{d^2G_x}{dx^2} + \kappa_1^2 G_x = -\delta(x - x_s) \qquad x < 0 \qquad \text{(A.3-1)}$$

$$\frac{d^2G_x}{dx^2} + \kappa_2^2 G_x = -\delta(x - x_s) \qquad 0 \leq x \leq d. \qquad \text{(A.3-2)}$$

where κ_1 and κ_2 were defined in (3.2.11) and (3.2.12). The solution should satisfy the boundary conditions at the dielectric boundaries, i.e. $G(x, x_s)$ and $\frac{1}{\mu}dG(x, x_s)/dx$ should be continuous at $x = 0$, and $G(x, x_s) = 0$ at $x = d$. Since the structure is unbounded in the negative x-direction, the Green's function should also satisfy the radiation condition. To construct the Green's function, we follow the UT method [40]. Similar to Appendix A.2, U and T should satisfy (A.2-6)-(A.2-8). The boundary condition for $U(x)$ is similar to the PMC-backed slab. Furthermore, $T(x)$ should

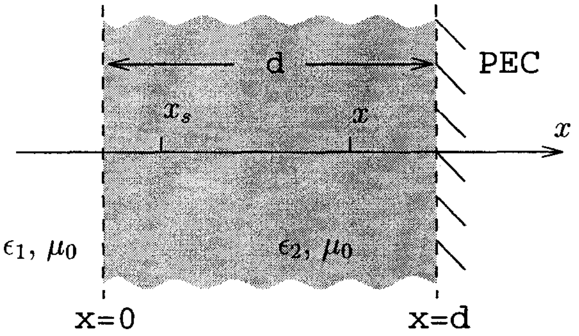

Figure A.4: Dielectric slab backed by PEC.

satisfy the boundary condition at $x = d$, i.e. $T(d) = 0$. The solutions can be written as

$$T(x) = e^{-j\kappa_2(d-x)} - e^{j\kappa_2(d-x)} \qquad x_s \le x \le d \qquad \text{(A.3-3)}$$

$$U(x) = e^{j\kappa_2 x} + Ae^{-j\kappa_2 x} \qquad 0 \le x \le x_s \qquad \text{(A.3-4)}$$

$$U(x) = Be^{j\kappa_1 x} \qquad x < 0. \qquad \text{(A.3-5)}$$

where the boundary condition at $x = d$ and the radiation condition are already imposed. Forcing the boundary condition at the air-dielectric interface gives the unknowns A and B as

$$A = \frac{\sqrt{\lambda_{x2}} - \sqrt{\lambda_{x1}}}{\sqrt{\lambda_{x2}} + \sqrt{\lambda_{x1}}} \qquad (A.3-6)$$

$$B = \frac{2\sqrt{\lambda_{x2}}}{\sqrt{\lambda_{x2}} + \sqrt{\lambda_{x1}}}. \qquad (A.3-7)$$

The Wronskian of T and U becomes

$$W = -2j\kappa_2(e^{j\kappa_2 d} + Ae^{-j\kappa_2 d}). \qquad (A.3-8)$$

Using (A.2-3) and (A.2-4), the Green's function can be written as

$$G(x,x_s) = \frac{\left(e^{j\kappa_2 x} + Ae^{-j\kappa_2 x}\right)\left(e^{j\kappa_2(d-x_s)} - e^{-j\kappa_2(d-x_s)}\right)}{2j\kappa_2\left(e^{j\kappa_2 d} + Ae^{-j\kappa_2 d}\right)} \qquad x \le x_s \tag{A.3-9}$$

$$G(x,x_s) = \frac{\left(e^{j\kappa_2 x_s} + Ae^{-j\kappa_2 x_s}\right)\left(e^{j\kappa_2(d-x)} - e^{-j\kappa_2(d-x)}\right)}{2j\kappa_2\left(e^{j\kappa_2 d} + Ae^{-j\kappa_2 d}\right)} \qquad x_s \le x \tag{A.3-10}$$

where $0 \le x, x_s \le d$. The compact expression for the GF becomes

$$G^e_{22x}(x_<, x_>; \kappa_1, \kappa_2) = \frac{\left(e^{j\kappa_2 x_<} + Ae^{-j\kappa_2 x_<}\right)\left(e^{j\kappa_2(d-x_>)} - e^{-j\kappa_2(d-x_>)}\right)}{2j\kappa_2\left(e^{j\kappa_2 d} + Ae^{-j\kappa_2 d}\right)} \tag{A.3-11}$$

which can be expressed in a trigonometric form as

$$G^e_{22x} = \frac{j\kappa_1 \sin\kappa_2 x_< + \kappa_2 \cos\kappa_2 x_<}{j\kappa_1 \sin\kappa_2 d + \kappa_2 \cos\kappa_2 d} \cdot \frac{\sin\kappa_2(d - x_>)}{\kappa_2}. \tag{$A.3-12$}$$

A.4 Surface Wave Modes of the 2D Infinite Extent Dielectric Slab

The Green's function solution for an infinite extent dielectric slab given by (3.2.20) requires integration in the w plane. The locations of the poles of the integrand should be determined before the integration. The poles of the integrand in (3.2.20) originate from G^m_{22x} and G^e_{22x} which are called PMC and PEC poles, respectively. The transcendental equations for the roots are

$$j\kappa_1 \cos\kappa_2 d - \kappa_2 \sin\kappa_2 d = 0 \qquad \text{(PMC case)} \tag{$A.4-1$}$$

$$j\kappa_1 \sin\kappa_2 d + \kappa_2 \cos\kappa_2 d = 0 \qquad \text{(PEC case).} \tag{$A.4-2$}$$

It is convenient to introduce $p = \kappa_2 d$ and $q = \kappa_1 d$, and rewrite (A.4-1) and (A.4-2) as

$$p \tan p = jq \qquad \text{(PMC case)} \qquad (A.4-3)$$

$$p \cot p = -jq \qquad \text{(PEC case).} \qquad (A.4-4)$$

Since $\kappa_2 = \sqrt{k_2^2 - \eta^2}$ and $\kappa_1 = \sqrt{k_1^2 - \eta^2}$, it can be shown that

$$p^2 - q^2 = \ell^2 = (\epsilon_2/\epsilon_1 - 1)(k_1 d)^2. \qquad (A.4-5)$$

The poles can be obtained by solving (A.4-3), (A.4-4) and (A.4-5). For a lossless case, p and $q_0 = jq$ are real. The numerical computations of the poles can be performed by the secant method. For the lossy case, we can use the secant method with a complex initial guess. For low loss dielectric slabs, the initial guess is chosen very close to the poles that are found for lossless case. Once the poles are found, the residue contribution of the poles can be calculated by using the residue theorem. For a dielectric slab of infinite extent, the residue contribution of (3.2.20) becomes

$$G_{\infty}^{e_\nu, m_\tau} = G_x^{e_\nu, m_\tau}(x, x_s, \mathrm{w}_{\nu,\tau}).D(y - y_s) \qquad (A.4-6)$$

where $G_{\infty}^{e_\nu}$ and $G_{\infty}^{m_\tau}$ are PMC and PEC pole contributions due to w_ν and w_τ which are PEC and PMC poles on the w plane, respectively. Furthermore, $D(y - y_s)$ is

$$D(y - y_s) = e^{-jk_1 \sin \mathrm{w}_{\nu,\tau} |y - y_s|}. \qquad (A.4-7)$$

The expressions for $G_x^{e_\nu}$ and $G_x^{m_\tau}$ can be written as

$$G_x^{e_\nu}(x, x_s, \mathrm{w}_\nu) = \frac{q(jp \cos p_0 - q \sin p_0)}{p k_1 d A_\nu \sin \mathrm{w}_\nu \sin p} \sin(p - p_1) \qquad (A.4-8)$$

$$G_x^{m_\tau}(x, x_s, \mathrm{w}_\tau) = \frac{q(jp\cos p_0 - q\sin p_0)}{pk_1 dA_\nu \sin \mathrm{w}_\nu \cos p} \cos(p - p_1) \qquad (A.4-9)$$

where

$$A_\nu = (j(1 - (q/p)^2) - q(1 - (q/p)^2)) \qquad (A.4-10)$$

and $p_0 = \kappa_2 x_<$ and $p_1 = \kappa_2 x_>$. The propagation constants in the x-direction outside and inside the infinite extent dielectric slab are $\kappa_1 = k_1 \cos \mathrm{w}_{\nu,\tau}$ and $\kappa_2 = \sqrt{k_2^2 - k_1^2 \sin^2 \mathrm{w}_{\nu,\tau}}$, respectively. The total contribution of the SW poles for the dielectric slab problem can be obtained as

$$G_\infty^{SW} = \sum_\nu G^{e_\nu}/2 + \sum_\tau G^{m_\tau}/2. \qquad (A.4-11)$$

A.5 E_z Due to M_x and M_y

When the Green's function G which is the solution of (3.1.4) is available, the electric field E_z generated by a z-directed line source of strength J_z can be obtained by using (3.1.5). Using Maxwell's equation ($\nabla \times \boldsymbol{E} = -j\omega\mu\boldsymbol{H}$), we can obtain H_x and H_y as

$$H_x^s = -\frac{1}{j\omega\mu}\frac{\partial E_z}{\partial y} = J_z\frac{\partial G}{\partial y} \qquad (A.5-1)$$

$$H_y^s = \frac{1}{j\omega\mu}\frac{\partial E_z}{\partial x} = -J_z\frac{\partial G}{\partial x} \qquad (A.5-2)$$

which are the components of the magnetic field $\boldsymbol{H}$. In order to obtain the electric field E_z generated by a magnetic line source, we can use the reciprocity theorem as follows. Fig. A.5.a shows a y-directed magnetic line source M_{y2} at (x_2, y_2) which generates the electric field E_{z2} at (x_1, y_1). Using the reciprocity theorem we can write

$$J_{z1}(x_1, y_1)E_{z2}(x_1, y_1) = -M_{y2}(x_2, y_2)H_{y1}(x_2, y_2) \qquad (A.5-3)$$

where the y-component of the magnetic field H_{y1} at (x_2, y_2) is generated by J_{z1} at

Figure A.5: Reciprocity theorem is applied to obtain the electric field E_{z2} generated by (a) a y-directed magnetic line source M_{y2}, and (b) a x-directed magnetic line source M_{x2}.

(x_1, y_1). Using (A.5-2) and (A.5-3), the electric field E_{z2} due to a y-directed magnetic line source becomes

$$E_{z2}(x_1, y_1) = M_{y2}(x_2, y_2)\frac{\partial G(x_1, x_2; y_1, y_2)}{\partial x_2}. \qquad (A.5-4)$$

To obtain the electric field E_{z2} generated by the x-directed magnetic line source M_{x2} at (x_2, y_2) as shown in Fig. A.5.b, we use the reciprocity theorem as

$$J_{z1}(x_1, y_1)E_{z2}(x_1, y_1) = -M_{x2}(x_2, y_2)H_{x1}(x_2, y_2) \qquad (A.5-5)$$

where the magnetic field component H_{x1} at (x_2, y_2) is generated by an electric line source J_{z1}. Using (A.5-1) in (A.5-5), we can write the electric field E_{z2} due to the x-directed magnetic line source M_{x2} at (x_2, y_2) as

$$E_{z2}(x_1, y_1) = -M_{x2}(x_2, y_2)\frac{\partial G(x_1, x_2; y_1, y_2)}{\partial y_2}. \qquad (A.5-6)$$

If we assume that the magnetic line source is radiating in free space, we can use the free-space Green's function which is

$$G_f = \frac{1}{4j}H_0^{(2)}(k\rho). \qquad (A.5-7)$$

Using (A.5-4), (A.5-6), and the free-space Green's function, the electric field at (x_o, y_o) generated by a magnetic line source at (x_s, y_s) can be written as

$$E_z(x_o, y_o) = \frac{k}{4j}\frac{(x_o - x_s)}{\rho} M_y(x_s, y_s) H_1^{(2)}(k\rho) \qquad (A.5-8)$$

$$E_z(x_o, y_o) = -\frac{k}{4j}\frac{(y_o - y_s)}{\rho} M_x(x_s, y_s) H_1^{(2)}(k\rho) \qquad (A.5-9)$$

where

$$\rho = \sqrt{(x_s - x_o)^2 + (y_s - y_o)^2}. \qquad (A.5-10)$$

A.6 H_x and H_y Due to M_x and M_y

Having the Green's function G, the electric field generated by a line source I_0 can be calculated by using (3.1.5). Moreover, the expressions for the electric field generated by magnetic line sources are given in (A.5-4) and (A.5-6). We can write the magnetic field generated by a magnetic line dipole by using (A.5-1)-(A.5-2), (A.5-4) and (A.5-6) as

$$H_x(x_1, y_1) = -\frac{1}{jw\mu} M_{y2}(x_2, y_2) \frac{\partial G}{\partial x_2 \partial y_1} \qquad (A.6-1)$$

$$H_x(x_1, y_1) = \frac{1}{jw\mu} M_{x2}(x_2, y_2) \frac{\partial G}{\partial y_1 \partial y_2} \qquad (A.6-2)$$

$$H_y(x_1, y_1) = \frac{1}{jw\mu} M_{y2}(x_2, y_2) \frac{\partial G}{\partial x_1 \partial x_2} \qquad (A.6-3)$$

$$H_y(x_1, y_1) = -\frac{1}{jw\mu} M_{x2}(x_2, y_2) \frac{\partial G}{\partial x_1 \partial y_2}. \qquad (A.6-4)$$

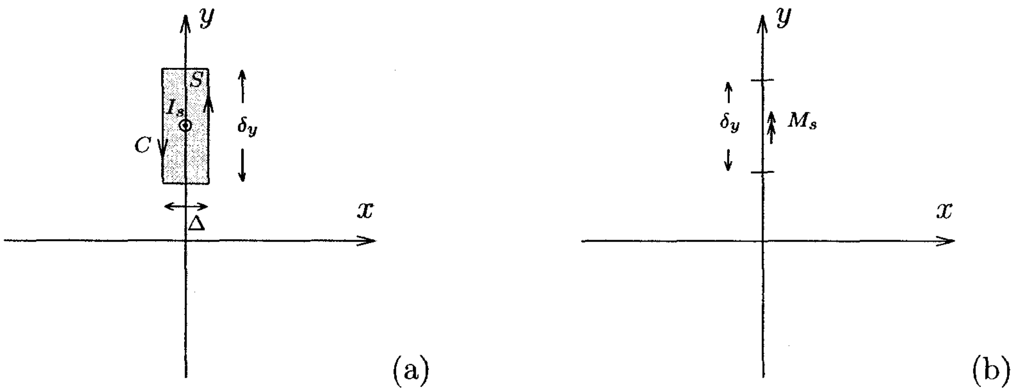

(a) (b)

Figure A.6: (a)Geometry of a rectangular box enclosing a line source at $\boldsymbol{\rho}_n$ with strength I_s. (b) A magnetic line dipole of strength M_s in front of a cell.

A.7 Self Term Evaluation for the First and Second Derivative of Free Space Green's Function

Fig. A.6.a shows a line source in the free space at the center of the n'th cell $\boldsymbol{\rho}_n = x_n\hat{\boldsymbol{x}} + y_n\hat{\boldsymbol{y}}$ where x_n and y_n are given in (5.4.3) and (5.4.4), respectively. The cell extent is assumed to be in the y direction, so $1 \leq n \leq p$. We can use Maxwell's equation on a rectangular box shown in Fig. A.6.a as

$$\oint_C \boldsymbol{H} \cdot \boldsymbol{dl} = I_s + j\omega\epsilon \int\int_S \boldsymbol{E} \cdot \boldsymbol{ds} \qquad (A.7-1)$$

where C and S denote the contour and the area of the rectangle shown in Fig. A.6. The rectangular box has the length of δ_y and width of Δ. The area S becomes small as $\Delta \to 0$. As a result, the last term in (A.7-1) can be neglected. By using (A.5-2), (A.7-1) can be written in the limit ($\Delta \to 0$) as

$$I_s = -\int_{\boldsymbol{\rho}_n^+ - \frac{\delta_y}{2}\hat{\boldsymbol{y}}}^{\boldsymbol{\rho}_n^+ + \frac{\delta_y}{2}\hat{\boldsymbol{y}}} I_s \frac{\partial G_f(\boldsymbol{\rho}_n, \boldsymbol{\rho}^+)}{\partial x^+} dy - \int_{\boldsymbol{\rho}_n^- + \frac{\delta_y}{2}\hat{\boldsymbol{y}}}^{\boldsymbol{\rho}_n^- - \frac{\delta_y}{2}\hat{\boldsymbol{y}}} I_s \frac{\partial G_f(\boldsymbol{\rho}_n, \boldsymbol{\rho}^-)}{\partial x^-} dy \qquad (A.7-2)$$

where $x^{\pm} = x_n \pm \Delta/2$, $\boldsymbol{\rho}^{\pm} = x^{\pm}\hat{\boldsymbol{x}} + y\hat{\boldsymbol{y}}$, and $\boldsymbol{\rho}_n^{\pm} = x^{\pm}\hat{\boldsymbol{x}} + y_n\hat{\boldsymbol{y}}$. since $H_y(\boldsymbol{\rho}^+) = -H_y(\boldsymbol{\rho}^-)$, we can write

$$\frac{\partial G_f(\boldsymbol{\rho}_n, \boldsymbol{\rho}^+)}{\partial x^+} = -\frac{\partial G_f(\boldsymbol{\rho}_n, \boldsymbol{\rho}^-)}{\partial x^-}. \qquad (A.7-3)$$

Using (A.7-3) in (A.7-2) and assuming $I_s = 1$, the self term for the first derivative of the Green's function becomes

$$I_2^{(f)} = \int_{\boldsymbol{\rho}_n^- - \frac{\delta_y}{2}\hat{\boldsymbol{y}}}^{\boldsymbol{\rho}_n^- + \frac{\delta_y}{2}\hat{\boldsymbol{y}}} \frac{\partial G_f(\boldsymbol{\rho}_n, \boldsymbol{\rho}^-)}{\partial x^-}\, dy = \frac{1}{2}. \qquad (A.7-4)$$

It is noted that the current line source is placed on the right side of the n'th cell since a cell occupies the region $\boldsymbol{\rho}_n^- - \frac{\delta_y}{2}\hat{\boldsymbol{y}} \le \boldsymbol{\rho} \le \boldsymbol{\rho}_n^- + \frac{\delta_y}{2}\hat{\boldsymbol{y}}$.

Fig. A.6.b shows a magnetic current line dipole with strength M_s at $\boldsymbol{\rho}_n$. The n'th cell is assumed to be at $\boldsymbol{\rho}^-$ where $1 \le n \le p$. The magnetic field on the n'th cell can be written as

$$H_y(\boldsymbol{\rho}^-) = \frac{1}{j\omega\mu_0}\left(\frac{\partial^2}{\partial y^2} + k_0^2\right)F_y \qquad (A.7-5)$$

where F_y is the y component of the electric vector potential, and $k_0 = w\sqrt{\mu_0\epsilon_0}$. By using the free space Green's function, F_y can be written as

$$F_y = M_s G_f \qquad (A.7-6)$$

where G_f is given in (A.8-3). By using (A.7-6) and (A.8-3), (A.7-5) can be written as [48]

$$H_y(\boldsymbol{\rho}^-) = -M_s\frac{k_2}{8\eta}[H_0^{(2)}(k_2|\boldsymbol{\rho} - \boldsymbol{\rho}') + H_2^{(2)}(k_2|\boldsymbol{\rho} - \boldsymbol{\rho}|)\cos 2\phi] \qquad (A.7-7)$$

where $\cos\phi$ is given in (5.4.12). By using (A.7-7), we can integrate the magnetic field over the n'th cell and write

$$\begin{aligned}\int_{\boldsymbol{\rho}_n^- - \frac{\delta_y}{2}\hat{\boldsymbol{y}}}^{\boldsymbol{\rho}_n^- + \frac{\delta_y}{2}\hat{\boldsymbol{y}}} H_y(\boldsymbol{\rho}^-)\,dy = &- M_s\frac{k_2}{8\eta}\int_{\boldsymbol{\rho}_n^- - \frac{\delta_y}{2}\hat{\boldsymbol{y}}}^{\boldsymbol{\rho}_n^- + \frac{\delta_y}{2}\hat{\boldsymbol{y}}} H_0^{(2)}(k_2|\boldsymbol{\rho} - \boldsymbol{\rho}')\,dy \\ &- M_s\frac{k_2}{8\eta}\int_{\boldsymbol{\rho}_n^- - \frac{\delta_y}{2}\hat{\boldsymbol{y}}}^{\boldsymbol{\rho}_n^- + \frac{\delta_y}{2}\hat{\boldsymbol{y}}} H_2^{(2)}(k_2|\boldsymbol{\rho} - \boldsymbol{\rho}|)\cos 2\phi\,dy\end{aligned} \qquad \text{(A.7-8)}$$

The last integral in (A.7-8) can be derived by using the small argument expansion of the second-order Hankel function. The reader is referred to [48] for more details. The last integral in (A.7-8) becomes

$$\int_{\boldsymbol{\rho}_n^- - \frac{\delta_y}{2}\hat{\boldsymbol{y}}}^{\boldsymbol{\rho}_n^- + \frac{\delta_y}{2}\hat{\boldsymbol{y}}} H_2^{(2)}(k_2|\boldsymbol{\rho} - \boldsymbol{\rho}|)\cos 2\phi\,dy = j\frac{\delta_y}{\pi}(1 - \frac{16}{k_2^2\delta_y^2}). \qquad (A.7-9)$$

By using (A.7-9) and (A.8-4), (A.7-8) can be expressed as

$$\int_{\boldsymbol{\rho}_n^- - \frac{\delta_y}{2}\hat{\boldsymbol{y}}}^{\boldsymbol{\rho}_n^- + \frac{\delta_y}{2}\hat{\boldsymbol{y}}} H_y(\boldsymbol{\rho}^-)\,dy = -M_s\frac{k_2^2\delta_y}{8\omega\mu}[1 - j\frac{2}{\pi}\ln(\frac{k_2\gamma\delta_y}{4e}) + \frac{j}{\pi}(1 - \frac{16}{k_2^2\delta_y^2})] \qquad (A.7-10)$$

where $\gamma = 1.781072$, and $e \approx 2.71828$ is Neper's number. Since the magnetic line source is not on the n'th cell, we can write the source-free wave equation ($\nabla^2 F_y + k_2^2 F_y = 0$) over the cell extent as

$$\frac{\partial^2 F_y}{\partial x^2} = -(\frac{\partial^2}{\partial y^2} + k_2^2)F_y. \qquad (A.7-11)$$

Using (A.7-5)-(A.7-6) and (A.7-10)-(A.7-11), we can write

$$\int_{\boldsymbol{\rho}_n^- - \frac{\delta_y}{2}\hat{\boldsymbol{y}}}^{\boldsymbol{\rho}_n^- + \frac{\delta_y}{2}\hat{\boldsymbol{y}}} \left.\frac{\partial^2 G_f(\boldsymbol{\rho}', \boldsymbol{\rho})}{\partial x^2}\right|_{(\boldsymbol{\rho}_n, \boldsymbol{\rho}^-)} dy = j\frac{k_2^2\delta_y}{8}[1 - j\frac{2}{\pi}\ln(\frac{k_2\gamma\delta_y}{4e}) + \frac{j}{\pi}(1 - \frac{16}{k_2^2\delta_y^2})]. \qquad (A.7-12)$$

Taking the derivative of the free space Green's function with respect to x and x' gives us

$$\frac{\partial G_f(\boldsymbol{\rho}', \boldsymbol{\rho})}{\partial x'} = -\frac{\partial G_f(\boldsymbol{\rho}', \boldsymbol{\rho})}{\partial x}. \qquad (A.7-13)$$

By applying (A.7-13) in (A.7-12), the self term evaluation can be expressed as

$$I_3^{(f)} = \int_{\boldsymbol{\rho}_n^- - \frac{\delta_y}{2}\hat{\boldsymbol{y}}}^{\boldsymbol{\rho}_n^- + \frac{\delta_y}{2}\hat{\boldsymbol{y}}} \left. \frac{\partial^2 G_f(\boldsymbol{\rho}', \boldsymbol{\rho})}{\partial x' \partial x} \right|_{(\boldsymbol{\rho}_n, \boldsymbol{\rho}^-)} dy = -j\frac{k_2^2 \delta_y}{8}\left[1 - j\frac{2}{\pi}\ln(\frac{k_2 \gamma \delta_y}{4e}) + \frac{j}{\pi}(1 - \frac{16}{k_2^2 \delta_y^2})\right]. \qquad (A.7-14)$$

Similar to (A.7-4), it can be shown that for $p + 1 \leq m \leq t$, the self-term evaluation of the first derivative of the free-space Green's function becomes

$$I_2^{(f)} = \int_{\boldsymbol{\rho}_m^- - \frac{\delta_x}{2}\hat{\boldsymbol{x}}}^{\boldsymbol{\rho}_m^- + \frac{\delta_x}{2}\hat{\boldsymbol{x}}} \frac{\partial G_f(\boldsymbol{\rho}_m, \boldsymbol{\rho}^-)}{\partial y^-} dx = \frac{1}{2} \qquad (A.7-15)$$

where $y^- = y_m - \Delta/2$, $\boldsymbol{\rho}^- = x\hat{\boldsymbol{x}} + y^-\hat{\boldsymbol{y}}$, and $\boldsymbol{\rho}_m^- = x_m\hat{\boldsymbol{x}} + y^-\hat{\boldsymbol{y}}$. Furthermore, (A.7-12) can be written for $p + 1 \leq m \leq t$ as

$$\int_{\boldsymbol{\rho}_m^- - \frac{\delta_x}{2}\hat{\boldsymbol{x}}}^{\boldsymbol{\rho}_m^- + \frac{\delta_x}{2}\hat{\boldsymbol{x}}} \left. \frac{\partial^2 G_f(\boldsymbol{\rho}', \boldsymbol{\rho})}{\partial y' \partial y} \right|_{(\boldsymbol{\rho}_m, \boldsymbol{\rho}^-)} dx = -j\frac{k_2^2 \delta_x}{8}\left[1 - j\frac{2}{\pi}\ln(\frac{k_2 \gamma \delta_x}{4e}) + \frac{j}{\pi}(1 - \frac{16}{k_2^2 \delta_x^2})\right]. \qquad (A.7-16)$$

A.8 Self Impedance Term Evaluation for the Interior Green's Function

The self impedance term evaluation for the interior Green's function is required when computing the exterior Green's function. Furthermore, the first and second derivative of the interior Green's function should be evaluated. The self impedance term evaluation of the interior Green's function is required to calculate K_{nn}^K in (5.4.43).

First, we need to evaluate an integral in form of

$$I_1 = \int_{\boldsymbol{\rho}_n - \frac{\delta_t}{2}\hat{\boldsymbol{t}}}^{\boldsymbol{\rho}_n + \frac{\delta_t}{2}\hat{\boldsymbol{t}}} G_{22}(\boldsymbol{\rho}_n, \boldsymbol{\rho})\, dt \qquad (A.8-1)$$

where $G_{22}(\boldsymbol{\rho}_n, \boldsymbol{\rho})$, the interior Green's function, is singular at $\boldsymbol{\rho}_n = \boldsymbol{\rho}$. The parametric variable t depends on the cell orientation, and $\hat{\boldsymbol{t}} = \{\hat{\boldsymbol{x}}, \hat{\boldsymbol{y}}\}$. As a result, we have $dt = \{dx, dy\}$, and $\delta_t = \{\delta_x, \delta_y\}$. To evaluate I_1, a singularity subtraction is expedient. This can be realized by writing the interior Green's function as

$$G_{22} = G_f + G_m \qquad (A.8-2)$$

where G_f, which is the free space Green's function, contains the singularity of the interior Green's function. The free space Green's function expressed by the Hankel function is

$$G_f = \frac{1}{4j} H_0^{(2)}(k_2 |\boldsymbol{\rho}_n - \boldsymbol{\rho}|)) \qquad (A.8-3)$$

where k_2 is the wave number in the dielectric region. Using the small argument formulation for the Hankel function [49], the self term for G_f can be written as

$$I_1^{(f)} = \int_{\boldsymbol{\rho}_n - \frac{\delta_t}{2}\hat{\boldsymbol{t}}}^{\boldsymbol{\rho}_n + \frac{\delta_t}{2}\hat{\boldsymbol{t}}} G_f(\boldsymbol{\rho}_n, \boldsymbol{\rho})\, dt = \frac{\delta_t}{4j}[1 - j\frac{2}{\pi}\ln(\frac{\gamma k_2 \delta_t}{4e})] \qquad (A.8-4)$$

where $\gamma = 1.781072$ is Euler's constant. By subtracting G_f from the interior Green's function, G_m can be written as

$$G_m = G_m^{(1)} + G_m^{(2)} + G_{finite}^{SW} - G_\infty^{SW} \qquad (A.8-5)$$

where G^{SW}_{finite} and G^{SW}_{∞} are given in (4.4.9) and (A.4-11), respectively. Using (4.4.10), (A.8-2) and (A.8-5), $G^{(1)}_m$ and $G^{(2)}_m$ can be written as

$$G^{(1)}_m = \frac{j}{\pi}\int_{\overline{P}} \kappa_1\eta_2 G_x G^{(y)}_m \, \mathrm{dw} \qquad (A.8-6)$$

$$G^{(2)}_m = \frac{j}{\pi}\int_{\overline{S}} \kappa_1\eta_2 G^{(x)}_m G^{(y)}_f \, \mathrm{dw} \qquad \text{(A.8-7)}$$

where G_x is given in (3.3.17). Furthermore, $G^{(y)}_f$, $G^{(x)}_m$ and $G^{(y)}_m$ are

$$G^{(y)}_f = \frac{e^{-j\eta_2(y_> - y_<)}}{2j\eta_2} \qquad (A.8-8)$$

$$G^{(x)}_m = \frac{\Gamma_x e^{-j\kappa_2(4d - x_> - x_<)} + \Gamma_x e^{-j\kappa_2(x_> + x_<)} + \Gamma_x^2 e^{-j\kappa_2(4d + x_> - x_<)} + \Gamma_x^2 e^{-j\kappa_2(4d - x_> + x_<)}}{2j\kappa_2(1 - \Gamma_x^2 e^{-j4\kappa_2 d})} \qquad (A.8-9)$$

$$G^{(y)}_m = \frac{\Gamma e^{-j\eta_2(2L - y_> - y_<)} + \Gamma e^{-j\eta_2(2L + y_> + y_<)} + \Gamma^2 e^{-j\eta_2(4L + y_> - y_<)} + \Gamma^2 e^{-j\eta_2(4L - y_> + y_<)}}{2j\eta_2(1 - \Gamma^2 e^{-j4\eta_2 L})} \qquad (A.8-10)$$

where Γ is given in (3.3.31), and Γ_x can be expressed as

$$\Gamma_x = \frac{\kappa_2 - \kappa_1}{\kappa_2 + \kappa_1}. \qquad (A.8-11)$$

The path of integration $\overline{P}$ is shown in Fig. 3.13. It is noted that $G^{(x)}_m$ has a branch point at $\kappa_2 = 0$. As a result, we choose the path $\overline{S}$ to evaluate (A.8-7). Fig. A.7 shows the path of integration and the branch cuts on the w-plane. The path is chosen so that it does not cross any branch cut. It is noted that $G_f + G^{(2)}_m$ gives the infinite slab Green's function, and it already includes the surface wave contribution of the infinite slab denoted by G^{SW}_{∞}. Since the surface wave contribution of the infinite slab is also included in G^{SW}_{finite}, the term $-G^{SW}_{\infty}$ appears in (A.8-5).

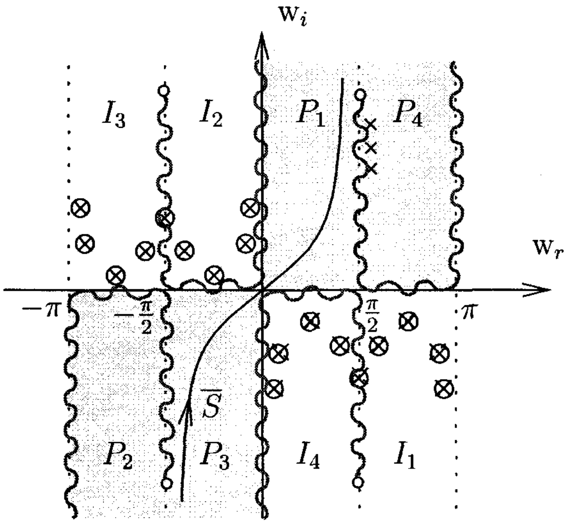

Figure A.7: Complex w-plane shows the path of integration $\overline{S}$. The LW poles ($\otimes$) and SW poles ($\times$) are shown on this plane

In summary, I_1 given in (A.8-1) can be written as

$$I_1 = I_1^{(f)} + \int_{\boldsymbol{\rho}_n - \frac{\delta_t}{2}\hat{\boldsymbol{t}}}^{\boldsymbol{\rho}_n + \frac{\delta_t}{2}\hat{\boldsymbol{t}}} G_m(\boldsymbol{\rho}_n, \boldsymbol{\rho})\, dt \qquad (A.8-12)$$

where $I_1^{(f)}$ and G_m are given in (A.8-4) and (A.8-5), respectively.

To compute the exterior Green's function, we should also evaluate the first derivative of I_1. If we assume a y-directed cell ($1 \leq n \leq p$) in (A.8-1), the derivative of I_1 with respect to x can be written by using (A.8-2) as

$$I_2 = I_2^{(f)} + \int_{\boldsymbol{\rho}_n - \delta_y/2}^{\boldsymbol{\rho}_n + \delta_y/2} \frac{\partial G_m(\boldsymbol{\rho}_n, \boldsymbol{\rho})}{\partial x}\, dy. \qquad (A.8-13)$$

where $I_2^{(f)}$ is the self-term calculated for the derivative of the free space Green's function which is given in (A.7-4). Furthermore, for the cells in the range $p + 1 \leq$

$n \leq t$, I_2 becomes

$$I_2 = I_2^{(f)} + \int_{\boldsymbol{\rho}_n - \delta_s/2}^{\boldsymbol{\rho}_n + \delta_s/2} \frac{\partial G_m(\boldsymbol{\rho}_n, \boldsymbol{\rho})}{\partial y} \, dx \qquad (A.8-14)$$

where $I_2^{(f)}$ is given in (A.7-15). Similarly, the self-term for the second derivative of the interior Green's function for $1 \leq n \leq p$ is in form of

$$I_3 = I_3^{(f)} + \int_{\boldsymbol{\rho}_n - \delta_y/2}^{\boldsymbol{\rho}_n + \delta_y/2} \left. \frac{\partial^2 G_m(\boldsymbol{\rho}', \boldsymbol{\rho})}{\partial x' \partial x} \right|_{(\boldsymbol{\rho}_n, \boldsymbol{\rho})} dy \qquad (A.8-15)$$

where $I_3^{(f)}$ is given in (A.7-14). When $p + 1 \leq n \leq t$, I_3 becomes

$$I_3 = I_3^{(f)} + \int_{\boldsymbol{\rho}_n - \delta_x/2}^{\boldsymbol{\rho}_n + \delta_x/2} \left. \frac{\partial^2 G_m(\boldsymbol{\rho}', \boldsymbol{\rho})}{\partial y' \partial y} \right|_{(\boldsymbol{\rho}_n, \boldsymbol{\rho})} dx \qquad (A.8-16)$$

where $I_3^{(f)}$ is given in (A.7-16).